

# Investigation of granular flow using silo centrifuge models

PARDEM



John Mathews

Institut für Geotechnik

University of Natural Resources and Life Sciences, Vienna

A thesis submitted for the degree of

*Doctor of Philosophy*

Thesis number: 28

September 2013





# Investigation of granular flow using silo centrifuge models

---

John Mathews



This thesis is dedicated to my children. God willing, I will give you an excellent foundation to build on.



## Acknowledgements

I would like to thank all those whose support I have received during this research:

- God Almighty, my inspiration and sustainer.
- My supervisor Prof. Wei Wu, whose incisive observations and suggestions have helped direct and accelerate this work.
- My wife Ritsya-el for her total support, patience and encouragement.
- My loving parents who have always supported and stood by me.
- My colleagues in the PARDEM network who have contributed to a rich and varied three years which I will remain very grateful for. Collaborating with Pratap Kasina and Mar Combarros has been particularly productive, encouraging and enjoyable.
- My colleagues at the Institute for Geotechnical Engineering at BOKU in Vienna. Particularly Miguel Angel Cabrera, Gregor Idinger, Enrico Soranzo and Barbara Świtała, who have all made my time at BOKU more productive and enjoyable.
- Boris Štimac and Olja Barbir, my two masters students who are hard-working, quick learners and good colleagues.
- Jason Barrington, MEng., for his assistance developing Excel macro files.
- Dr. Markus Raucher, for his practical support improving the silo centrifuge model.
- Itasca GmbH, for their generous lease of PFC licences.
- Dr. Lothar te Kamp of Itasca GmbH, for his advice and encouragement concerning PFC3d.

This research was undertaken as part of the PARDEM Initial Training Network. It was funded by Marie Curie Actions and the European Union's Research Framework 7 programme. The financial support for this project is gratefully acknowledged.



## Abstract

Silo discharge and silo wall pressures have been investigated for over a century, but many features of silo design and operation are only partially understood. The velocity field within the silo during discharge cannot be reliably predicted yet, and the mechanisms controlling discharge remain unclear. This thesis presents an investigation into gravity discharge from silos in increased gravity conditions. Flow conditions and lateral wall pressures are quantified. A review of silo centrifuge modelling and silo discharge under the action of gravity is also presented.

It is shown that the mass flow rate is proportional to the square root of the gravity and that the width of the flow channel at any given height above the outlet is independent of gravity. The local velocity of discharging material is also proportional to the square root of the gravity. These observations show that the angle at which a stagnant zone intercepts a silo wall is independent of gravity and that the criteria for funnel or mass flow conditions are independent of gravity.

Analysis of the time required to discharge the silo leads to the observation of a scaling law for silo centrifuge models, which is useful for centrifuge models involving granular flows. In a silo model discharging cohesionless material, time scales with gravity according to the following law:

$$t_m = t_p N^{-1/2}$$

Force Sensing Resistors (FSRs) are used to measure normal pressure across the silo walls. The performance of the FSR arrays is assessed by investigating normal pressures before and during discharge. The FSR instrumentation does not distinguish between normal and shear forces

and this influences the readings, however qualitative and in some cases quantitative agreement with Janssen's wall pressure theory based on continuum assumptions was found.

A discrete element model is presented with the aim of investigating micro-scale mechanisms. The DEM model was calibrated by conducting a series of triaxial tests where the micro properties were varied until a bulk response similar to the physical material was obtained. These material properties were then used to model a silo of the same dimensions as the physical model discharging under different gravity conditions. The discharge rate for the numerical model was found to fluctuate greatly and the response to gravity of the discharge rate is not the same as is observed elsewhere.

## **Abstract**

Das Auslassen eines Silos sowie der Druckverlauf an dessen Wänden werden seit über einem Jahrhundert untersucht, jedoch sind viele Eigenschaften betreffend Design und Betrieb eines Silos nur zum Teil bekannt. Das Geschwindigkeitsprofil im Silo während des Auslassens kann nicht zuverlässig vorhergesagt werden, und der Mechanismus welcher das Auslaufen kontrolliert ist unklar. Diese Dissertation präsentiert eine Untersuchung über den gravitationsabhängigen Ausfluss von Silos in erhöhten Gravitationsfeldern. Fließkonditionen und laterale Wanddrücke werden quantifiziert. Ein Überblick über die Modellierung von Silos mittels Zentrifugenversuchen sowie das Auslaufen in Abhängigkeit der Gravitation wird ebenfalls präsentiert.

Es wird aufgezeigt, dass der Massendurchfluss proportional zum Quadrat der Gravitation ist, und die Breite des fließenden Bereichs für jede beliebige Höhe über dem Ausfluss unabhängig der Gravitation ist. Die lokale Geschwindigkeit des ausfließenden Materials ist ebenfalls proportional zum Quadrat der Gravitation. Beobachtungen zeigen, dass der Winkel unter welchem eine stagnierende Zone auf die Wand des Silos trifft unabhängig der Gravitation ist. Kriterien welche über Kamin- oder Massenausfluss entscheiden sind ebenfalls unabhängig der Gravitation.

Eine Untersuchung über die benötigte Zeit um einen Silo zu entleeren führt zur Definierung eines Skalierungsgesetzes für Silomodellversuche in einer Zentrifuge, welche zur Beschreibung granularem Fließens in Zentrifugenmodellversuchen nützlich ist. Die Auslaufzeit eines Silos mit kohäsionslosem Material in Relation zur Gravitation kann mit folgender

Beziehung beschrieben werden:

$$t_m = t_p N^{-1/2}$$

Kraftmesswiderstände (FSRs) werden eingesetzt um den Normaldruck an den Siloinnenwänden zu messen. Das Ergebnis der FSR Felder wird durch die Untersuchung des Normaldrucks vor und während des Auslassens bewertet. Die Messung mittels FSR unterscheidet nicht zwischen Normal- und Scherkräften, was die Messwerte beeinflusst. Trotzdem wurden qualitative, sowie in manchen Fällen auch quantitative, Übereinstimmungen mit Janssen's theoretischer Druckverteilung gefunden.

Ein Discrete Element Model wird vorgestellt, mit dem Ziel mikroskalare Mechanismen zu erforschen. Das DEM Model wurde mittels einer Serie Triaxial-Versuche kalibriert, wobei Mikroeigenschaften soweit variiert wurden bis das Gesamtverhalten dem des physikalischen Materials ähnelte. Diese Materialeigenschaften wurden weiter verwendet um ein numerisches Silomodell mit den gleichen Dimensionen des experimentellen Modellsilos bei unterschiedlicher Gravitation zu modellieren. Es hat sich gezeigt, dass die Abflussrate des numerischen Modells stark fluktuiert. Weiters weicht die Abflussrate in Abhängigkeit der Gravitation von anderen Beobachtungen ab.

---

# Contents

<b>Contents</b>	<b>xiii</b>
<b>List of Figures</b>	<b>xvii</b>
<b>Nomenclature</b>	<b>xxvi</b>
<b>1 Introduction</b>	<b>1</b>
1.1 Motivation . . . . .	1
1.2 Scope and structure . . . . .	2
<b>2 State-of-the-art review</b>	<b>5</b>
2.1 Silo and hopper design principles . . . . .	5
2.1.1 Background . . . . .	6
2.1.2 Flow pattern . . . . .	7
2.1.3 Silo dimensions . . . . .	11
2.1.4 Flow rate . . . . .	12
2.1.5 Inlets and outlets . . . . .	14
2.1.6 Measurement and variability of material properties . . . . .	14
2.1.7 Calculating structural loads . . . . .	14
2.1.8 Design codes . . . . .	24
2.2 Granular discharge through an orifice . . . . .	26
2.2.1 Derivation of the Beverloo discharge correlation . . . . .	28
2.2.2 The collapsing arch analogy . . . . .	29
2.2.3 The empty annulus . . . . .	30
2.2.4 Bulk density measurements for discharge prediction . . . . .	32
2.2.5 Discharge rate from hoppers . . . . .	33

## CONTENTS

---

2.2.6	Discharge through non-circular orifices . . . . .	34
2.2.7	Effect of gravity on static and dynamic angles of repose . . . . .	35
2.3	Principles of centrifuge modelling . . . . .	35
2.4	Silo centrifuge modelling . . . . .	38
2.4.1	Background . . . . .	38
2.4.2	Silo centrifuge model design . . . . .	41
2.5	Silo research . . . . .	42
2.6	Discharge pressure theories for structural design . . . . .	43
2.6.1	Influence of particle shape . . . . .	43
2.6.2	Design considerations . . . . .	44
2.7	Numerical modelling using the Discrete Element Method (DEM) . . . . .	45
2.7.1	Introduction . . . . .	45
2.7.2	DEM calculation cycle . . . . .	47
2.7.3	Force-displacement law . . . . .	48
2.7.4	Law of motion . . . . .	49
2.7.5	Boundary conditions and initial conditions . . . . .	49
2.7.6	Determination of time-step . . . . .	49
2.8	Research summary tables . . . . .	50
<b>3</b>	<b>Loads on silos and hoppers according to BS EN 1991-4:2006</b>	<b>55</b>
3.1	General Rules . . . . .	56
3.1.1	Evaluation of the lateral pressure ratio K . . . . .	57
3.2	Wall pressures for flat-bottomed silo . . . . .	58
3.2.1	Horizontal and vertical pressures and wall frictional traction . . . . .	58
3.2.2	Pressures during discharge on vertical walls . . . . .	59
3.3	Silo with 30 degree hopper . . . . .	60
3.3.1	Filling loads . . . . .	61
3.3.2	Discharge loads . . . . .	62
3.4	Silo with 60 degree hopper . . . . .	64
3.4.1	Hopper wall friction coefficient in a shallow hopper . . . . .	64
3.4.2	Filling loads . . . . .	64
3.4.3	Discharge loads . . . . .	66

---

<b>4 Silo centrifuge model description</b>	<b>67</b>
4.1 Introduction	67
4.2 Stress equivalence between scales	67
4.3 Development of a scaling law for time in silo centrifuge models	68
4.4 Experimental set-up	69
4.4.1 Description of the IGT Beam centrifuge	69
4.4.2 Design of the model	72
4.5 Instrumentation	79
4.5.1 High-speed video	79
4.5.2 Particle Image Velocimetry	82
4.5.3 Load cells	87
4.6 Granular materials	89
4.7 Test procedure	95
<b>5 Experimental results</b>	<b>99</b>
5.1 Introduction	99
5.2 Method and instrumentation	99
5.3 Results presentation	100
5.4 Repeatability	101
5.5 Verification of centrifugal acceleration	101
5.6 Flow acceleration	105
5.7 Discharge rates	106
5.8 Scaled discharge rates	111
5.9 Normalised flow profiles	116
5.10 Flow profiles at different heights	129
5.11 Flow profile comparison with different silo geometry	132
5.12 Settlement	134
5.13 Normal wall pressures before and during discharge	140
5.13.1 Introduction	140
5.13.2 Sensor specification and calibration	142
5.13.3 Silo centrifuge tests with pressure sensors	145

## CONTENTS

---

5.13.4 Conclusions . . . . .	154
<b>6 Discrete element model of silo discharge</b>	<b>157</b>
6.1 Model design . . . . .	157
6.1.1 Dimensions . . . . .	158
6.1.2 Parameters . . . . .	158
6.1.3 Filling . . . . .	160
6.1.4 Discharge . . . . .	160
6.2 Calibration process for numerical model . . . . .	161
6.3 Density increases at higher gravities . . . . .	164
6.4 Mass flow rate . . . . .	166
6.5 Flow patterns during discharge . . . . .	171
<b>7 General conclusions and suggestions for further work</b>	<b>177</b>
<b>Appendix A: Silo centrifuge model drawings</b>	<b>185</b>
<b>Appendix B: Instrumentation details - Load Cells</b>	<b>193</b>
<b>Appendix C: Recommendations for silo centrifuge model design and development</b>	<b>197</b>
<b>References</b>	<b>201</b>

# List of Figures

2.1	Forms of flow pattern: a) Mass flow b) Parallel pipe flow c) Taper mixed flow d) Concentric mixed flow e) Fully eccentric mixed flow f) Eccentric parallel pipe flow g) Eccentric taper pipe flow . . . . .	9
2.2	Example of Jenike design chart for silos with conical hopper . . . . .	10
2.3	Example of Jenike design chart for silos with planar hopper . . . . .	11
2.4	Janssen pressure slice . . . . .	16
2.5	Janssen pressure pattern . . . . .	17
4.1	Schematic sketch of Trio-Tech 1231 Geotechnical Centrifuge, Ferstl [1998] . . . . .	70
4.2	General view of geotechnical centrifuge . . . . .	72
4.3	Sketch of model silo in centrifuge during flight. 1-direction of horizontal rotation, 2-centrifuge beam, 3-swing basket during flight . . . . .	74
4.4	3D sketch representing silo model before filling, before centrifuge flight, and during flight . . . . .	75
4.5	Sketch of model silo outside of centrifuge, 1-acrylic window, 2-side wall, 3-filling funnel, 4-camera, 5,6-LED array, 7-camera stand, 8-data logger, 9-vertical roller, 10-collection bucket . . . . .	76
4.6	Funnel used to fill silo . . . . .	77
4.7	Top view of empty model silo showing pressure pads, data logger and high-speed camera . . . . .	77
4.8	Side view of opening mechanism . . . . .	78
4.9	Photograph of model silo showing stopwatch and grid points . . . . .	80
4.10	High-speed video example of silo discharge, 11.5x slower (20 FPS, original = 232 FPS), click to play . . . . .	81

## LIST OF FIGURES

---

4.11 Example of PIV analysis of discharge from silo with flat-bottom, 19x slower (12 FPS, original = 232 FPS) click to play [ <i>m/s</i> ] . . . . .	84
4.12 Description of PIV vector calculation . . . . .	85
4.13 Image preparation . . . . .	86
4.14 Difference between applied and output loads using 2 1kN C9B HBM Load Cells. Average error is 0.441% . . . . .	89
4.15 Photograph of material M1, fine sand . . . . .	92
4.16 Photograph of material M2, coarse sand . . . . .	92
4.17 Photograph of material M3, glass beads mixture . . . . .	92
4.18 Photograph of material M4, Polyamide mixture . . . . .	93
4.19 Grain size distribution of material M1: fine quartz sand DIN EN 12904 . . . . .	93
4.20 Particle size distribution of material M2: DIN 1164/58 Norm Sand II . . . . .	94
4.21 Results from triaxial tests on the coarse sand (M2) showing dependency of angle of internal friction on density and confining pressure (Klein, 1998) . . . . .	94
4.22 Typical test . . . . .	96
4.23 Typical load cell result, Coarse sand, Flat bottomed silo, 10g . . . . .	97
5.1 Data from load cells . . . . .	103
5.2 Discharge times in silo with flat bottom . . . . .	103
5.3 Discharge times in silo with 30 degree hopper . . . . .	104
5.4 Velocity magnitude of material above outlet at different stages of discharge in silo with flat bottom . . . . .	105
5.5 Velocity magnitude of material above outlet at different stages of discharge in silo with 30 degree hopper . . . . .	106
5.6 Discharge rates, Material M1 - Fine sand, Silo with flat bottom . . . . .	107
5.7 Discharge rates, Material M1 - Fine sand, Silo with 30 degree hopper . . . . .	107
5.8 Discharge rates, Material M2 - Coarse sand, Silo with flat bottom . . . . .	108
5.9 Discharge rates, Material M2 - Coarse sand, Silo with 30 degree hopper . . . . .	108
5.10 Discharge rates, Material M3 - Glass beads, Silo with flat bottom . . . . .	109
5.11 Discharge rates, Material M3 - Glass beads, Silo with 30 degree hopper . . . . .	109
5.12 Discharge rates, Material M4 - Polyamide, Silo with flat bottom . . . . .	110
5.13 Discharge rates, Material M4 - Polyamide, Silo with 30 degree hopper . . . . .	110

5.14	Normalised discharge rates, Material M1 - Fine sand, Silo with flat bottom	112
5.15	Normalised discharge rates, Material M1 - Fine sand, Silo with 30 degree hopper . . . . .	112
5.16	Normalised discharge rates, Material M2 - Coarse sand, Silo with flat bottom . . . . .	113
5.17	Normalised discharge rates, Material M2 - Coarse sand, Silo with 30 degree hopper . . . . .	113
5.18	Normalised discharge rates, Material M3 - Glass beads, Silo with flat bottom . . . . .	114
5.19	Normalised discharge rates, Material M3 - Glass beads, Silo with 30 degree hopper . . . . .	114
5.20	Normalised discharge rates, Material M3 - Polyamide, Silo with flat bottom . . . . .	115
5.21	Normalised discharge rates, Material M3 - Polyamide, Silo with 30 degree hopper . . . . .	115
5.22	Normalised flow profiles, vertical velocity component, Material M1 - Fine sand, Silo with flat bottom . . . . .	120
5.23	Normalised flow profiles, vertical velocity component, Material M1 - Fine sand, Silo with 30 degree hopper . . . . .	120
5.24	Normalised flow profiles, vertical velocity component, Material M2 - Coarse sand, Silo with flat bottom . . . . .	121
5.25	Normalised flow profiles, vertical velocity component, Material M2 - Coarse sand, Silo with 30 degree hopper . . . . .	121
5.26	Normalised flow profiles, vertical component, Material M3 - Glass beads, Silo with flat bottom . . . . .	122
5.27	Normalised flow profiles, vertical component, Material M3 - Glass beads, Silo with 30 degree hopper . . . . .	122
5.28	Normalised flow profiles, vertical component, Material M4 - Polyamide, Silo with flat bottom . . . . .	123
5.29	Normalised flow profiles, vertical component, Material M4 - Polyamide, Silo with 30 degree hopper . . . . .	123
5.30	Normalised flow profiles, horizontal velocity component, Material M1 - Fine sand, Silo with flat bottom . . . . .	124

## LIST OF FIGURES

---

5.31 Normalised flow profiles, horizontal velocity component, Material M1 - Fine sand, Silo with 30 degree hopper . . . . .	125
5.32 Normalised flow profiles, horizontal velocity component, Material M2 - Coarse sand, Silo with flat bottom . . . . .	125
5.33 Normalised flow profiles, horizontal velocity component, Material M2 - Coarse sand, Silo with 30 degree hopper . . . . .	126
5.34 Normalised flow profiles, horizontal component, Material M3 - Glass beads, Silo with flat bottom . . . . .	126
5.35 Normalised flow profiles, horizontal component, Material M3 - Glass beads, Silo with 30 degree hopper . . . . .	127
5.36 Normalised flow profiles, horizontal component, Material M4 - Polyamide, Silo with flat bottom . . . . .	127
5.37 Normalised flow profiles, horizontal component, Material M4 - Polyamide, Silo with 30 degree hopper . . . . .	128
5.38 Normalised flow profiles at 3 different heights at 1g, Material M3 - Glass beads, Silo with flat bottom . . . . .	129
5.39 Normalised flow profiles at 3 different heights at 5g, Material M3 - Glass beads, Silo with flat bottom . . . . .	130
5.40 Normalised flow profiles at 3 different heights at 10g, Material M3 - Glass beads, Silo with flat bottom . . . . .	130
5.41 Normalised flow profiles at 3 different heights at 15g, Material M3 - Glass beads, Silo with flat bottom . . . . .	131
5.42 Normalised flow profiles at 3 different heights at 10g, Material M3 - Glass beads, Silo with flat bottom . . . . .	133
5.43 Normalised flow profiles at 3 different heights at 10g, Material M3 - Glass beads, Silo with 30 degree hopper . . . . .	133
5.44 Region of silo used in PIV settlement analysis . . . . .	135
5.45 Density increase as a result of increased gravity . . . . .	136
5.46 Consolidation across the width of silo above the hopper. [mm] . . . . .	136
5.47 Consolidation across the width of silo above the hopper. [mm] . . . . .	137
5.48 Contour maps of consolidation in vertical direction. [mm] . . . . .	137
5.49 Displacement in vertical direction. [mm] . . . . .	138
5.50 Typical FSR construction . . . . .	141

---

5.51 FSR force resistance characteristic trend . . . . .	141
5.52 FSR longevity test . . . . .	142
5.53 Typical data from a pressure pad calibration test . . . . .	143
5.54 Calibration curve for blue pressure sensor using averaged data . . . . .	144
5.55 Calibration curve for red pressure sensor using averaged data . . . . .	145
5.56 Wall pressures during test with coarse sand in flat bottom silo, 50g . . . . .	147
5.57 Wall pressures during test with coarse sand in flat bottom silo, 50g . . . . .	148
5.58 Normal wall pressures at 3 times. LHS, coarse sand in flat bottom silo, 50g . . . . .	148
5.59 Silo wall pressures, coarse sand in silo with 60° hopper at 50g . . . . .	150
5.60 Silo wall pressures, coarse sand in silo with 60° hopper at 50g . . . . .	150
5.61 Normal wall pressures at 3 times. LHS, coarse sand in silo with 60 degree hopper at 50g . . . . .	151
5.62 Silo wall pressures, coarse sand in silo with 30° hopper at 50g . . . . .	152
5.63 Silo wall pressures, coarse sand in silo with 30° hopper at 50g . . . . .	153
5.64 Normal wall pressures at 3 times. LHS, coarse sand in silo with 30 degree hopper at 50g . . . . .	153
6.1 Particle size distribution of material M2, DIN 1164/58 Norm Sand II Klein (1998) . . . . .	159
6.2 Particle size distribution in numerical model . . . . .	160
6.3 Variation of friction angle with confining pressure for physical samples of different initial density . . . . .	162
6.4 Variation of friction angle with confining pressure for DEM samples of different initial density . . . . .	162
6.5 Region used to calculate bulk density in silo with 30 degree hopper . . . . .	165
6.6 Bulk density of granular material in different silos at different factors of gravity . . . . .	166
6.7 Discharge rate through time, silo with flat bottom . . . . .	168
6.8 Discharge rate through time, silo with 30 degree hopper . . . . .	169
6.9 Observed discharge rates compared with Beverloo prediction . . . . .	170
6.10 Flow pattern in model silo with 30 degree hopper . . . . .	173
6.11 Flow pattern in model silo with flat bottom . . . . .	174

## LIST OF FIGURES

---

# Nomenclature

## Roman Symbols

$A$	Cross-sectional area
$A^*$	Silo outlet area minus empty annulus
$a_c$	Centrifugal acceleration
$C$	Coefficient of silo discharge
$c$	Cohesion
$C_{circ}$	Discharge coefficient for circular orifice
$c_{op}$	Patch load solid reference factor
$C_f$	Calibration factor
$C_h$	Horizontal pressure discharge factor
$C_w$	Wall frictional traction discharge factor
$d$	Average particle diameter
$D^*$	Hydraulic mean diameters after empty annulus removal
$D_0$	Circular orifice diameter
$D_H$	Hydraulic diameter
$D_s$	Diameter of silo

## LIST OF FIGURES

---

$e$	Void ratio
$e_0$	Silo outlet eccentricity
$e_f$	Maximum eccentricity of the surface pile during filling
$F$	Hopper wall pressure ratio
$F_e$	Hopper wall pressure ratio during discharge
$F_f$	Hopper wall pressure ratio after filling
$g$	Acceleration due to gravity
$g^*$	Applied gravity
$H$	Hopper height measured from hopper apex
$h_h$	Vertical height between the hopper apex and the transition
$K$	Lateral pressure ratio
$k$	Beverloo grain size coefficient
$K_0$	Lateral pressure ratio (at rest)
$K_a$	Lateral pressure ratio (active state)
$K_p$	Lateral pressure ratio (passive state)
$l$	Length
$N$	Gravity factor
$p$	Horizontal stress
$p_0$	Mean horizontal stress reached at great depth within a silo
$p_{he}$	Symmetrical wall discharge pressure during discharge
$p_{nf}$	Normal pressure on steep hopper after filling
$p_{tf}$	Frictional traction on steep hopper after filling

$p_{vft}$	Mean vertical stress in the solid at the transition after filling
$p_{we}$	Wall frictional traction during discharge
$p_{vf}$	Vertical pressures
$p_{wf}$	Wall friction
$P_E$	Applied pressure
$p_h$	Horizontal pressure
$P_O$	Output pressure reading
$p_v$	Mean vertical stress after filling
$p_{ne}$	Normal pressure on steep hopper during discharge
$p_{te}$	Frictional traction on steep hopper during discharge
$Q$	Mass flow rate
$q$	Vertical stress
$q_0$	Mean vertical stress reached at great depth within a silo
$R$	Radius of rotation
$R^2$	Coefficient of determination
$S$	Hopper shape coefficient
$t_t$	Wall pressure transition time
$U$	Coefficient of uniformity
$u_x$	Horizontal component of velocity
$u_z$	Vertical component of velocity
$u_{x,n}$	Normalised horizontal velocity component
$u_{z,n}$	Normalised vertical velocity component

## LIST OF FIGURES

---

$V_i$	$i^{\text{th}}$ component of velocity
$V_n$	Normalised velocity
$W$	Silo discharge rate due to gravity
$w$	Width
$W_0$	Silo outlet width
$W_s$	Width of silo
$x$	Vertical coordinate upwards from the hopper apex
$z$	Vertical coordinate
$z_0$	Janssen reference depth

### **Greek Symbols**

$\beta$	Hopper half angle
$\gamma$	Unit weight of granular solid
$\mu$	Coefficient of friction
$\mu_{h,eff}$	Effective or mobilized characteristic wall friction coefficient
$\mu_h$	Hopper wall friction coefficient
$\Omega$	Electrical resistance
$\omega$	Angular velocity
$\phi_d$	Angle between stagnant zone boundary and the horizontal
$\phi_i$	Friction angle
$\rho_b$	Bulk density
$\rho_s$	Particle density
$\sigma_i$	Pressure acting in the $i^{\text{th}}$ direction
$\tau$	Shear stress

# Chapter 1

## Introduction

### 1.1 Motivation

The transportation, storage and processing of granular materials affects products in every area of our lives, and has been described as being second only to water as a priority for improved handling<sup>1</sup>.” Knowlton et al. [1994] report that granular materials processes rarely perform above 60% of their design performance and this contrasts with fluids systems that often reach 96% of their design performance. This motivates increased granular materials research and development.

Discharge behaviours and structural loads on silos have been investigated for over a century, but many features of silo design and operation are only partially understood. Consequently a high number of phenomenological and empirical models are used in their design and operation. This results in granular materials handling being less efficient and increasingly encountering reliability problems. This contrasts with other engineering fields including fluid mechanics where analytical models have led to improved efficiency.

In this thesis an investigation into internal silo flow and its response to increased gravities using a silo centrifuge model is presented. This research was conducted

---

<sup>1</sup>Duran J., “Sands, Powders & Grains” Springer, New York. 2000

## 1. INTRODUCTION

---

with the following motivations:

1. A silo centrifuge modelling technique is used because a full-scale silo model requires relatively large amounts of time, money and materials. However, their advantage over smaller models is the creation of industrial stress conditions and greater similarity between experiments and application. Small silo models decrease the cost of resources but fail to produce stress conditions comparable to industrial silos. Silo centrifuge models combine the advantages of each of these scales by producing increased stresses in smaller silos.
2. Varying the gravity enables the constitutive response of a granular material to be investigated from a new perspective. The effect of gravity on silo flow has not yet been quantified.
3. Industry will soon begin mining and transporting granular materials on our moon or from asteroids and will need to predict bulk behaviours at different gravities.
4. Lastly, whilst there are examples of silo centrifuge research investigating wall forces and outlet requirements, there is no published data investigating internal flow conditions of silo centrifuge models. This was probably the result of limits imposed by technology, which have recently been alleviated.

### 1.2 Scope and structure

A silo centrifuge model has been built to investigate silo discharge rates at increased gravities ranging from 1g to 50g. The apparent gravity ( $g^*$ ) is controlled by centrifugal acceleration of a magnitude determined by considering the distance from the region of interest to the axis of rotation. The apparent gravity controls the stresses in the model and the bulk granular response is observed using high-speed video, load cells and pressure sensors on the walls of the model.

The Beverloo correlation is often used to predict the gravity discharge rate of a silo because it is versatile and reasonably accurate. It assumes that the discharge rate is

---

proportional to  $\sqrt{g}$  and this assumption is investigated. The scope is expanded further by considering the velocity profiles and flow patterns during discharge. Velocities at different apparent gravities are normalised by transforming a velocity component  $V_i$  to normalised velocity component  $V_i/\sqrt{g^*W_0}$  where  $g^*$  is the apparent gravity and  $W_0$  is the outlet width.

The work presented in this thesis includes:

1. A state-of-the-art review of silo discharge under the action of gravity.
2. A state-of-the-art review of centrifuge modelling as a tool for silo design and research.
3. Analysis of wall pressures in silos and hoppers according to BS EN 1991-4:2006.
4. Investigation of silo flow during discharge in increased gravity using a silo centrifuge model developed for this research.
5. Investigation of wall pressures before and during discharge using Force Sensing Resistor arrays.
6. Numerical investigation of silo discharge in increased gravity using the Discrete Element Method

This thesis is divided into 7 chapters:

1. This chapter presents the background, objectives and scope of this research.
2. Chapter 2 is a state-of-the-art review of silo discharge, silo centrifuge modelling and an introduction to Discrete Element Modelling.
3. Chapter 3 details the design of a silo according to British design standards.
4. Chapter 4 describes the silo centrifuge model used in the experiments.
5. Chapter 5 presents the results of the silo centrifuge investigations. It includes results pertaining to instrumentation calibration, verification of experimental procedure, silo discharge rates, flow profiles during discharge, settlement and wall pressures before and during discharge.

## 1. INTRODUCTION

---

6. Chapter 6 describes the numerical validation using the Discrete Element Method.
7. Chapter 7 discusses the results and conclusions.

# Chapter 2

## State-of-the-art review

### 2.1 Silo and hopper design principles

Silos and hoppers often give reduced or variable flow rates which increase operating costs or decrease product quality. Therefore improvements in the design and operation of silos is required. The following considerations of silo design and operation are discussed:

- Types of flow pattern and their selection.
- Dimensional design.
- Inlet and outlet considerations.
- Outlet and hopper design.
- Flow rate.
- Measurement of material properties.
- Pressures in the cylinder and hopper.
- Origins of structural loads.

## 2. SILO AND HOPPER DESIGN

---

- Analysis of the lateral earth pressure coefficient.
- Using national design codes.

The usage of the terms silos, hoppers and bins is not universal and varies between industries. In this thesis, the same conventions are used as in the design standard BS EN 1991-4 where a silo is a storage structure of any size containing granular materials. A “hopper” is a converging section at the bottom of the structure where material exits the silo under the action of gravity. “Cylinder” or “vertical section” is any section with a cross section that does not vary with height. “Tank” is reserved for a structure storing liquid and “bin” is not used.

Silos are used to store a wide range of materials and often vary in capacity from a few tonnes to tens of thousands of tonnes. The structural design of silos varies significantly and is a consequence of the materials stored and the conditions required in order to achieve a product of a certain quality under location and pricing constraints. Such is the variability between different materials that a silo designed for one material cannot usually be used to store another material, and never without structural analysis<sup>1</sup>.

Comparisons between fluids and granular materials are common but not usually useful. In contrast to granular materials the laws governing fluids are well understood and this leads to fluids handling being more efficient than for granular materials. Constitutive equations for fluids cannot be modified for granular flow because the processes differ fundamentally. Granular flow is dominated by frictional and shearing forces and involves volume changes. Newtonian fluids are incompressible, have constant viscosity and cannot support shearing forces.

### 2.1.1 Background

The challenges encountered by the silo engineer are highlighted by considering the passage of a grain or particle passing through a silo. During this process it experiences

---

<sup>1</sup>EN 1991-4 1.1.2(4) “ each silo is designed for a defined range of particulate solids properties.”

many different stress states and flow regimes. Therefore they need to be understood by the silo designer.

As material enters the silo it falls under the action of gravity and loses contact with other grains. It falls until it hits either the silo wall or other particles below it and it may bounce, roll or slide until it comes to rest. This will change its orientation which can lead to segregation effects which introduces inhomogeneity into the bulk material. As it is being stored, the particle might be displaced by other particle's entering the silo, and compaction may change the particles shape and contacts. This would also alter bulk material properties.

During discharge the particle will move with a velocity and acceleration dependent on its location in the silo and the silos geometry. Its orientation will change locally and globally and its contacts with surrounding particles may be repeatedly lost and reformed. Contact forces will vary and a large range of stress and strain conditions will be produced in the material. If the silo is discharged under the action of gravity then the particles leave the silo in a state of free-fall, similar to the way they entered. This process illustrates the need for comprehensive understanding of granular materials in silo and hopper design.

### **2.1.2 Flow pattern**

The distribution of particle velocities during discharge constitute a flow pattern. The flow pattern depends on many factors including structural factors (wall roughness and hopper angle), granular material properties (particle size distribution and shape) and processing history (breakage and segregation). The reliable prediction of flow patterns is essential to the efficient design and operation of silos but is currently not possible. Usually, the desired flow pattern fulfils the condition where material that is put into the silo does not leave the silo sooner than material which entered the silo before it.

This can only be achieved if a mass-flow condition exists, which is defined as all the material in the silo moving once the outlet is opened and is shown in Figure 2.1(a). However, even when mass flow is produced, it is difficult to ensure that the

## 2. SILO AND HOPPER DESIGN

---

flow is completely “first in, first out” because this requires that all material above the hopper moves with the same velocity. This is difficult to achieve as the silo walls induce shearing stresses in the material which produces a velocity gradient. The internal shear stresses reduce as distance from the wall increases and thus it is difficult to insure a constant velocity in the cylinder. Silo inserts, careful selection of wall material and hopper angle can alleviate this situation.

The alternative to mass flow is funnel flow. This was defined by [Jenike \[1964\]](#) as a flow pattern in which some material is stationary while the rest is moving. [Rotter \[2005\]](#) subdivided this definition into pipe flow and mixed flow conditions. The definitions introduced by [Rotter \[2005\]](#) are as follows:

If flow does not intersect the silo wall then pipe flow is present. If the flow channel is vertical it is parallel pipe flow (Figure 2.1(b)) and if the channel converges towards the outlet (without intersecting the silo wall) it is taper pipe flow (Figure 2.1(c)). If the flow channel is against the silo wall and parallel it is fully eccentric pipe flow (Figure 2.1(f)) and if it converges along the wall of the silo it is eccentric taper pipe flow (Figure 2.1(g)). If the flow channel intersects any part of the silo wall then the flow condition is mixed flow. If mixed flow is present and the flow channel is symmetric about the centre of the silo then it is concentric mixed flow (Figure 2.1(d)). If instead it is against the wall of the silo across its entire height then it is fully eccentric mixed flow (Figure 2.1(e)). If it intersects the silo walls at a range of heights then it is partially eccentric mixed flow.

Flow pattern selection depends on the material and its intended usage. Flow pattern also greatly influences the forces exerted on the structure during discharge, though design standards do not currently differentiate between each flow category. If funnel flow is permissible then this is often chosen over mass flow because an increased hopper half angle is more space efficient and wear against the walls of the structure is decreased. This decreases construction and maintenance costs. If the following conditions should be avoided then funnel flow will not be suitable:

- Segregation (due to sifting or dusting mechanisms)
- Ageing

- Degradation (spoiling, oxidisation, caking)
- Ratholing

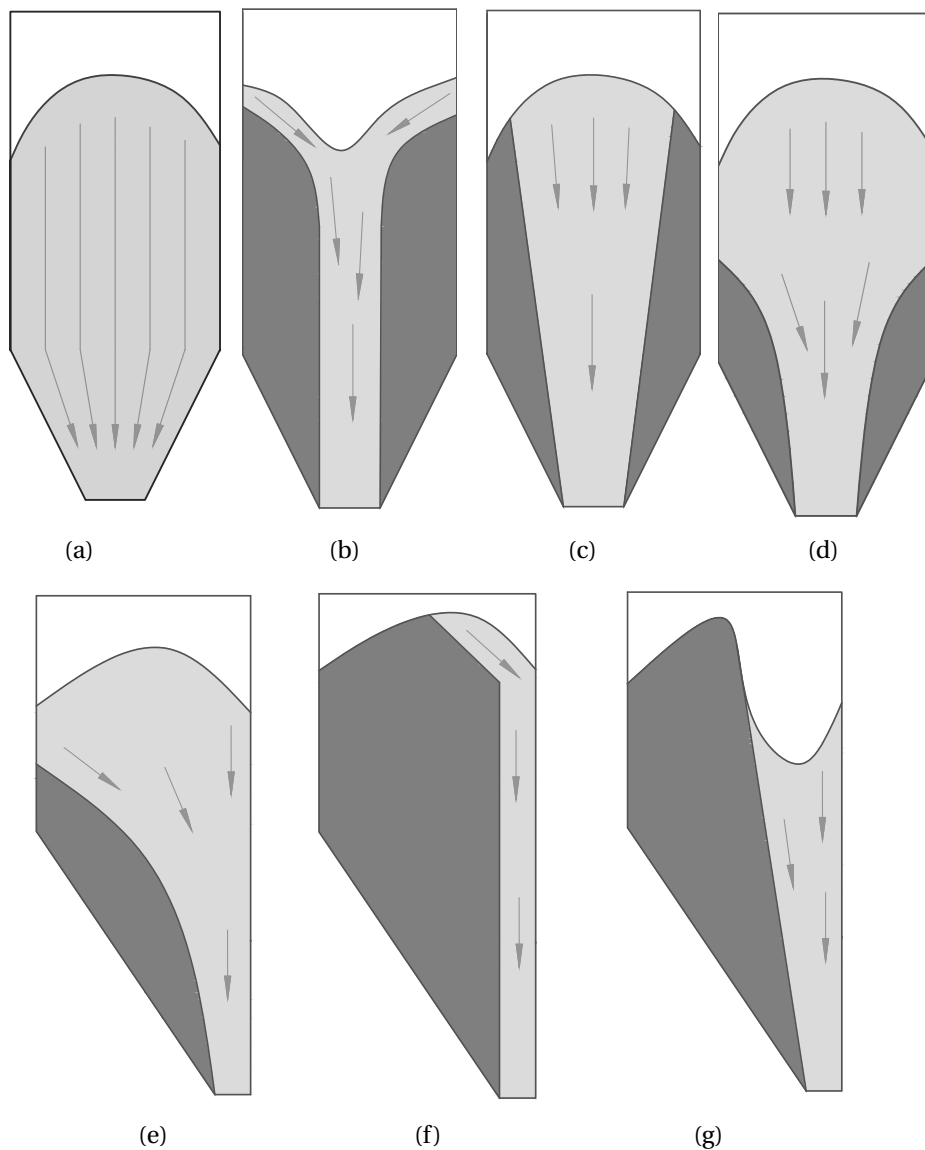


Figure 2.1: Forms of flow pattern: a) Mass flow b) Parallel pipe flow c) Taper mixed flow d) Concentric mixed flow e) Fully eccentric mixed flow f) Eccentric parallel pipe flow g) Eccentric taper pipe flow

## 2. SILO AND HOPPER DESIGN

---

Simple relationships between material properties and the hopper half-angle required to produce mass flow were reported by Jenike in 1964 and are still used today. These relationships allow the prediction of either mass flow or funnel flow for materials of known properties in axisymmetric cones and infinitely long wedges. The input parameters are wall friction angle, friction angle and hopper geometry. Wall friction angle and internal friction angle are often dependent upon a range of other factors including weather conditions, handling history, chemical composition, particle geometry variability, storage time, and hopper wear.

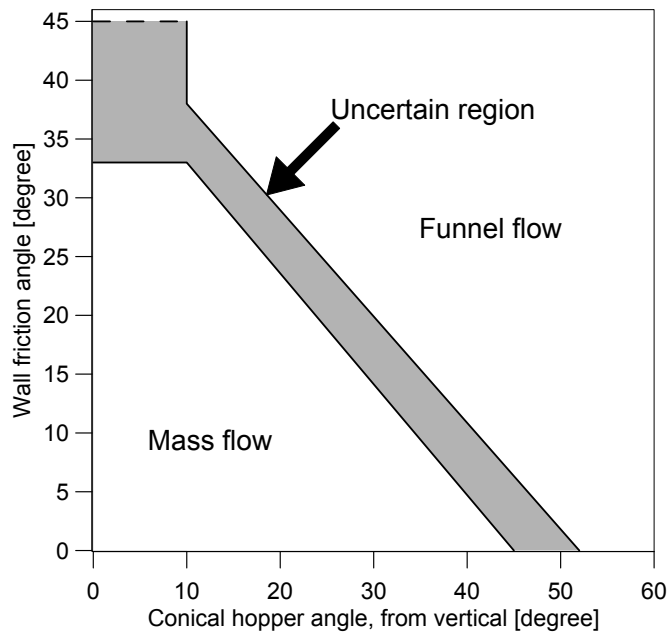


Figure 2.2: Example of Jenike design chart for silos with conical hopper

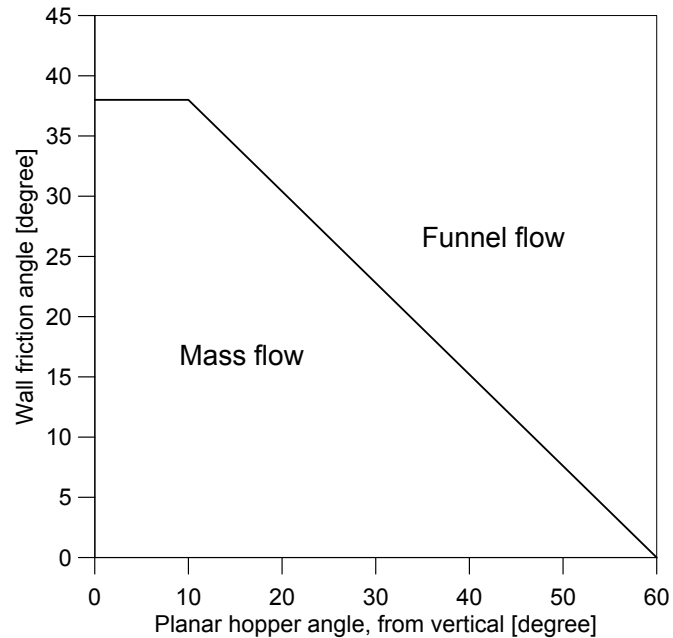


Figure 2.3: Example of Jenike design chart for silos with planar hopper

### 2.1.3 Silo dimensions

The first quantity to be considered when determining the dimensions of a silo is often the weight of material to be stored. The weight is dependent on a number of factors including production or delivery rates, delivery quantity and the required storage time.

The silo volume is calculated by considering bulk density and the maximum weight of the stored material. Bulk density is usually dependent on consolidation pressure and therefore a consolidation test may be required. The same particle size distribution as will be in the silo should be used<sup>1</sup>.

Silo dimensions are selected once the required volume is known. Local factors including access to roads or railways, height of the roof if the silo will be indoors and space restrictions imposed by other equipment should be considered. Build quality is likely to be highest when the silo is manufactured in a dedicated workshop because

<sup>1</sup>This is in contrast to wall friction or cohesivity tests, where using only the fines fraction of the particle size distribution would give a conservative value and is therefore recommended.

## 2. SILO AND HOPPER DESIGN

---

this will minimise imperfections which can avoid problems including stagnant zones or low pressure zones, which affect the operation of the silo and the strength of the structure.

A reasonable height to width ratio for a silo is 1.5 to 4. A ratio above 4 can incur additional expense to mitigate wind and seismic loads. A ratio below 1.5 requires that a large part of the silo volume is in the hopper, which is more expensive to construct and uses space less efficiently.

### 2.1.4 Flow rate

Regardless of what type of material is in a silo, the maximum steady discharge rate varies linearly with the cross-sectional area of the outlet. For coarse and free-flowing materials discharging from a silo with a flat bottom and circular orifice the gravity discharge rate can be estimated using the [Beverloo et al. \[1961\]](#) correlation (Equation 2.1). If a conveyor system is to be used then the gravity discharge rate becomes the maximum possible steady discharge rate.

$$W = C\rho_b\sqrt{g}(D - kd)^{2.5} \quad (2.1)$$

where  $W$  is the maximum steady discharge rate,  $\rho_b$  is the bulk density,  $D$  is the diameter of the circular outlet,  $d$  is the average particle diameter and  $k$  and  $C$  are empirical fitting parameters.

For steep hoppers producing mass flow, the increase in flow rate arising from the hopper geometry can be accounted for by using the similarly derived equation:

$$W = \rho_b A \sqrt{\left( \frac{W_0 g}{[2(1 + m) \tan(\alpha)]} \right)} \quad (2.2)$$

where  $A$  is the cross-sectional area of the outlet,  $W_0$  is the outlet diameter or width,  $m$  is 1 for conical hoppers and 0 for wedges and  $\alpha$  is the hopper half angle (measured

from the vertical) in degrees.

Alternatively, or when funnel flow is expected, the Beverloo correlation can be modified to consider the angle of the hopper and the angle of the stagnant zone:

$$W = W_{Beverloo} F(\alpha, \phi_d) \quad (2.3)$$

$$\begin{aligned} F(\alpha, \phi_d) &= (\tan \alpha \tan \phi_d)^{-0.35} && \text{for } \alpha < 90 - \phi_d \\ F &= 1 && \text{for } \alpha > 90 - \phi_d \end{aligned} \quad (2.4)$$

where  $W_{Beverloo}$  is the predicted discharge rate using the Beverloo correlation and  $\phi_d$  is the angle of the stagnant zone measured from the horizontal. These equations are discussed in detail in Section 2.2.

Flow pattern is determined by conditions in the hopper and around the outlet. The mass flow rate is also determined to a great extent in this region. It is therefore at the outlet that problems with silo flow are created and solved <sup>1</sup>.

A simple example of the influence of hopper design on conditions in the silo cylinder is to consider the requirement for mass flow. For this condition to be present in the cylinder it is also required to exist in the hopper. This occurs when the pressure between the grains and between the grains and the hopper wall is proportional to the distance from the outlet. In order that pressure would decrease, shearing forces must decrease in order to increase flow velocity.

---

<sup>1</sup>This is understood when one considers that whilst the flow direction is from the top to the bottom, flow is initiated at the outlet and propagates upwards away from the outlet until it reaches the top of the stored material.

### **2.1.5 Inlets and outlets**

Inlet design should consider the significance of segregation effects and structural loads. Where these are significant there should be a single central inlet. Segregation effects should be minimised and the loads imposed on the cylinder should be accounted for in the structural design process.

Regarding the outlet, a single central outlet is recommended when segregation or structural loads are significant or when mass flow is required. If multiple outlets are necessary they should be evenly spaced and equidistant from the centre because this minimises segregation and uneven structural loads.

### **2.1.6 Measurement and variability of material properties**

When estimating bulk material properties such as bulk density, friction coefficient or lateral pressure ratio, the supply chain and history of the bulk material needs to be considered. For example if a granular material is produced and stored on site then the variability of its bulk properties can be well-controlled. However, if instead the granular material is transported and stored in an uncontrolled environment (outdoors, for example) then there is much less control over its bulk properties, in which case the variability of key parameters over a number years may be significant even if its source is unchanged.

When a granular material property other than its chemical composition varies, it is difficult to predict what difference this will make to its bulk behaviour. Design codes do not yet account for this directly but instead deal with the uncertainty by introducing a factor of variability. Examples of variability include small changes in moisture content or particle shape.

### **2.1.7 Calculating structural loads**

Interactions between a stored material and the structure bear little resemblance to the mechanisms in fluids acting on tanks. Peak pressures acting on a silo wall vary

with diameter and not height (as might be expected), this is different to fluids where the amount of pressure is so closely related to depth that the term “head” (with units of length) is used to quantify pressure.

Design methods and failure mechanisms to be designed against depend on the construction material, which is usually steel or concrete. Steel silos have thin walls which are stronger in tension than in compression. Buckling is a common failure mechanism and there are various different types of buckling mechanisms to be considered. Concrete on the other hand is strong in compression but has almost no tensile strength. Therefore steel reinforcement must be used to increase tensile strength. Concrete silo failure is often the result of tensile strength being exceeded, this leads to cracking which in turn allows moisture to weaken the reinforcement. This is particularly dangerous in coastal regions.

When designing the silo structure to withstand the pressures created by the bulk material it has often been the peak pressure that is considered the most critical factor. However consideration of spatial and temporal stress variations can be much more significant and should also be verified. Structurally, bending moments and shear loads must be considered as well as the more intuitive circumferential stresses produced from high constant radial pressures.

#### **2.1.7.1 Janssen's equation for cylindrical wall pressures**

The primary technique for describing silo wall pressures is attributed to [Janssen \[1895\]](#). The correlation gives generally good predictions of stresses in vertical walls after filling and is the main descriptor of filling pressure in all design standards including:

- The British design standard - BS EN 1991-4:2006 Eurocode 1. Actions on structures. Silos and tanks
- The German design standard - Einwirkungen auf Tragwerke Teil 6: Einwirkungen auf Silos und Flüssigkeitsbehälter

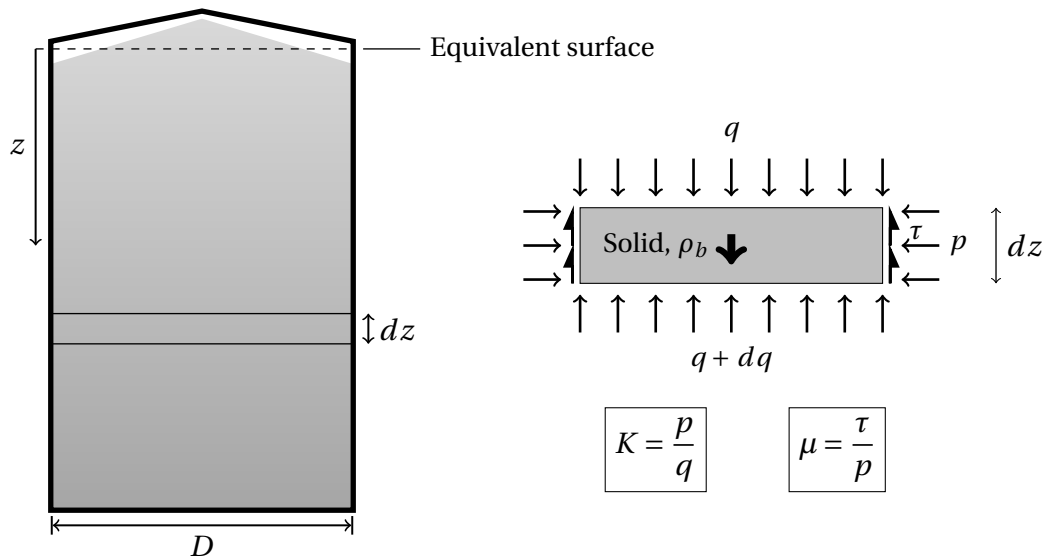


Figure 2.4: Janssen pressure slice

Prior to [Janssen \[1895\]](#) it was well known that silo pressures did not increase linearly with depth but at that time the relationship between pressure and depth had not yet been understood. Janssen calculated the equilibrium of forces acting on a thin horizontal slice of the silo material and a derivation of his theory is presented below:

The vertical equilibrium of a horizontal slice of material stored in a silo is solved by considering the average forces acting on the horizontal surfaces above and below the slice and about the perimeter. This leads to the following equation:

$$(q + \delta q)A + U\tau\delta z = qA + \rho_b A\delta z \quad (2.5)$$

where  $A$  is cross-sectional area  $q$  is vertical stress,  $U$  is the perimeter,  $\tau$  is the shear stress,  $\rho_b$  is unit weight (or bulk density) and  $z$  is the vertical coordinate. Equation 2.5 can be rearranged to give:

$$\frac{\delta q}{\delta z}A + U\tau = \rho_b A \quad (2.6)$$

The vertical stress  $q$  is not required to be uniform because only the average vertical stress is considered. Horizontal equilibrium of the slice requires that force symmetry

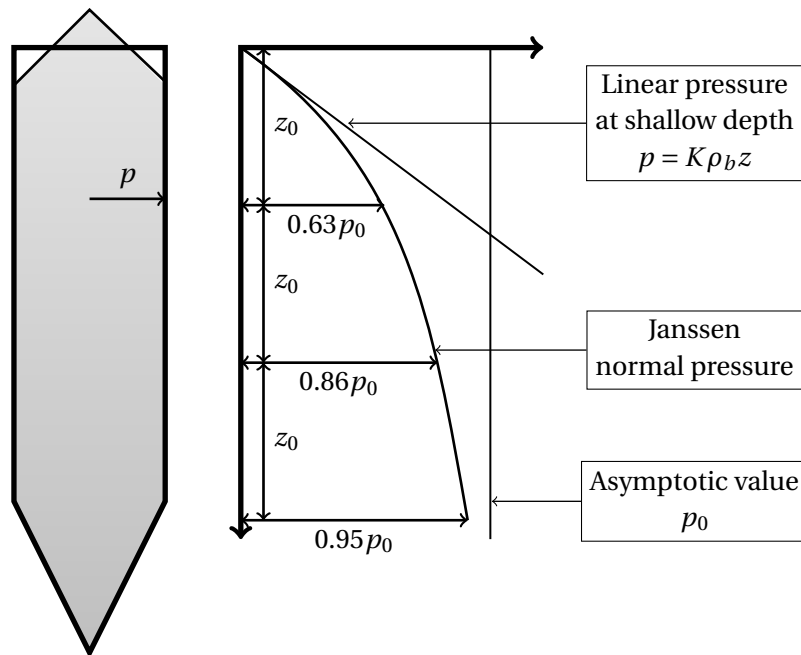


Figure 2.5: Janssen pressure pattern

exists in the wall pressures  $p$ , but the wall pressures do not need to be constant at a given height. Shear stresses on the top and bottom surfaces of the slice are assumed to integrate to 0. The integral of the shear stresses on the top and bottom surfaces is also assumed to be 0.

Two key assumptions are made when calculating the filling pressures:

1. Wall friction is fully developed at every point. This is required so that the mean shear force  $\tau$  can be related to the mean normal pressure  $p$  on the wall using the wall friction coefficient  $\mu$ .

$$\tau = \mu p \quad (2.7)$$

2. The mean normal pressure at the perimeter is related to the mean vertical pressure at the perimeter by the lateral pressure ratio  $K$ .

$$p = K q \quad (2.8)$$

## 2. SILO AND HOPPER DESIGN

---

These two assumptions allow vertical equilibrium to be expressed as

$$\frac{\delta q}{\delta z} + \frac{U}{A} \mu K q = \rho_b \quad (2.9)$$

Considering that the boundary stress at the top of the silo is 0, the pressure distribution can be written as:

$$q = q_0(1 - e^{-\frac{z}{z_0}}) \quad (2.10)$$

when

$$z_0 = \frac{1}{\mu K} \frac{A}{U} \quad (2.11)$$

and

$$q_0 = \rho_b z_0 \quad (2.12)$$

where the vertical coordinate  $z$  has its origin at the geometric centre of the top of the heap. This height is known as the “equivalent surface.”

$z_0$  defines the rate at which the asymptotic pressure is approached and is commonly called the Janssen reference depth.  $q_0$  is the mean vertical stress that is reached at great depth.

Equation 2.10 can be transformed into horizontal pressures using the lateral stress ratio:

$$p = p_0(1 - e^{-\frac{z}{z_0}}) \quad (2.13)$$

where

$$z_0 = \frac{1}{\mu K} \frac{A}{U} \quad (2.14)$$

and

$$p_0 = K \rho_b z_0 = \frac{\rho_b A}{\mu U} \quad (2.15)$$

Figure 2.1.7.1 shows the key features of this pressure distribution. Three important relationships can be seen in equation 2.13.

- $p \propto q \propto \rho_b$  - Pressure varies linearly with bulk weight and it is therefore important that this is accurately determined.
- $z_0 \propto \sqrt{A}$  - The Janssen reference depth varies with cross-sectional area multiplied to the power of one half.
- $z_0 \propto 1/K$  - The Janssen reference depth is proportional to the inverse of the lateral stress ratio.

### 2.1.7.2 Hopper Pressures

Janssen's silo pressure theory is only applicable to vertical silo sections. A complementary theory for converging sections was derived by Dabrowski in 1957 and is attributed to Walker [1966]. This is the theory used in EN 1991-4 (2007).

The same notation is used as with Janssen's silo pressure theory. The mean vertical stress in the material is  $q$ , the mean normal pressure against the hopper wall is  $p$ ,  $\tau$  is the mean wall friction traction and  $\rho_b$  is the bulk density. The angle of the hopper is denoted  $\beta$  and is measured from the vertical at the steepest part of the hopper. The height of the hopper is denoted  $H$  and is measured from the apex of the walls.  $x$  is the vertical coordinate and varies from 0 to  $H$ .

Hopper radius and cross-sectional area can therefore be expressed as a function of  $x$  in the following ways:

- The distance from the central axis to the nearest point on a wall is  $r = x \tan(\beta)$
- Cross-sectional area as a function of height is  $A = \pi r^2 = \pi x^2 \tan^2(\beta)$  for a conical hopper
- Cross-sectional area as a function of height is  $A = 4r^2 = 4x^2 \tan^2(\beta)$  for a pyramidal hopper

## 2. SILO AND HOPPER DESIGN

---

- The perimeter of a horizontal slice is  $U = 2\pi r = 2\pi x \tan(\beta)$  for a conical hopper
- The perimeter of a horizontal slice is  $U = 8r = 8x \tan(\beta)$  for a pyramidal hopper

Making groups of common factors allows simplified expressions. If for a conical hopper  $k_1 = \pi$  and  $k_2 = 2k_1$ , and for a pyramidal hopper  $k_1 = 4$  and  $k_2 = 2k_1$  then;

$$A = k_1 x^2 \tan^2(\beta) \quad (2.16)$$

$$U = k_2 x \tan(\beta) \quad (2.17)$$

This allows vertical equilibrium to be expressed concisely. Equation 2.18 shows vertical equilibrium with small terms eliminated:

$$x \frac{\delta q}{\delta x} = 2\left(p + \frac{\tau}{\tan(\beta)} - q\right) - \rho_b x \quad (2.18)$$

The same two assumptions as in the Janssen equation are used:

- Wall friction is fully developed at every point during discharge, and shear at the wall is proportional to the normal pressure so that  $\tau = \mu_h p$ .
- The mean pressure normal to the hopper wall is proportional to the mean vertical stress in the material such that  $p = Fq$ , where  $F$  is the hopper pressure ratio
- Additionally, when the material is not moving, there is a smaller friction coefficient  $\mu_{h,eff}$

Inserting these relationships into Equation 2.18 gives

$$x \frac{\delta q}{\delta x} - nq = -\rho_b x \quad (2.19)$$

where

$$n = 2[F + F\mu_h \cot(\beta - 1)] \quad (2.20)$$

The mean vertical stress at the top of the hopper section can be found using Equation 2.13. The equation can then be solved by considering the top boundary condition where  $x = H$  and  $q = q_t$ .

This gives

$$q = q_t \left(\frac{x}{H}\right)^n + \frac{\rho_b}{(n-1)} \left( \left(\frac{x}{H}\right) - \left(\frac{x}{H}\right)^n \right) \quad (2.21)$$

Similarly to finding stresses in the vertical sections, the pressures normal to the hopper are found using

$$p = F \left( q_t \left(\frac{x}{H}\right)^n + \frac{\rho_b}{(n-1)} \left(\frac{x}{H}\right) - \left(\frac{x}{H}\right)^n \right) \quad (2.22)$$

Equation 2.22 shows two sources of loading in the hopper which are the overburden from the vertical section and the self-weight of material in the hopper. High local pressures can occur if the cylinder is tall,  $q_t \approx q_0$  and  $F$  is high. When  $F$  is high,  $\beta$  is small and  $\mu$  is large, then  $n$  is also large. This has the result of a large peak in the pressure distribution at the transition.

The most common cause of structural failure of hoppers is rupture at the transition. This is not due to high internal hopper pressure but stresses resulting from excessive vertical pressures in the vertical section. This can be caused by unexpected variations in material properties which increase  $q_t$ .

The factors controlling fully mobilised friction are hopper smoothness and slope. The hopper is classified as steep if the solid slides which will occur if the following condition is met:

$$\tan(\beta) < \frac{1 - K}{2\mu_h} \quad (2.23)$$

where  $\mu_h$  is the fully mobilised wall friction coefficient of the hopper.

The question of whether a hopper is steep or shallow is significant because the pressure distribution against the hopper wall changes significantly. This is shown in section [2.1.7.3](#).

### **2.1.7.3 Influence of flow patterns during discharge**

During the 1960's the influence of flow pattern on structural forces began to be investigated. Funnel flow during discharge produces smaller stresses than for a mass flow system. This is because a smaller mass of material is in motion, and the stress maxima and minima will not be as pronounced because the forces must be transmitted from the moving material to the walls of the structure via the static material in between, which has a damping effect. The work of Jenike [1964] was instrumental in achieving wide spread recognition of the effects of flow pattern on structural forces. EN 1991-4 (2007) divides silo flow under symmetrical conditions patterns into 3 categories. These are shown in figure [2.1.2](#).

### **2.1.7.4 Using the lateral earth pressure ratio K**

Janssen's silo pressure theory is a reliable predictor of silo filling pressures. Adoption of the theory is made easier by its use of only 3 material parameters, 2 of which were easy to quantify - bulk density and wall friction coefficient. However measuring the lateral earth pressure ratio  $K$  is not as simple.

The lateral earth pressure coefficient was used in 1857 by William Rankine as part of his earth pressure theory for use in designing retaining walls. This theory makes use of horizontal and vertical pressure ratios and provides limiting values of  $K$  as a function of the angle of internal friction ( $\phi_i$ ). This is the material's angle of internal friction which is found using a direct shear test. Because earth is a granular material

and limiting values of  $K$  could be found indirectly, it was intended that Rankine's earth pressure theory would be used for the design of silos and replace the need to measure  $K$  directly.

The two limiting  $K$  values are known as the Rankine earth limits and are defined as

$$K_a = \frac{1 - \sin(\phi)}{1 + \sin(\phi)} \quad (2.24)$$

for the active state, and

$$K_p = \frac{1 + \sin(\phi)}{1 - \sin(\phi)} \quad (2.25)$$

for the passive state.

Rankine earth pressure theory assumes that the soil is cohesionless, the wall is frictionless, the soil-wall interface is vertical, the failure surface on which the soil moves is planar and the resultant force is angled parallel to the backfill surface.

The active pressure state is achieved when the retaining wall moves away from the soil and the soil relaxes and deforms to the point where the maximum strength of the soil is reached and it is about to fail in extension through shearing. It therefore represents the minimum lateral pressure that must be applied before plastic deformation occurs.

The passive pressure state is achieved when the retaining wall moves towards the soil, increasing the compressive force on the soil such that the limit of the compressive strength of the soil (failure in compression) is reached. It therefore represents the maximum compressive stress that may be applied before the soil deforms plastically.

Thus the active and passive pressure states represent the limit states between elastic and plastic deformation in tension and compression.

A third pressure state exists called the at rest pressure state. This is present when a soil is retained by a rigid wall and no lateral movement occurs. The ratio of vertical to horizontal pressure in this state is denoted  $K_0$ .

When Janssen's silo pressure theory was first used it was assumed that material stored in a silo would be in an active pressure state, leading to a small value of  $K$  and thus small maximum lateral pressures. This assumption is incorrect and using the active

## 2. SILO AND HOPPER DESIGN

---

stress assumption gives values of  $K$  that are too small. Unfortunately this was not quickly corrected there was a period of almost 60 years during which the reason for the structural failures of silos was uncertain.

Change came as a result of an increased appreciation of Rankine's earth pressure theory and the suggestion that the strains produced in the structure as a result of filling may be small enough to keep the material within its plastic limits, in an elastic state. This initial filling condition is denoted  $K_0$  and is assumed to be approximately 50% larger than  $K_a$ .

The value of  $K_0$  is approximated as  $1 - \sin(\theta_i)$  after [Jaky \[1948\]](#). More information about this approximation is in [Muir Wood \[1990\]](#).  $K_0$  is valid in the ideal state where the principle stresses are uniform and act in the vertical and horizontal directions. Since there are shear stress gradients originating from friction with the silo wall, there is neither horizontal principal stresses or uniform principal stresses. Therefore a new stress state is denoted with a lateral pressure coefficient denoted  $K_f$ . This shows the benefit of measuring  $K_f$  directly, however for design purposes it may be evaluated as  $K_f = 1.1(1 - \sin\theta)$  according to EN 1991-4 (2007). The most common value of  $K$  is 0.4 and this will be correct when the friction angle of the material ( $\theta$ ) is between 23 and 28 degrees.

### 2.1.8 Design codes

The world's first design code for silos was DIN 1055-6 (1964). At this time most silos were constructed using concrete and it was assumed that the critical design criterion was circumferential stress, since concrete is strong in compression and buckling is unlikely. Consequently  $K$  was often overestimated and  $\mu$  was underestimated in order to protect against bursting.

As metal silos became more common, consideration of the vertical forces in the structure became more important. Design codes containing material properties suitable for concrete silos were not suitable for designing metal silos because when the critical design criterion is buckling under compressive load,  $K$  and wall friction should both be overestimated. Thus, it became clear that a range of material proper-

ties needed to be accounted for based upon factors ranging from the material itself to the equipment used to process it. This was first accommodated by using empirical multiplication factors.

The current editions of the design codes have improved upon this and now include upper and lower bounds of material properties. The bounds allow for the different structural failure mechanisms and also the variability that is found between different samples of a granular material.

In EN 1991-4 (2007) a central value for each parameter is specified along with a specific conversion factor that incorporates the scatter that is likely to be observed. The conversion factor is designed to include values within a 10% to 90% probability.

The size of a silo will affect which design considerations are important. For this reason, BS EN 1991-4 distinguishes between 3 categories of silos based on the mass of stored material. The design requirements differ depending on whether a silo can store up 1000, 10,000 or 100,000 tonnes and also differentiates between silos of four slenderness ratios. These are “squat silo”, “retaining silo”, “slender silo” and “intermediate slenderness silo”. In EN 1991-4 (2007) a formal methodology of establishing the variability of a material is given in Appendix C.

## 2.2 Granular discharge through an orifice

The rate at which granular material discharges from a silo under the action of gravity is of fundamental importance. The most widely used method to predict silo discharge rate from silos with a flat bottom was developed by [Beverloo et al. \[1961\]](#). [Nedderman \[1992\]](#) reports that the discharge rate was first investigated at the beginning of the 20<sup>th</sup> and experimentalists found a small dependency on the discharge rate  $W$  with height  $H$  of the form  $W \propto H^{0.04}$  and that the relationship of discharge to outlet diameter was found to be close to  $W \propto D^3$  [Ketchum \[1907\]](#). This was found by plotting  $\ln W$  against  $\ln D_0$ . A value of  $W \propto D_0^{2.96}$  was emphasised because of its relationship to the dependence on  $H^{0.04}$ .

In this way early models for silo discharge rate took the form:

$$W = C' \rho_b \sqrt{g} D_0^{2.96} H^{0.04} \quad (2.26)$$

A comparison of different discharge models is conducted by [Fedler \[1988\]](#). He compared the models of [Fowler and Glastonbury \[1959\]](#), [Beverloo et al. \[1961\]](#), [Ewalt and Buelow \[1963\]](#) and [Gregory and Fedler \[1987\]](#). Each model uses different assumptions and simplifications.

[Fowler and Glastonbury \[1959\]](#) assume that the coefficient of friction is a function of the granular shape, size, roughness and void ratio. These properties are incorporated into one coefficient because they are difficult to measure when material is in a silo. Using only the “primary physical factors” that influenced the materials angle of repose, and using dimensional analysis, the following correlation is reported:

$$W = 0.236 \left( \frac{D}{d} \right)^{0.185} \left( \rho_b A \sqrt{2gD} \right) \quad (2.27)$$

where  $W$  is the mass flow rate ( $g/s$ ),  $D$  is the orifice diameter ( $cm$ ),  $d$  is the particle diameter ( $cm$ ),  $A$  is the orifice area ( $cm^2$ ),  $g$  is the gravitational constant ( $cm/s^2$ ) and  $\rho_b$  is the material bulk density ( $g/cm^3$ ).

This correlation suggests that the mass flow rate is linearly related to bulk density

and is a function of the orifice diameter raised to the power of 2.685.

[Beverloo et al. \[1961\]](#) uses dimensional analysis and experimental data to correlate mass flow rate, outlet diameter and grain size. The discharge rate is found to be dependent on the diameter of the orifice to a 5/2 power law.

This relationship is well-established for large circular orifices where the diameter is many times the diameter of the grains falling through it. For small orifices [Beverloo et al. \[1961\]](#) accurately predicts discharge rate only when an additional fitting parameter is included.

[Ewalt and Buelow \[1963\]](#) developed a model using shelled corn with different moisture contents discharging through orifices up to 15cm wide. They report that the discharge rate is best described as an exponential function of the form  $W = aD^b$  where  $a$  and  $b$  are constants and  $D$  is the orifice diameter.

The effect of moisture level was investigated and found not to influence the value of  $b$ , which is 3.10. The coefficient  $a$  had an average value of 0.1196. This is a simplistic model where the effect of all material properties, even bulk density, are incorporated into two constants.

The model created by [Gregory and Fedler \[1987\]](#) considers the effect of viscous and inertial forces by distinguishing between laminar and turbulent flow and is unique in this regard.

$$\text{Laminar Flow: } W = \frac{\pi}{16} \frac{gD^2}{k} D^3 \quad (2.28)$$

$$\text{Turbulent Flow: } W = \frac{\pi}{8} \frac{g^{0.5}}{k} D_b^{1.5} D^{2.5} \quad (2.29)$$

where  $k$  is a resistance factor.

[Fedler \[1988\]](#) compares these models to experiments with 5 types of material. The models by [Beverloo et al. \[1961\]](#) and [Gregory and Fedler \[1987\]](#) were found to give the best agreement with experimental data. The inclusion of terms to consider a boundary layer and the bulk density greatly increase the versatility and accuracy of the models. The Beverloo correlation is widely used because it is dimensionally consistent, uses easily evaluated material properties and has been shown to give

reasonably accurate results across a wide range of materials and orifice diameters.

### 2.2.1 Derivation of the Beverloo discharge correlation

The rate at which a granular material discharges from a silo during emptying is most reliably predicted using the Beverloo correlation. It is derived using dimensional analysis and it can be shown how the form of the equation is related to physical processes that may be controlling discharge by using the analogy of a collapsing arch. The Beverloo model is useful for a great range of industrial applications but becomes inaccurate at very low ratios of orifice diameter to particle diameter, and when particle diameter is very small. It is recommended for the following range of outlet to particle diameter ratios:

$$D_0/6 > D > 400\mu m \quad (2.30)$$

From intuition, the most important terms required to compute the discharge rate of a silo include the density of the material  $\rho_b$ , the height of the stored material  $H$ , the diameter  $D_s$  or width  $W_s$  of the silo, the orifice diameter  $D_0$ , the average particle diameter  $d$ , the coefficient of friction  $\mu$  and the acceleration due to gravity  $g$ . When a hopper is present, its inclination is also considered. The angle of inclination  $\beta$ , called the hopper half angle is measured from the vertical and is equal to half the angle of the virtual hopper apex.

One of the first surprising properties of silo discharge and an important distinction between granular solids and fluids is the independence of discharge rate and the height of the stored material above the silo outlet. Another distinction is the independence of the discharge rate and the diameter of the silo<sup>1</sup>.

Discharge will stop when the silo outlet becomes too small compared to the size of the particles passing through it. The minimum ratio  $D_0/d$  required for flow depends on particle shape to an extent and how the mean diameter is calculated and ranges

---

<sup>1</sup>These independences are true in all normal conditions. At extreme values when  $H \lesssim 2D_0$  or when  $D \lesssim 2D_0$  these relationships are not true.

from 6 – 10. When  $D_0/d > 10$  the silo will discharge without jamming.

Considering these limits, the rate of discharge from a silo is dependent only on density, gravity, outlet diameter and material friction.

$$W = f(\rho_b, g, D_0, \mu) \quad (2.31)$$

Considering the principles of dimensional analysis and understanding that the coefficient of friction is dimensionless, the only correct form of the relationship between discharge and these variables is

$$W = C\rho_b\sqrt{g}D_0^{5/2} \quad (2.32)$$

where  $C$  is a coefficient and a function of the coefficient of friction.

Plotting this relationship for a range of orifice diameters in the form  $W^{5/2}$  against  $D_0$  shows that the relationship is linear with a non-zero intercept of  $W^{5/2}$  on the  $D_0$  axis. Tests with mono-sized particles of different diameters show that the size of the intercept is proportional to particle diameter  $d$  and leads to the following correlation:

$$W = C\rho_b\sqrt{g}(D_0 - kd)^{5/2} \quad (2.33)$$

where  $C$  is almost independent of the particle friction coefficient and  $k$  usually ranges from 1.4 for smooth spherical particles and increases with particle angularity.

## 2.2.2 The collapsing arch analogy

The physical origins of the Beverloo correlation can also be explained by considering a collapsing arch just above the outlet. It has been suggested that the Beverloo correlation exists because there is a free-fall zone above the silo outlet limited by an arch spanning the orifice. Above the arch the particles are well-packed and have

very small velocities. Below the arch the particles are in free-fall and accelerate under the action of gravity. If the size of the arch is proportional to the size of the outlet then the velocity of the particles falling through the outlet can be found by calculating the velocity of a particle falling without initial velocity from a distance that is proportional to the height of the outlet.

This analogy encounters problems when it is considered in more detail. [Nedderman \[1992\]](#) argues that the collapsing arch analogy cannot be completely correct due to the following argument. On the surface of the arch, the normal stress becomes zero, and above the arch, the material is subjected to forces resulting from its own mass and also from internal material stresses. Below the arch the material is subjected only to its own body forces.

Therefore as a particle falls through the arch it would experience a reduction in the forces acting on it and its acceleration would reduce. This is incompatible with the acceleration needed to dilate the material and initiate free-fall. The collapsing arch theory might be improved by including one or more of the following conditions:

- i A stress discontinuity within the material replaces the free-fall arch.
- ii The stress gradient is zero at the free-fall arch. i.e.  $d\sigma_{rr}/dr = 0$  on  $r = r_0$
- iii Dilation is a gradual process happening across a region close to the outlet but not solely at the outlet.

Experimental work shows that item (iii) is possibly a factor, and thus it is not possible to unambiguously identify a free-fall arch.

### 2.2.3 The empty annulus

Discharge through different sizes and shapes of orifice was investigated by [Brown and Richards \[1960\]](#) and the concept of an empty annulus was first presented. The area through which solids can flow is less than the total orifice area because if a particle was less than  $d/2$  distance from the edge of the orifice it could not fall out of

---

the silo without first moving in the horizontal direction. For spherical particles, the maximum interference to flow would cause a reduction of the orifice size of  $(D - d)$  because no particle could lay on the orifice edge past a distance of  $d/2$ . This implies that value of  $k$  in the Beverloo correlation should be equal to 1.0. However a better fit to experimental data is found when  $k=1.4$ . This shows that other factors need to be considered such as surface roughness and particle shape. The physical meaning of the term “ $kd$ ” has been the subject of much research, for example, [Zhang and Rudolph \[1991\]](#), [Nedderman and Laohakul \[1980\]](#) [Brown and Richards \[1960\]](#) and [Brown and Richards \[1970\]](#). Suggestions about the physical origin of the  $kd$  term include the existence of a shearing layer in the material approaching the orifice.

Because of the experimental procedure used by Beverloo et al. the correlation uses the term  $D - kd$  however it would also be possible to include the term  $d/D$ . The  $kd$  term is compatible with the concept of an area next to the orifice boundary through which fewer particles fall than compared to the centre of the orifice. Whilst a localised reduction in discharge rate has been observed, the mechanisms producing this behaviour are unknown.

Arguments that  $k$  should not equal 1 are based on the following assumptions:

1. The effective diameter is not  $D_0 - d$
2. The centre of mass of a particle is not its geometric centre
3. The particle is not effectively spherical

Whatever the physical meaning of the term  $kd$ , it is clear from geometrical considerations that the porosity of a granular material will increase next to a boundary wall and that therefore the concept of an empty annulus and reduced effective diameter of an orifice is helpful.

The Beverloo equation is phenomenological because the value of the coefficients required to produce the best fit to data should be established for each type of material and an equation derived only from fundamental principles and material properties is not yet possible.

One limitation of the Beverloo correlation is that it does not consider the effect of hopper inclination. An alternative correlation to Beverloo was developed by Johanson (Equation 2.2). This correlation assumes mass flow and includes hopper inclination but does not consider particle size (though the concept of an empty annulus could easily be implemented)<sup>1</sup>.

Another method to predict the gravity discharge rate of a silo with a hopper is to combine the work of [Rose and Tanaka \[1956\]](#) and [Beverloo et al. \[1961\]](#). This has been recommended by the British Materials Handling Board, 1987. The study by [Rose and Tanaka \[1956\]](#) pre-dates [Beverloo et al. \[1961\]](#) and reports on the correlation between discharge rate, hopper angle and the inclination of the stagnant zone. It may be combined with the work by Beverloo et al. as follows:

$$W = W_B F(\beta, \phi_d) \quad (2.34)$$

$$\begin{aligned} F(\beta, \phi_d) &= (\tan \beta \tan \phi_d)^{-0.35} && \text{for } \beta < 90 - \phi_d \\ F &= 1 && \text{for } \beta > 90 - \phi_d \end{aligned} \quad (2.35)$$

### 2.2.4 Bulk density measurements for discharge prediction

Intuition would suggest that the value of bulk density to be used when predicting discharge rate should be the same as the bulk density of the material in the silo. However, experiments have shown that the discharge rate is the same for loosely filled and compacted material. This is explained using critical state theory which states that when material begins to move it will dilate and the bulk density will adjust to a value compatible with the flowing state that results from dilation.

In practice, the requirement to calculate this value of bulk density is lessened by the previous requirement to define the value of constant  $C$  for each material. As the true density of a material during discharge will be some factor of its stated bulk density, this factor can be incorporated into the value of  $C$ . When using SI units and when the

---

<sup>1</sup>No other information about its derivation or development could be found and therefore this method is not discussed further.

value of  $\rho_b$  is calculated for a loosely-filled silo, the value of C is rarely significantly different to 0.58 for a circular orifice or 1.03 for a slot orifice, despite its supposed dependency on the coefficient of wall friction.

### 2.2.5 Discharge rate from hoppers

Material will discharge from a silo with a hopper quicker than from a flat-bottomed silo. The discharge rate from a mass flow hopper is larger than from a hopper producing funnel flow.

Rose and Tanaka [1956] reported the following correlation (pre-Beverloo)

$$Q \propto (\tan \beta \tan \phi_d)^{-0.35} \quad (2.36)$$

when  $\beta < 90 - \phi_d$ , where  $\phi_d$  is the angle between the stagnant zone boundary and the horizontal.

This can be incorporated into the Beverloo equation in the following way:

$$W = W_B F(\beta, \phi_d) \quad (2.37)$$

where  $W_B$  is the discharge rate using the Beverloo correlation and  $F(\beta, \phi_d)$  is

$$F(\beta, \phi_d) = (\tan \beta \tan \phi_d)^{-0.35} \quad \text{for } \beta < 90 - \phi_d \quad (2.38)$$

$$F = 1 \quad \text{for } \beta > 90 - \phi_d \quad (2.39)$$

There is not yet any reliable method for predicting  $\phi_d$ . It can be determined experimentally or an assumed value of  $45^\circ$  may be used.

### 2.2.6 Discharge through non-circular orifices

The Beverloo correlation may be modified for rectangular outlets. The correlation then takes the form:

$$W = C\rho_b\sqrt{g^*}(l - kd)(W_0 - kd)^{1.5} \quad (2.40)$$

where  $l$  is the thickness of the silo and  $W_0$  is the width of the outlet.

This is formulated by maintaining dimensional consistency and considering that the flow rate increases linearly with silo thickness  $l$ .

Values for  $C$  for non-circular outlets can be calculated using a suggestion by [Fowler and Glastonbury \[1959\]](#) that the flow rate is proportional to the product of the orifice area and the square root of the mean hydraulic diameter. For a rectangular outlet this is  $C_{slot} = C_{circ}(4\sqrt{2}/\pi)$ . This conversion is now derived:

The hydraulic diameter is defined as

$$D_H = \frac{4A}{U} \quad (2.41)$$

where  $A$  is the cross-sectional area and  $U$  is the perimeter of the orifice.

Using the concept of the empty annulus to adjust the cross-sectional area and perimeter of the orifice, the following relationship can be expressed:

$$W \propto A^* \sqrt{D_H^*} \quad (2.42)$$

where  $A^*$  and  $D_H^*$  are the area and hydraulic mean diameter of the orifice after removing the empty annulus.

For a slot orifice of dimensions  $wl$  the expression becomes

$$A^* = (w - kd)(l - kd) \quad (2.43)$$

and

$$D_H^* = \frac{4(w - kd)(l - kd)}{2(w + l - 2kd)} \quad (2.44)$$

if  $l > 3w$ , then  $D_H^* \approx 2(w - kd)$  and

$$W = \frac{4\sqrt{2}}{\pi} C_{circ} \rho_b \sqrt{g}(l - kd)(w - kd)^{1.5} \quad (2.45)$$

This formula agrees to within 1% with experimental data by [Myers and Sellers \[1977\]](#) who measured the flow rate of spherical glass beads from wedge hoppers.

### 2.2.7 Effect of gravity on static and dynamic angles of repose

The effect of gravity on static and dynamic angle of repose seems to be the subject of conflicting evidence. [Brucks et al. \[2007\]](#) report that angle of repose is independent of  $g$ . However this is not confirmed by either [Kleinhaus et al. \[2011\]](#) or the experiments in this thesis. [Kleinhaus et al. \[2011\]](#) report that the static angle of repose decreases with apparent gravity and that dynamic angle of repose increases with apparent gravity. I observe that the static angle of repose decreases with increasing gravity.

## 2.3 Principles of centrifuge modelling

In this section, the mechanical principles of centrifuge modelling are shown. The equivalent weight of a model is discussed first, followed by the gravitational field and then Coriolis effects.

According to equation 2.46, a model with a mass of  $20\text{kg}$  rotated in a centrifuge at a radius of  $r = 1.0\text{m}$  with an angular velocity of 95 rotations per minute (rpm) will be accelerated at  $99.0\text{m/s}^2$ , or 10.09 earth gravities. The force exerted on the model by the centrifuge arm in order to cause this acceleration will be  $20\text{kg} \times 99.0\text{m/s}^2 =$

## 2. SILO AND HOPPER DESIGN

---

1980*N*

$$a_c = r\omega^2 \quad (2.46)$$

If the model is viewed from an external reference frame it will be constantly accelerating towards the centre of the centrifuge, however if the model is viewed from a point with a position that does not change relative to the model (from the model's reference frame) then it will appear to be at rest. The force exerted by the model on the centrifuge arm will be equal to the force exerted by the centrifuge arm on the model, according to Newton's third law.

A model outside of the centrifuge and resting on the Earth's surface is referred to as the prototype. If it has a mass of  $10.09 \times 20\text{kg}$  then the force it exerts on the surface on the Earth, and which the Earth's surface exerts on the model will be equal to  $10.09 \times 20\text{kg} \times 9.81\text{m/s}^2 \approx 1980\text{N}$ . Therefore when acceleration is increased by the same factor as model geometry is decreased, the prototype on the Earth's surface and the model in the centrifuge experience the same physical forces, and that these forces are exerted across the surfaces contacting the model or prototype with the Earth or centrifuge. Stresses are not applied to the top surface of either the model or the prototype and thus the internal stresses develop across the height of both bodies in the same natural way. The difference between the model and prototype is described by the change in the length dimension, which varies by a factor of  $N$ .

The second consideration is the variation of acceleration across a centrifuge model, which is inevitable and is the result of centrifugal acceleration being proportional to the radius of rotation. Some parts of a centrifuge model are nearer the axis of rotation than others and thus there are small differences in the acceleration experienced at different points. In order to calculate the difference between material stresses produced in a uniform gravitational field and a radially increasing gravitational field, the cumulative effect of the difference between the body forces produced by the two fields must be considered.

Let the model and the prototype both have a free surface where the vertical stress is 0. According to Schofield [1980], if  $R$  is the target radius of the centrifuge model then there will be a correct pressure  $p_V$  in the  $1/N$  scale model at radius  $R$ . Let the

distance between  $R$  and the free surface of the model be  $aR$ . In the centrifuge model the vertical stress at depth  $R$  is found by integrating between the free surface and the target radius:

$$p_V = \int_{R(1-a)}^R \rho_b r \omega^2 dr = \frac{\rho_b \omega^2}{2} R^2 a(2-a) \quad (2.47)$$

The same vertical pressure is produced in a prototype outside of the centrifuge at a depth of  $NaR$ . Therefore  $p_V = \rho g NaR$  and

$$\frac{Ng}{R\omega^2} = \frac{2-a}{2} \quad (2.48)$$

Between the free surface and target radius, the stress in the model will be a little less than in the prototype over the same relative range. If a point half-way between the free surface and target radius is considered, then the vertical stress in the model is found to be:

$$p_V = \int_{R(1-a)}^{R(1-a/2)} \rho_b r \omega^2 dr = \frac{\rho_b \omega^2}{2} R^2 a(1-3a/4) \quad (2.49)$$

If this quantity is compared with the vertical stress in the prototype at the corresponding depth of  $z = NaR/2$ , then the vertical stress is  $p_V = \rho_b g NaR/2$  and the error may be computed as:

$$\left( \frac{\rho_b g n a R / 2}{\rho_b \omega^2 R^2 a (1 - \frac{3}{4} a) / 2} \right) - 1 = \left( \frac{ng}{R\omega^2} \frac{4}{4-3a} \right) - 1 = \left( \frac{2-a}{2} \frac{4}{4-3a} \right) = \left( \frac{a}{4-3a} \right) \quad (2.50)$$

In this thesis the target radius of the silo centrifuge model corresponds to the distance between the rotational axis and the silo outlet. During flight this is  $1.075m$ . The distance between the outlet and the top surface of the stored material is approx  $30cm$ . The error in the middle of the silo is then calculated using a value of  $a = 0.15/1.075$ . This gives an error of  $\approx 3.9\%$ .

The effect of Coriolis forces will now be quantified. The Coriolis effect is the perceived deflection of a moving object when it is viewed from a rotating reference frame, and will be present whenever there is movement in any direction within the model. If an object moves within the model's reference frame with velocity  $v$  then the artificial

acceleration is of magnitude  $2v\omega$  where  $\omega$  is the angular velocity of the centrifuge arm. The ratio of Coriolis acceleration ( $2\omega$ ) to centrifugal acceleration is then:

$$\frac{\text{Coriolis acceleration}}{\text{Centrifugal acceleration}} = \frac{2\omega}{R\omega^2} = \frac{2 \times \text{velocity within model}}{\text{flight velocity of model}} \quad (2.51)$$

For example, if the silo centrifuge model is being tested at 10g then the flight velocity at the outlet is  $10.69\text{ m/s}$ . Material within the silo discharge at a maximum velocity of approximately  $0.21\text{ m/s}$  and therefore the error caused by the Coriolis effect is  $2 \times 0.21/10.69 = 3.9\%$ , which is considered small. Furthermore the model is arranged such that the Coriolis forces will act out of the plane about which the quasi-two-dimensional material is orientated.

In this research a “model normalisation” technique has been developed where the experimental results have been normalised with respect to gravity. This allows data from different centrifugal accelerations to be quantitatively compared without the need to develop a prototype or multiple models of different size. This is a new centrifugal modelling approach. Modelling of models is the more common technique and involves conducting tests at different centrifugal accelerations in order to observe the same behaviours when the product of length and acceleration are the same.

## 2.4 Silo centrifuge modelling

### 2.4.1 Background

Silo centrifuge modelling is a technique that requires few assumptions and promises quick and cheap series of tests. In practice however it is rarely used due to the high costs of investing in a centrifuge, the specialist expertise which must be developed, and the technical and physical requirements of instrumentation.

[Craig \[1989\]](#) reports that centrifugal modelling as an engineering tool was first suggested by Edouard Phillips in 1869. However, it was only in 1931 when centrifuge modelling was first used by Philip Bucky to model tunnels. His centrifugal techniques

proved useful and this is the first record of centrifuge modelling directly influencing the design of Geotechnical structures.

In the 1960s Peter Rowe and Andrew Schofield built centrifuges at the University of Manchester and UMIST (England). Their work, involving models up to 2.0 x 1.0 x 0.6 metres, showed that centrifuge model results can be used for fundamental research as well as project-specific design. Scaling laws and limitations were developed, and water retaining embankments were modelled. Centrifugal modelling developed to become a popular area of research in the 1980's and 1990's with many research centres investing in new centrifuges.

Geotechnical centrifuge modelling has focussed on embankments, slopes, foundations, and tunnels. Water-retaining embankments encompassing undisturbed clays and drainage controls have been modelled, as well as consultancy projects for off-shore oil and gas industries. These have included gravity platforms, drag anchor behaviour, and piled structures. 2 metre long pipelines have been modelled at over 100g. Silo centrifuge models have remained rare because of the unique challenges that these models present including model dimensions, instrumentation design and data collection.

Silo centrifuge research began in the middle of the 1970's and continued through the 1980s. After the 1980s silo centrifuge research became less frequent and almost no silo centrifuge has been published during the 1990s or 2000s.

The first studies to investigate silo design using a centrifuge were by [Molerus and Schoeneborn \[1977\]](#) who investigated critical outlet dimension by varying the apparent gravity. The critical outlet dimensions for mass and funnel flow were quantified and the silo centrifuge technique was found to give results in agreement with existing silo design theory. This showed that the centrifuge could be a legitimate tool in silo research. Critical outlet diameter was also investigated by [Egerer \[1982\]](#).

[Nielsen and Askegaard \[1977\]](#) investigated scaling errors and reported that both cohesive and non-cohesive material flows can be scaled using silo centrifuge models. They concluded that non-cohesive models had a minimum necessary size and recommended silo centrifuge models for investigations using cohesive media.

## 2. SILO AND HOPPER DESIGN

---

[Craig and Wright \[1981\]](#) investigated flow profiles and wall stresses using stroboscopes (lamps which are switched on and off at a precise frequency) to observe flow patterns. Funnel flow and mass flow were observed and wall pressures were found to give good agreement with Janssens equation.

[Nielsen \[1984\]](#) conducted a review of centrifuge testing as a tool in silo research and discussed experimental difficulties including sources of error.

[Kristiansen et al. \[1988\]](#) conducted a centrifuge study of load and flow conditions in silos with cohesive media and showed that hopper stresses are dependent on filling procedure, that under normal conditions where flow is stopped and restarted, the Jenike critical outflow diameter is too small.

Scaling errors were investigated by [Lepert et al. \[1989\]](#). Material substitution was found to result in uncontrolled errors and is therefore not recommended. Using the same material in the model and prototype was found to give good flow rate prediction. The interaction between geometry and flow regime was also investigated.

Work by [Grossstueck and Schwedes \[2005\]](#) is the only work on silo centrifuge modelling found after this. The work was first published in 2003. The critical outlet diameter for silos discharging cohesive media was investigated and silo centrifuge techniques were compared to theoretical approaches. They concluded that silo centrifuge modelling was suitable for cohesive media.

These silo centrifuge studies show a consistent observation of the usefulness of centrifuges in determining key elements of silo design. The effects of hopper inclination and outlet diameter have been repeatedly investigated. However the level of detail in the observations and conclusions is limited. This is probably due to the limited imaging and computing technology available in the past. Silo centrifuges modelling is particularly suited for use with cohesive materials because their strength is related to compaction. The use of silo centrifuge modelling for non-cohesive material is reliable but the advantages over other techniques are less pronounced. Measurement errors have been reported to increase with decreasing model size and increasing model stiffness, which places additional requirements on instrumentation design. Silo centrifuge modelling is a useful tool for project-specific silo design and investiga-

tion, but is not without its limitations. Since shearing mechanisms are discrete and do not scale as a continuum, particle size effects involving shear must be avoided. Therefore smooth-walled silos are preferable to rough-walled silos.

The accessibility and convenience of having small-scale, repeatable tests that are cheap is offset by the design considerations discussed in section [2.4.2](#).

### **2.4.2 Silo centrifuge model design**

- The ideal model set up requires a uniform increase of gravity across the entire model. However, centrifugal acceleration is dependent on the radius of rotation and a linear increase in gravity across the silo in the direction away from the rotational axis is created. Therefore the change in gravity across the model should be limited by reducing the height of the silo model, or having a large radius of rotation. Silos tend to be much taller than they are wide and even in the case of large centrifuges only very small silo centrifuge models have yet been produced.
- If one silo medium is to be substituted for another they must have the same constitutive properties, otherwise uncontrolled scale errors result. This is usually impossible and it is better to avoid situations where particle size becomes significant. Material substitution is only suitable in exceptional circumstances.
- Temperature deformations are magnified by the scaling effect in a similar way to geometric tolerances. Temperature should therefore be tightly controlled if the materials are sensitive to changes in ambient temperature.
- [Rotter \[2009\]](#) reports that the order of decrease in scale must be matched by the order of increase in dimensional tolerance. This is due to the influence of geometric imperfections on local pressures which influences the strain behaviour.
- [Nielsen \[1984\]](#) reports that if the silo is to be filled during centrifugal flight then Coriolis effects must be considered. If the material is known to discharge

differently after pluvial or spout filling then the effect of the Coriolis forces on grain direction should be investigated.

- [Nielsen \[1984\]](#) also reports that interruption to planar surfaces by instrumentation such as pressure sensors influence granular material flow. The contact area and contact stiffness of instrumentation including pressure sensors must be considered, and the critical dimensions of sensor surfaces will scale with the model.

### 2.5 Silo research

Silo and Hopper design is largely informed by the results of experimental work using models. There are relatively few theoretical solutions for silo problems and this is largely the result of two principal challenges - it is difficult to develop constitutive relations which remain valid during filling (consolidation) and discharge (with large deformation), and secondly, it is difficult to produce experimental results which can be used reliably when handling other bulk solids.

[Janssen \[1895\]](#), [Jenike \[1964\]](#) and [Walker \[1966\]](#) are the principle exceptions to this trend. Janssen calculated wall pressures in a silo with vertical sides and Jenike calculated the critical outlet diameter of a silo and developed design criterion for producing mass flow or funnel flow. Walker extended the work of Janssen to calculate hopper wall pressures. Their work is based on continuum models

Current challenges include the quantification of stresses during silo discharge, because the asymmetric variation of stresses produced in the structure during discharge are often more dangerous than symmetrical peak pressures [Rotter \[2009\]](#). Numerical methods such as the FEM and DEM do not adequately predict these discharge fluctuations and therefore better constitutive equations are required.

---

## 2.6 Discharge pressure theories for structural design

Work by [Arnold \[1980\]](#), [Jenike et al. \[1973\]](#), [Walker \[1966\]](#) and [Walters \[1973\]](#) shows that non-uniform vertical and wall shear stresses would result in smaller wall pressures. The Walker and the Walter methods require that the solid is in a fully plastic state at all times, whilst the Jenike method assumes that it is in an elastic state. These theories give revised quantities for the maximum possible pressures expected at a given height. Standard design practice requires that the entire failure envelope be considered, and for a period it was accepted that these maximum symmetrical loads should be considered. However, it is now clear that these theories do not adequately capture the real granular behaviour because silos do not frequently fail due to bursting, as these theories would predict.

The theory of [Jenike et al. \[1973\]](#) is the most widely accepted and forms the foundation of the Australian standard for pressures during discharge. [AS 3774 (1996)]. This has the effect of making Australian silos very strong as the ratio of discharge to filling pressures is high.

[Rotter \[1999\]](#) suggests that the instantaneous changes from filling to discharge pressures at the switch are responsible for much of the difficulty in switch theory. It is suggested that if a graduated change in pressures, based on values of  $K_0$  measured directly from experiments on test solids is used, then a graduated increases in symmetrical pressure peaks during discharge is predicted. This approach is used in the European design standard EN 1991-4 (2007) and prescribes much smaller  $C_e$  values than design standards based on older theories.

### 2.6.1 Influence of particle shape

Advances in technology have allowed new investigations into the influence of particle shape on three dimensional silo flow, discharge rate and wall stresses. Recent work by [Abbaspour-Fard \[2010\]](#) aimed to verify the importance of particle shape on granular material fabric and investigate if the increased computational expense was justified. Spherical particles and elongated particles with an aspect ratio ranging from 1 to 4

## 2. SILO AND HOPPER DESIGN

---

were compared. They reported that:

1. Density and coordination number are higher with spherical particles.
2. The flow patterns and mass discharge rate are significantly different with particles of aspect ratio 4 compared to 1. With the elongated particles, the material failed during discharge with propagating shear lines or cracks travelling up into the silo. As aspect ratios approached 1, these shear lines were not observed and discharge was steady from the layer closest to the bottom of the silo.
3. They concluded that particle shape should be taken into account as discharge rate and flow pattern could not be assumed to be the same across otherwise similar particles with different aspect ratios.

[Cleary \[2002\]](#) investigated the effect of particle shape in relation to the discharge rate from a hopper and found that elongated particles can produce flow up to 30% quicker with significantly different flow patterns. Angularity and coarseness of particles was also investigated and flow patterns were found to remain unchanged with flow rates decreased by up to 28% compared to spherical particles.

### 2.6.2 Design considerations

In a series of reports for industrial practitioners [Carson \[2001\]](#) reported that silos and hoppers fail due to a wide range of problems spanning design, construction and operation issues. The following recommendations are drawn from case studies:

1. Conditions which alter central filling or discharge such as feeder geometry, outlet locations or extraction method should be investigated before symmetrical geometry is assumed.
2. Flow pattern and material flow properties should be verified for each design case. If the predicted funnel flow is close to mass flow then both regimes should be considered.

3. The use of tabulated figures should be a last resort because of the complexity of granular materials. Tabulated figures cannot encompass all the factors that affect the flow properties of a granular material and therefore, additional safety factors should be used to account for unknown variables.

## **2.7 Numerical modelling using the Discrete Element Method (DEM)**

### **2.7.1 Introduction**

Numerical modelling is the computation of material stresses and strains based on mathematically defined constituent relationships and boundary conditions. Numerical modelling of granular materials may be split into two broad categories; techniques using continuum models and those using discrete models.

Continuum models were first developed for classical continuous materials and are used effectively in fluids mechanics and structural modelling applications. Continuum models are also suitable for geotechnical design applications with small deformations and large length and time scales. However continuum models of granular materials processes are more challenging. This is due to the difficulties that arise because of compaction and dilation, changes in density and porosity and the loss and gain of particle contacts. Continuum models of granular systems mainly use the Finite Element Method.

Discrete modelling techniques overcome several of the weaknesses of continuum modelling techniques, but are limited to small numbers of particles and simplified descriptions of particle shape and contact laws. The most widely used discrete modelling method is the Discrete Element Method (DEM).

The DEM was developed by [Cundall and Strack \[1979\]](#) and its great advantage is the simulation of individual particles and their interactions with each other and with boundaries. Particle interactions are computed by solving Newton's second law

## 2. SILO AND HOPPER DESIGN

---

for each particle and this allows complicated emergent behaviours to be modelled. Boundary conditions and material properties can be specified according to the contact models being used, and the model parameters are linked to material properties. However the disadvantages of DEM include the computational resources required to model systems with a similar number of particles to industrial systems. At present, DEM is limited to modelling at most 100,000 particles when using a normal PC.

Particle Flow Code (PFC) is a commercial DEM software developed by ITASCA. It has a minimal graphical user interface and models are built using the FISH programming language. In PFC, a DEM model is composed of many independent particles (balls), and surfaces (walls). The balls are rigid and the contacts between balls or ball and wall are characterized by the “soft contact approach” where a finite normal stiffness represents the stiffness at a contact. This allows the mechanical behaviour of the model to be described in terms of the movement of each individual particle and the inter-particle forces acting between them. The relationship between the motion of a particles and the forces acting on it is described by Newton’s laws of motion. More complex behaviours can be described using inter-particle bonds.

The effect of a wall on a particle is that of a velocity boundary condition and the equations of motion are not satisfied for walls. Wall movement is defined by the user and is not affected by the forces acting on them.

A DEM model makes the following assumptions:

1. The particles are rigid bodies.
2. The contacts occur over a vanishingly small area (i.e., at a point).
3. The contacts are modelled using a soft-contact approach where the rigid particles are allowed to overlap one another at contact points.
4. The magnitude of this overlap is proportional to the contact force via the force displacement law.
5. All overlaps are small in relation to particle sizes.
6. Bonds can exist at contacts between particles.

---

## 7. All particles are spherical <sup>1</sup>.

Particle interaction is a dynamic process with equilibrium being reached wherever the internal forces are balanced. The net contact forces and displacements are computed by tracing the movements of all the individual particles. These movements are the result of disturbances propagating through the system which are caused by body forces or particle motions. This process is dynamic and the propagation speed is a function of the physical properties of the system.

The dynamic behaviour is discretised by assuming that velocities and accelerations are constant within each time step. Additionally, the time step is chosen to be small enough so that a disturbance cannot propagate further than the region bounded by its nearest neighbours within one time step. This ensures that the forces on each particle are always determined only by its interactions with particles with which it is in contact with. This has the disadvantage that when modelling systems with a wide particle size distribution the time step is decreased to account for the smallest particle size.

### 2.7.2 DEM calculation cycle

In a DEM model two types of calculation are completed before each time step. These are the application of Newton's second law on each particle, and a force-displacement law on each contact. The force-displacement law updates the contact forces on each particle and Newton's second law is used to determine the motion of each particle. Walls only require the updating of force-displacement laws for each contact they have with balls, because wall velocity is controlled by the user. At the end of each time step the position of the wall is updated according to the specified velocity.

For each simulated time step, the order of calculations is:

1. Calculate the force acting on each particle

---

<sup>1</sup>At present, clumps of spherical particles may be arranged to form alternatively shaped particles that behave as one single particle. Non-spherical particles created by other methods are not yet available in commercially-available software

## 2. SILO AND HOPPER DESIGN

---

2. Calculate the position of each particle
3. Update the wall positions

At the beginning of each time step, the set of contacts is updated from the known particle and wall positions from the previous time step. Contacts are formed or broken automatically. The force-displacement law is then applied to each contact and the contact forces are updated. The contact forces are determined based on relative motion between the balls and walls in contact and the contact model being used.

Once the forces have been determined, the law of motion is applied in order to update the position and velocity of each particle, which are based on the forces and moments resulting from the contact and body forces acting on the particle. The wall positions are also updated based on their specified velocities.

### **2.7.3 Force-displacement law**

The force-displacement law relates the relative displacement between two entities (ball-ball or ball-wall) at a contact point to the contact force that acts on those entities. In DEM a contact is described as occurring at single point that lies on a plane described by a unit normal vector. The contact point is always within the interpenetration volume and for ball-ball contacts, the normal vector is directed along the line connecting the ball centres. For ball-wall contacts the normal vector joins the ball centre to the nearest point on the wall. The contact force between the two entities is split into its normal and shear components. The normal component acts in the direction of the normal vector and the shear component acts in the direction of the contact plane. These two force components are related to the relative displacement by the normal and shear stiffnesses at the contact and the force-displacement law.

#### **2.7.4 Law of motion**

The movement of a particle is determined by the resultant force and moment vectors acting upon it and is split up into translational and rotational parts. The translation of the particle is described by the resultant force, which contains terms including the position, velocity and acceleration of the particles centre of mass. The resultant moment of the particle is expressed by the rotational moment of the particle and is described in terms of its angular velocity and angular acceleration.

#### **2.7.5 Boundary conditions and initial conditions**

Forces are applied to the assembly through gravity and wall movements. Translational and rotational velocities can be specified for balls as well as walls but applied forces cannot be specified. Wall velocities are set by specifying the translational and rotational velocities, and the centre of rotation.

Unlike walls, applied forces and initial moments, velocities and rotations can be set for balls. These can be specified as initial values which will change according to the contact forces and law of motion, or can be kept constant until specific conditions are met.

#### **2.7.6 Determination of time-step**

In PFC the equations of motion are integrated using a centred finite-difference scheme:

These solutions remain stable only if the timestep is below a critical value, which is related to the Eigen period of the system. Eigenvalue analyses for large and constantly changing systems are impractical and therefore a simplified procedure is employed to conservatively estimate the critical timestep at the start of each calculation cycle. The actual timestep used will be smaller than this and can be set as a fraction of the critical time step.

## **2.8 Research summary tables**

Table 2.1: Silo flow

Application	Experimental methods or parameters	Materials	Key results	Reference
Augmenting silo design for improved flow profiles	Industrial hopper investigated using sugar cubes as tracers.	Sugar ingots	The flow profile was successfully investigated in poorly performing working silo using a tracer method.	<a href="#">Job et al. [2009]</a>
Investigation of influence of flow characteristics	Using the Discrete Element Method the effect of particle size and silo geometry on flow rate, porosity, interaction forces and coordination number were investigated.	Theoretical numerical	Silo geometry has a greater effect on silo flow than particle size distribution. Mixing is propitious to flow. With a given particle size distribution, the relationship between flow rate and orifice size is linear.	<a href="#">Wu et al. [2009]</a>
Preventing funnel flow. Silos with two outlets	Physical model and Distinct Element Analysis	3 uniform sands	Silos with multiple openings greatly reduce funnel flow effects and alter structural forces.	<a href="#">Cheng et al. [2010]</a>
Flow parameters in eccentric silo flow	Digital particle image velocimetry (DPIV), Velocity functions using the exponential function, multiple regression, and <i>ch</i> function were investigated	Flax seeds	Both the generalized Gauss type function and the <i>ch</i> function can decrypt velocities when dependent on two variables. 2 regressions were required to find this function	<a href="#">Sielamowicz and Czech [2010]</a>
Effect of filling method on silo flow and wall stresses	Flow pattern observed from top surface of a flat-bottomed silo. Wall stresses deduced from strain gauges.	Barley Plastic Pellets	Filling method has a significant effect on flow pattern of plastic pellets, but not on that of Barley.	<a href="#">Zhong et al. [2001]</a>

Table 2.2: Particle shape

Simulation	Method/Contact Laws	Key results	Reference
Influence of particle shape on granular beds	DEM (3D)	Elongated or blocky particles reduce flow rates and narrow the flow profile.	<a href="#">Abbaspour-Fard [2010]</a>
Influence of particle shape on hopper discharge	DEM (3D)	Elongated or blocky particles reduce flow rates and narrow the flow profile.	<a href="#">Cleary [2002]</a>

Table 2.3: Silo research

Application	Experimental methods or parameters	Materials	Key result	Reference
Design	Case studies	Various industrial materials	Accurate prediction of flow pattern is essential	<a href="#">Carson [2001]</a>
Wall stresses & loading conditions	Empirical	n.a.	Empirical procedure described	<a href="#">Carson and Jenkyn [1993]</a>
To document silo phenomena	Visual observation & pressure measurement	Barley	Packing method is necessary to model silo flow	<a href="#">Nielsen [1998]</a>
Pressure measurement in silos with eccentric hoppers	Full-scale physical model	Particles: Maize Silo: Steel	Wheat, Multiple phenomena observed, including pressure oscillations, flow regime shifts, patch loads, effect of geometry on loads	<a href="#">Ramirez et al. [2010]</a>

Table 2.4: Silo centrifuge research

Application	Experimental methods or parameters	Test material	Key result	Reference
Critical silo outlet diameter	Outlet opened and gravitational field increased until flow initiation. Material was pre-consolidated.	Barytes Powder, BaSO <sub>4</sub> 15 $\mu$ m	Funnel flow and mass flow can be observed. Intermittent flow at critical stress level.	<a href="#">Molerus and Schoeneborn [1977]</a>
Scaling errors in silo centrifuge models	Measured wall stresses and observed flow profiles. Filling, consolidation and discharge during rotation	Cohesionless silica sand 63 - 149 $\mu$ m	Stress measurements are scalable.	<a href="#">Nielsen and Askegaard [1977]</a>
Wall stresses and flow profiles in silo centrifuges	Consolidation and discharge during rotation. Filling during rotation or under natural gravity field	Cohesive and cohesionless sand	Stress levels show good agreement with Janssen equation. Funnel and mass flow observed.	<a href="#">Craig and Wright [1981]</a>
Critical silo outlet diameter	Filling outside centrifuge. Principal stresses inferred from density changes.	Barytes Powder (BaSO <sub>4</sub> ), Limestone (CaCO <sub>3</sub> )	Mass flow and funnel flow were observed. Critical outlet dimensions were investigated.	<a href="#">Egerer [1982]</a>
Critical silo outlet diameter	Pre-consolidation in centrifuge. Acceleration until flow initiation. Principal stresses inferred from density changes.	Silicon Carbide (SiC)	Discussion of possible sources of error, and measurement techniques.	<a href="#">Nielsen [1984]</a>
Wall stresses & critical silo outlet dimension	Filling with-in and with-out centrifuge, in direction of and against Coriolis forces.	Limestone, (CaCO <sub>3</sub> ) cohesive and free flowing.	Stresses in hopper depend on filling procedure. Flow rate is dependent on centrifugal forces. Critical outlet dimension is larger than that calculated by Jenike.	<a href="#">Kristiansen et al. [1988]</a>
Scaling errors	Filled under gravity. Settlement and discharge in centrifuge	Seeds	Inserts and hopper stresses investigated. Inserts can induce arching and alternating flow. Flow rate investigation requires identical particles.	<a href="#">Lepert et al. [1989]</a>
Critical silo outlet diameter.	Filled under gravity. Consolidation in centrifuge. Unhindered and controlled discharge	Limestone (CaCO <sub>3</sub> ).	Review and verification. Silo centrifuge technique is reliable if boundary conditions are correct and wall stresses verified.	<a href="#">Grossstueck and Schwedes [2005]</a>

## 2. SILO AND HOPPER DESIGN

---

## Chapter 3

# Loads on silos and hoppers according to BS EN 1991-4:2006

In this chapter a method of calculating loads on the silo centrifuge structure is presented. The pressures calculated will be compared to the pressures measured in silo centrifuge tests. Although the size of the silo centrifuge is much smaller than any silo the design standard was intended to be used for, the principles of centrifuge modelling (Section 2.3) show that when gravity is increased by the same factor as geometry is decreased then the same stresses are produced at both model and prototype scales.

In order to predict normal pressures on the hopper correctly, it is necessary to classify the hopper as shallow or steep. A steep hopper is one in which the solid slides down the inclined hopper wall when the silo is filled and the solid above the hopper causes it to be consolidated. The wall frictional shear stress or traction is then related to the normal pressure on the hopper by the wall friction coefficient. This is fully mobilized wall friction.

A shallow hopper is one in which the solid does not slide down the inclined hopper wall when the silo is filled because either the slope is too low or the friction too high. In this case the wall frictional shear stress or traction is not related to the normal pressure on the hopper by the wall friction coefficient, but by a lower value, which

depends on the hopper slope and the stress state in the solid. In this state wall friction is not fully mobilized.

The compressibility of the solid also plays a role in the distinction but it is less important. The boundary between steep and shallow hoppers is smooth, with the same pressures applied to a hopper that is at the boundary whether it is in either category (wall friction is just fully mobilized).

According to BS EN 1991-4:2006, the model silo is treated as in action class 1. The geometries of hopper that are covered by this standard include wedge shaped hoppers with vertical end walls.

When designing a structure it is important to consider the range of characteristic values which may occur for design parameters. However this is not necessary for research comparing experimental and analytical observations and therefore constant values for  $K$ ,  $\mu$  and  $\lambda$  are used.  $K$  is derived according to Rankine's earth pressure theory and is not based on the approximation of Jaky (1948).

## 3.1 General Rules

For each condition in a hopper, the mean vertical stress in the solid at a height  $x$  above the hopper apex is determined as:

$$P_v = \left( \frac{\gamma h_h}{n-1} \right) \left( \left( \frac{x}{h_h} \right) - \left( \frac{x}{h_h} \right)^n \right) + p_{vft} \left( \frac{x}{h_h} \right)^n \quad (3.1)$$

in which:

$$n = S (F \mu_{h,eff} \cot(\beta) + F) - 2 \quad (3.2)$$

- $S = 4$  for the slot outlet of the silo centrifuge model.
- $\gamma$  is the upper characteristic value of the unit weight of the solid.
- $h_h$  is the vertical height between the hopper apex and the transition.

- 
- $x$  is the vertical coordinate upwards from the hopper apex.
  - $\mu_{h,eff}$  is the effective or mobilized characteristic wall friction coefficient for the hopper.
  - $S$  is the hopper shape coefficient.
  - $F$  is the characteristic value of the hopper pressure ratio. It should take account of whether the hopper is steep or shallow, and also whether filling or discharge loads are being evaluated.
  - $\beta$  is the hopper apex half angle.
  - $p_{vft}$  is the mean vertical stress in the solid at the transition after filling.

### 3.1.1 Evaluation of the lateral pressure ratio $K$

When Janssen's theory for wall pressures in vertical silos was first developed, the lateral stress coefficient was evaluated using Rankine's limit states. However as silos walls are usually rigid,  $K_a$  underestimates the stress ratio. Instead, a  $K$  value between  $K_a$  and  $K_p$  should be calculated. This is denoted  $K_0$ . It is approximately 50% larger than  $K_a$ . This implies that the bulk solid is being stored in an elastic state and is not near a plastic limit.

$$K_a = \frac{1 - \sin(\theta_i)}{1 + \sin(\theta_i)} \quad (3.3)$$

where  $\theta_i$  is the angle of internal friction of the solid.

For the coarse sand (material M2)  $\phi = 34$  deg. Therefore

$$K_a = \frac{1 - \sin(34)}{1 + \sin(34)} = 0.283 \quad (3.4)$$

But

$$K_0 = 1 - \sin(\theta_i) = 0.441 \quad (3.5)$$

This form of the equation was introduced by Jaky (1948) and is the established method of safely approximating  $K_0$ . It is the lower characteristic value for lateral pressure ratio. According to BS EN 1991-4 (2007), the approximation of the lateral stress ratio for filling for design purposes is defined as the upper characteristic value for lateral pressure ratio.

$$K_f = 1.1K_0 = 1.1(1 - \sin(\theta)) = 0.485 \quad (3.6)$$

## 3.2 Wall pressures for flat-bottomed silo

According to section 5.1(2) of BS EN 1991-3:2006 the model silo is classed as having intermediate slenderness because its height to diameter ratio is between 1 and 2. Expected pressures would then be calculated based on section 5.3: "Squat and intermediate slenderness silos". This uses a different approach to calculate wall pressures and is not suitable. The silo will be treated as a slender silo and horizontal pressures in the vertical section will be calculated according to Janssen's silo wall pressure theory.

### 3.2.1 Horizontal and vertical pressures and wall frictional traction

The values of horizontal pressure  $p_h$  and wall friction  $p_{wf}$  and vertical pressure  $p_{vf}$  at any depth after filling and during storage should be determined as:

$$p_{hf}(z) = p_{ho}Y_j(z) \quad (3.7)$$

$$p_{wf}(z) = \mu p_{ho}Y_j(z) \quad (3.8)$$

$$p_{vf}(z) = \frac{p_{ho}}{K} Y_j(z) \quad (3.9)$$

---

in which:

$$p_{ho} = \gamma K z_0 = \gamma \frac{1}{\mu} \frac{A}{U} \quad (3.10)$$

$$z_0 = \frac{1}{K \mu} \frac{A}{U} \quad (3.11)$$

$$Y_J(z) = 1 - e^{-\frac{z}{z_0}} \quad (3.12)$$

where:

- $\gamma$  is the characteristic value of the unit weight.
- $\mu$  is the characteristic value of the wall friction coefficient for solid sliding on the vertical wall.
- $K$  is the characteristic value of the lateral pressure ratio.
- $z$  is the depth below the equivalent surface of the solid.
- $A$  is the cross-sectional area of the silo.
- $U$  is the internal perimeter of the plan cross-sectional area of the silo.

Expression 3.10 and expression 3.11 are evaluated as:

$$z_0 = 0.265m \quad (3.13)$$

$$p_{ho} = 58860N/m^2 = 58.86kPa \quad (3.14)$$

### 3.2.2 Pressures during discharge on vertical walls

The symmetrical wall discharge pressures  $p_{he}$  (horizontal wall pressure) and  $p_{we}$  (wall frictional traction) should be determined as:

$$p_{he} = C_h p_{hf} p_{we} = C_w p_{wf} \quad (3.15)$$

where  $C_h$  is the discharge factor for horizontal pressure and  $C_w$  is the discharge factor for wall frictional traction.

Section 5.2.2.1 (5) of BS EN 1991-4:2006 gives the most appropriate silo classification. The following expressions are used:

$$C_h = 1.15 + 1.5(1 + 0.4e/d_c)C_{op} \quad (3.16)$$

$$C_w = 1.4(1 + 0.4e/d_c) = 1.4 \quad (3.17)$$

$$e = \max(e_f, e_0) = 0 \quad (3.18)$$

where:

- $e_f$  is the maximum eccentricity of the surface pile during filling.
- $e_0$  is the eccentricity of the centre of the outlet.
- $c_{op}$  is the patch load solid reference factor for the solid (see table E.1 in the design standard for further details) and is 0.4 for sand.

According to section 5.2.2.2 (2) for silos in action class 1, the discharge patch loads may be ignored.

### 3.3 Silo with 30 degree hopper

A hopper is classed as steep if the following condition is met:

$$\tan(\beta) < \frac{1 - K}{2\mu_h} \quad (3.19)$$

---

where

- $K$  is the lower characteristic value of the lateral pressure ratio on the vertical walls.
- $\beta$  is the hopper half angle.
- $\mu_h$  is the lower characteristic value of wall friction coefficient in the hopper.

For sand against stainless steel a wall friction coefficient of 0.3 is used. This value is widely available in published data. For sand against the pressure sensor material the wall friction coefficient of 0.4 is estimated based on comparisons with other materials.

Expression 3.19 therefore becomes:

$$\tan(30) < \frac{1 - 0.441}{2 \times 0.4} \quad (3.20)$$

This is true, therefore the hopper is classified as steep.

### 3.3.1 Filling loads

Under filling conditions, the mean vertical stress  $P_v$  in the stored solid at any level in a steep hopper should be determined using expressions 3.1 and 3.2. The value of parameter  $F$  is  $F_f$ , with  $F_f$  as:

$$F_f = \frac{b}{1 + \frac{\tan \beta}{\mu_h}} \quad (3.21)$$

The parameter  $n$  (Expression 3.2) is then given by

$$n = S(1 - b)\mu_h \cot \beta \quad (3.22)$$

where  $b$  is an empirical coefficient  $b = 0.2$ .

The normal pressure  $p_{nf}$  and the frictional traction  $p_{tf}$  at any point on the wall of a steep hopper after filling should be determined as:

$$p_{nf} = F_f p_v \quad (3.23)$$

$$p_{tf} = \mu_h F_f p_v \quad (3.24)$$

In the case of model silo with 30 degree hopper, expressions 3.21 and 3.22 give the following values:

$$F_f = \frac{b}{1 + \frac{\tan \beta}{\mu_h}} = 0.0819 \quad (3.25)$$

$$n = S(1 - b)\mu_h \cot \beta = 2.8494 \quad (3.26)$$

### 3.3.2 Discharge loads

Under discharge conditions, the mean vertical stress in the stored solid at any level in a steep hopper should be determined using expressions 3.1 and 3.2 with the value of parameter  $F$  given by  $F = F_e$ .

The value of  $F_e$  may be calculated either by using the reference method given in expression 3.27 below, or by the alternative method given in section G.10 of the design standard.

$$F_e = \frac{1 + \sin \theta \cos \epsilon}{1 - \sin \theta \cos(2\beta + \epsilon)} \quad (3.27)$$

In which:

$$\epsilon = \theta_{wh} + \sin^{-1} \frac{\sin \theta_{wh}}{\sin \theta_i} \quad (3.28)$$

---


$$\theta_{wh} = \tan^{-1} \mu_h \quad (3.29)$$

Where:

- $\mu_h$  is the lower characteristic value of wall friction coefficient of the hopper.
- $\theta_i$  is the angle of internal friction of the solid.

### 3.3.2.1 Notes from BS EN 1991-4:2006

1.  $\theta_{wh} < \theta_i$  always, since the material will rupture internally if slip at the wall contact demands a greater shear stress that the internal friction can sustain.
2. Expression 3.27 is based on Walker's theory for discharge pressures. The alternative expression of Enstad for  $F_e$  may alternatively be used.

The normal pressure  $p_{ne}$  and frictional traction  $p_{te}$  at any point on the wall of a steep hopper during discharge should be determined as:

$$p_{ne} = F_e p_v \quad (3.30)$$

$$p_{te} = \mu_h F_e p_v \quad (3.31)$$

Where  $F_e$  is obtained according to expression 3.27.

Expressions 3.27 to 3.29 evaluate as:

$$F_e = \frac{1 + \sin \theta_i \cos \epsilon}{1 - \sin \theta_i \cos(2\beta + \epsilon)} = 1.0289 \quad (3.32)$$

$$\epsilon = \theta_{wh} + \sin^{-1} \frac{\sin \theta_{wh}}{\sin \theta_i} = 25.6603 \quad (3.33)$$

$$\theta_{wh} = \tan^{-1} \mu_h = 9.146 \quad (3.34)$$

### 3.4 Silo with 60 degree hopper

A hopper is steep according to expression 3.19.

This evaluates as:

$$\tan(60) < \frac{1 - 0.441}{2 \times 0.4} \Rightarrow 1.732 < 0.6988 \quad (3.35)$$

This is not true, therefore the hopper is shallow.

#### 3.4.1 Hopper wall friction coefficient in a shallow hopper

In a shallow hopper the wall friction is not fully mobilised. The effective wall friction is determined as:

$$\mu_{h,eff} = \frac{1 - K}{2 \tan \beta} \quad (3.36)$$

where:

- $K$  is the lower characteristic value of lateral pressure ratio for the vertical section.
- $\beta$  is the hopper apex half angle.

Expression 3.36 is evaluated as 0.161.

#### 3.4.2 Filling loads

Under filling conditions the mean vertical stress in the stored solid at any level of a shallow hopper should be determined using expressions 3.1 and 3.2. The value of

---

parameter  $F$  is given by:

$$F_f = 1 - (b / (1 + \tan(\beta) / \mu_{h,eff})) \quad (3.37)$$

The parameter  $n$  in expression 3.2 is then given as

$$n = S(1 - b)\mu_{h,eff}\cot\beta \quad (3.38)$$

where:

- $\mu_{h,eff}$  is the mobilised wall friction coefficient in the shallow hopper (see expression 3.36).
- $b$  is an empirical coefficient:  $b = 0.2$ .

The normal pressure  $p_{nf}$  and frictional traction  $p_{tf}$  at any point on the wall of a shallow hopper after filling should be determined as:

$$p_{nf} = F_f p_v \quad (3.39)$$

$$p_{tf} = \mu_{h,eff} F_f p_v \quad (3.40)$$

where

- $F_f$  is as in expression 3.37.
- $p_v$  is as in expression 3.1.

Expressions 3.37 and 3.38 evaluate as

$$F_f = 0.9830 \quad (3.41)$$

$$n = 0.2982 \quad (3.42)$$

### **3.4.3 Discharge loads**

In shallow hoppers under discharge conditions the normal pressure and frictional traction may be taken as identical to the values on filling (Section 6.4.3 (1)).

# Chapter 4

## Silo centrifuge model description

### 4.1 Introduction

This chapter begins by describing the experimental set-up and then details the instrumentation and analysis techniques. The granular materials used in the investigation are detailed next and the test procedure is explained.

A quasi-two-dimensional planar silo model was designed and built for the geotechnical centrifuge at the BOKU, Vienna. Four materials were investigated using two silo geometries. Load cells measured the mass of material as it discharged from the silo and high-speed video captured the flow of material behind the front transparent wall. A Particle Image Velocimetry analysis was conducted on the frames from the video to quantify the flow behaviour.

### 4.2 Stress equivalence between scales

When gravity is increased by the same factor as that by which model geometry is decreased, the same stresses and strains will be produced in the same relative locations in the model as in the prototype. It is demonstrated here using Janssen's theory of vertical silo wall pressures (see Section [2.1.7.1](#)), which states that pressures

#### 4. SILO CENTRIFUGE MODEL DESCRIPTION

---

normal to a vertical silo wall may be calculated as:

$$q_{\text{prototype}} = \frac{1}{\mu K} \frac{A}{U} \rho_b g \left( 1 - e^{-z / \frac{1}{\mu K} \frac{A}{U}} \right) \quad (4.1)$$

If a model-scale silo is built such that the length scale is reduced by a factor of  $N$  and gravity is increased by a factor of  $N$  then equation 4.1 leads to:

$$q_{\text{model}} = \frac{1}{\mu K} \frac{A}{N^2} \frac{N}{U} \rho_b N g \left( 1 - e^{-z / \frac{1}{\mu K} \frac{A}{N^2} \frac{N}{U}} \right) \quad (4.2)$$

$$= \frac{1}{\mu K} \frac{A}{U} \rho_b g \left( 1 - e^{-z / \frac{1}{\mu K} \frac{A}{U}} \right) = q_{\text{prototype}} \quad (4.3)$$

In Equation 4.2 the  $N$  terms cancel out and the equation becomes the same as Equation 4.1. The properties of the material remain the same at different scales because they are independent of both the silo geometry and gravity. This shows that equivalent stress states are produced in a prototype and in a model, and that a model of models technique is possible.

### 4.3 Development of a scaling law for time in silo centrifuge models

Let  $N$  be the ratio of centrifugal acceleration in the model to acceleration due to gravity on the surface of the Earth:

$$N = \frac{g^*}{9.81 \text{ m/s}^2} \quad (4.4)$$

The increase in mass discharge rate between two otherwise identical silos at different gravities is calculated by considering the Beverloo correlation for silo discharge rate. Equation 4.6 is introduced in Section 2.2.1 and  $g_1$  and  $g_2$  refer to two arbitrary

---

gravitational accelerations:

$$W = C\rho_b\sqrt{g}(D - kd)^{\frac{5}{2}} \quad (4.5)$$

$$\frac{W_1}{W_2} = \sqrt{\frac{g_1}{g_2}} \quad (4.6)$$

The ratio of discharge time between silo centrifuge tests at different gravities can then be expressed by considering that the mass of discharging material is kept constant:

$$W_1 = \frac{m}{t_1}, W_2 = \frac{m}{t_2} \implies \frac{W_1}{W_2} = \frac{t_2}{t_1} \implies t_2 = t_1\sqrt{\frac{g_1}{g_2}} \quad (4.7)$$

If  $g_1 = 9.81 \text{ m/s}^2$  then it corresponds to prototype scale and  $g_2/g_1$  may be expressed as  $N$ . This allows equation 4.7 to be expressed in conventional notation as:

$$t_N = \frac{t_P}{\sqrt{N}} \quad (4.8)$$

This scaling law is investigated and shown to be true in section 5.5.

## 4.4 Experimental set-up

### 4.4.1 Description of the IGT Beam centrifuge

All silo centrifuge tests took place in the beam centrifuge at the IGT, Universität für Bodenkultur BOKU (University of Natural Resources and Applied Sciences), Vienna. The model was designed and built for these experiments and where possible it has been considered how to make the model useful for future research also.

The geotechnical centrifuge is the only existing centrifuge in Austria. It was manufactured by Trio-tech, California in 1989. Since its installation it has been used for many geotechnical investigations including earth pressure, slope stability and foundation problems, however it had not been used to investigate silos.

Apart from one exception (Idinger [2010]) the centrifuge had rarely been used for

#### 4. SILO CENTRIFUGE MODEL DESCRIPTION

---

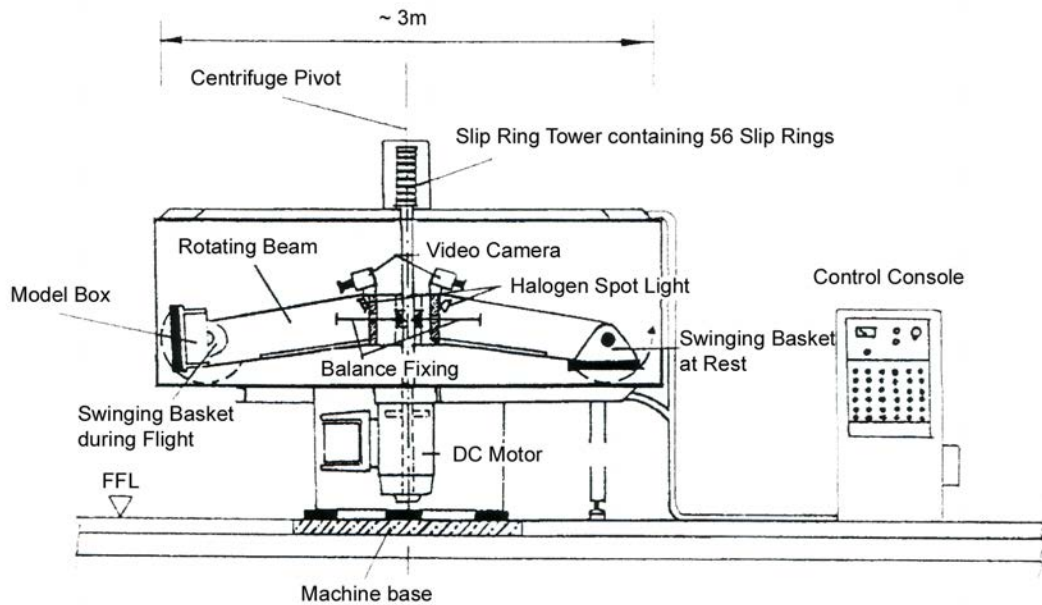


Figure 4.1: Schematic sketch of Trio-Tech 1231 Geotechnical Centrifuge, [Ferstl \[1998\]](#)

several years before this research and there was consequently a lack of modern equipment and expertise to use when designing and operating the model.

The beam centrifuge is “Model 1231 Standard Heavy Duty”. Table 4.1 lists its specifications. During flight, the motor forces the rotation of a symmetrical aluminium beam. A swing basket is hung at each end of the beam, the experimental model is placed into one swing basket and the counterweight is placed into the other. The counterweight must be of an equal mass to the experimental model to ensure that the beam remains balanced during flight. The counterweights used are small iron rods of individual mass  $\sim 14.5$  grammes placed into an aluminium box.

The slip-ring tower sits above the centrifuge and contains 56 electrical slip rings which transmit data and electricity between the centrifuge and the control room. The power supply includes low current and voltage slip rings which in the past have been used for lighting. The slip rings have capacities of 5 AMPS, 12 Volts and 5 AMPS, 24 Volts. The data is transmitted using DB15 plugs at either end.

A DB15 plug bar is used to transfer data and electricity between the centrifuge and

---

Table 4.1: Technical specifications of IGT Beam Centrifuge (TRIO-TECH, 1988)

Property	Value
Diameter of centrifuge [m]	3.0
Radius of swinging basket axis [m]	1.085
Motor	15HP DC
Slip rings	56
Radial acceleration [g]	0 to 200
Rotations per minute [1/min]	0 to 400
Maximum load capacity [G-kg]	10,000
Maximum model mass [kg]	90
Maximum model dimensions WxDxH [mm]	540 x 560 x 560
Total weight [kg]	2041

the control room. Plugs 1-5 are full bridge and plugs 6-10 are half bridge. Plugs 11-15 supply power and Plug 16 transmits an analogue camera signal. A slip ring full bridge contains 4 wires and a half bridge contains 3 wires. Power supply bridges contain 2 wires. An identical plug bar is installed in the control room.

The risks of injury when using the centrifuge are reduced by placing the centrifuge below ground level and requiring that nobody is in the same room as the centrifuge whilst it is in use. Also, the centrifuge is contained within a metal shell to add protection in case a component or test specimen becomes loose during flight. If the centrifuge becomes unbalanced during flight there is an automatic reset switch which cuts the power and activates the brakes.

The whole experiment is controlled from the centrifuge control room where the centrifuge is piloted using a control console. The required centrifugal acceleration is obtained by specifying the angular rotation either manually or using a computer programme. The current value is shown on a digital display. The velocity is held at a constant level with a stability of  $\pm 0.1\%$ .

## 4. SILO CENTRIFUGE MODEL DESCRIPTION

---



Figure 4.2: General view of geotechnical centrifuge

### 4.4.2 Design of the model

The silo centrifuge model was purpose-built for this research. In order to expedite the design and construction of the model the lighting and camera clamp from a previous investigation were used and modified (Idinger [2010]). Every other part of the model was custom designed and built for this investigation.

The silo centrifuge model is designed to behave as a quasi-two-dimensional silo and has dimensions  $15\text{cm} \times 10\text{cm} \times 29\text{cm}$  (width, depth, height). It is filled at  $1g$  whilst the centrifuge is stationary and the centrifuge is accelerated after filling is complete. The highest acceleration at which tests were conducted corresponded to  $60g$ . Technical drawings showing the design of the model silo are in Appendix A. Figures 4.2 - 4.7 show key features of the model.

The location of the outlet  $210\text{mm}$  above the base plate was chosen as the lowest possible height where the silo could be expected to discharge completely for a range of granular materials likely to be tested. This is only defined approximately because different materials have different angles of repose and the angle of repose was ob-

---

served during tests to decrease with increasing gravity<sup>1</sup>. The height of the top of the silo was simply the maximum possible that would fit in the centrifuge.

The model silo can be configured with a distance between the front and back walls (thickness) of either *1cm*, *3cm*, *5cm*, *10cm* or *15cm*. A thickness of *15cm* will make it a square silo. During this research a model thickness of *10cm* was used.

The silo centrifuge model can accommodate a hopper of any angle and the outlet does not need to be central. This flexibility was included in case the model is used in future research. The hopper pieces available during this research were for half angles of 60 and 30 degrees and for a flat-bottomed silo.

The interior of the model silo is completely smooth, there are no screw holes or protrusions in the walls. The only interruptions to planar aluminium or acrylic walls are the flush joints of neighbouring metal pieces positioned next to each other.

The discharge rate is measured using load cells beneath the collection bucket. Flow behind the front acrylic wall is observed using a high-speed video camera and lighting set-up.

A servo motor is used to initiate silo discharge. It opens the silo by pulling a pin which releases a spring loaded sliding door (Figure 4.8). The high-speed video camera is operated manually and is started before the centrifuge test begins. The load cell readings are monitored and recorded from the control room by connecting the load cells to an HBM spider8 Data Logger via the slip rings. The data logger is controlled using the HBM software CATMAN which runs on a PC in the control room. The data from the load cells is logged and displayed during a test and then exported as an Excel file. (Figure 4.23(a)).

---

<sup>1</sup>This influence of gravity on static angle of repose has also been observed by [Kleinhans et al. \[2011\]](#) and [Dorbolo et al. \[2013\]](#)

#### 4. SILO CENTRIFUGE MODEL DESCRIPTION

---

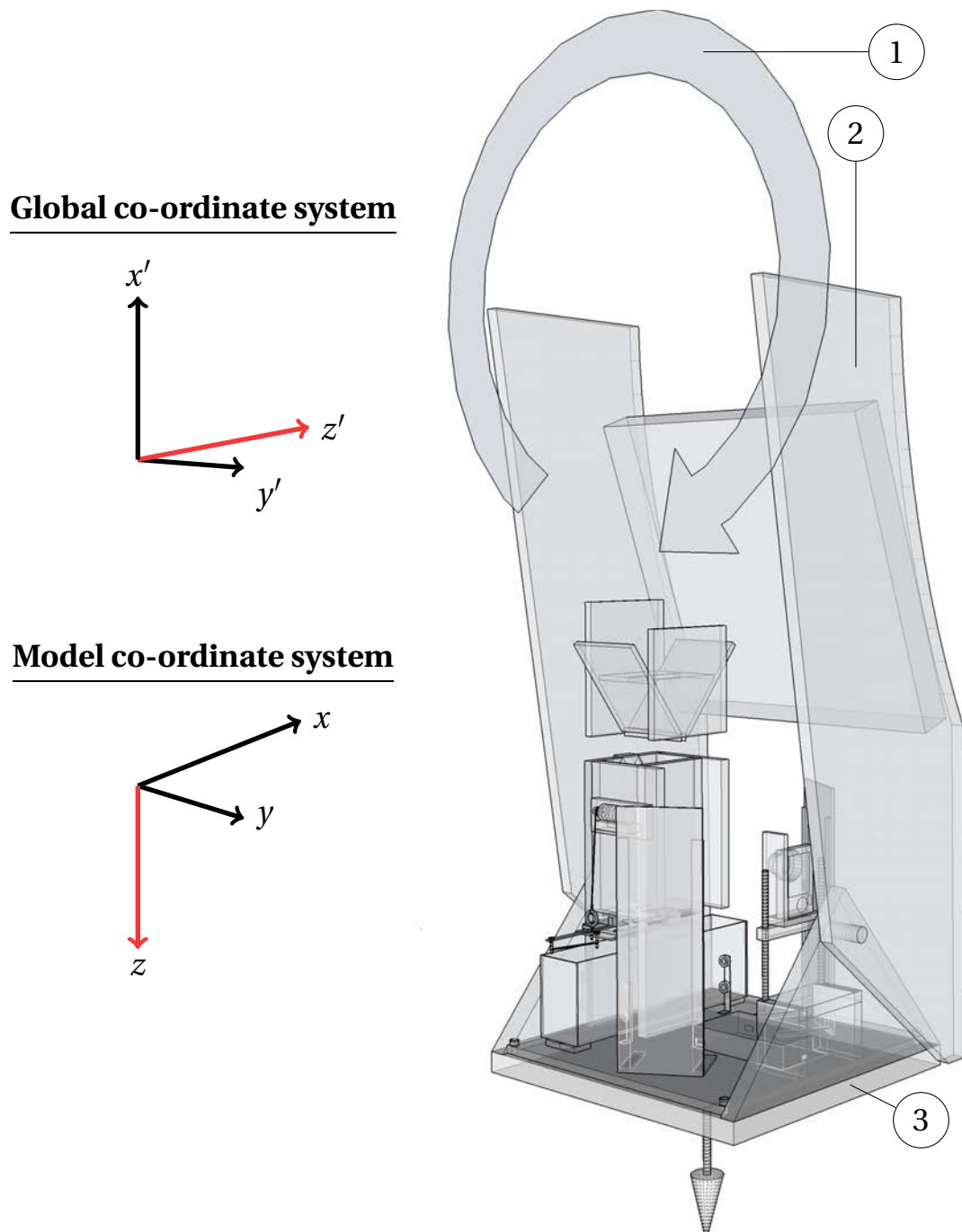


Figure 4.3: Sketch of model silo in centrifuge during flight. 1-direction of horizontal rotation, 2-centrifuge beam, 3-swing basket during flight



Figure 4.4: 3D sketch representing silo model before filling, before centrifuge flight, and during flight

#### 4. SILO CENTRIFUGE MODEL DESCRIPTION

---

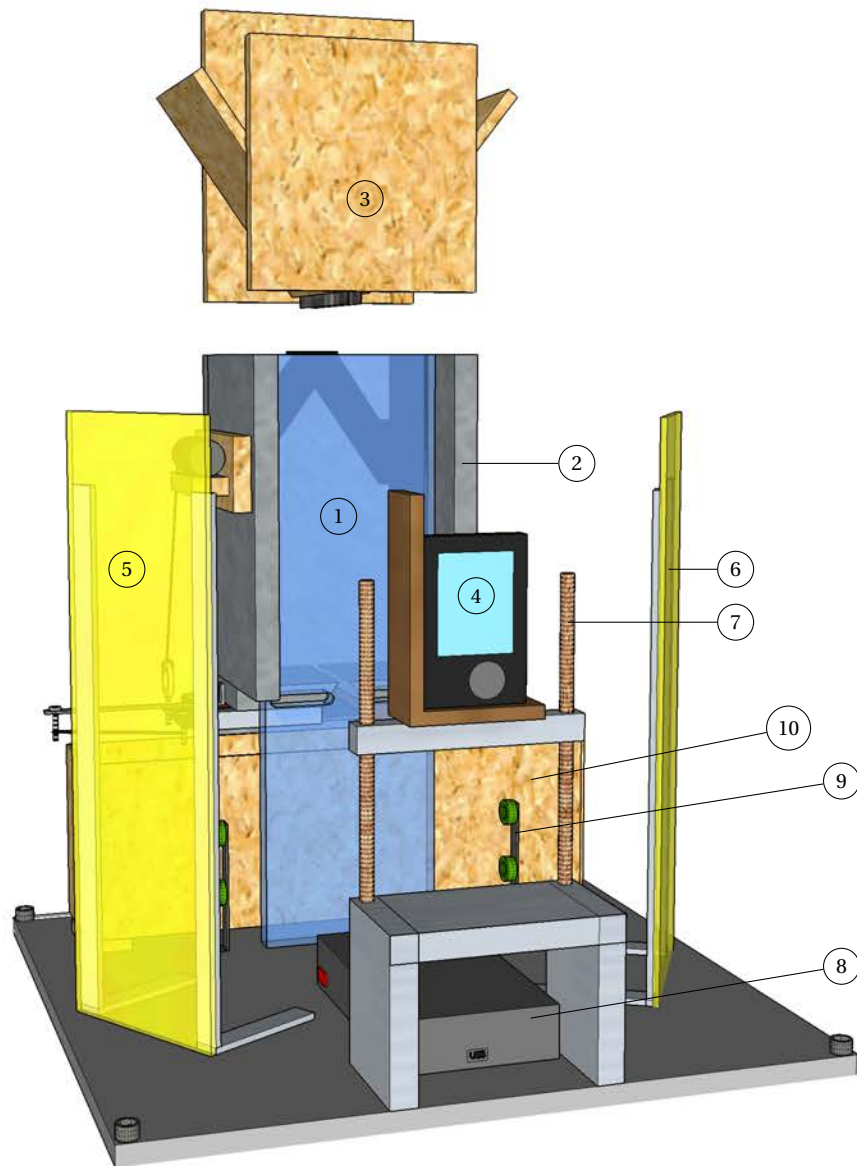


Figure 4.5: Sketch of model silo outside of centrifuge, 1-acrylic window, 2-side wall, 3-filling funnel, 4-camera, 5,6-LED array, 7-camera stand, 8-data logger, 9-vertical roller, 10-collection bucket

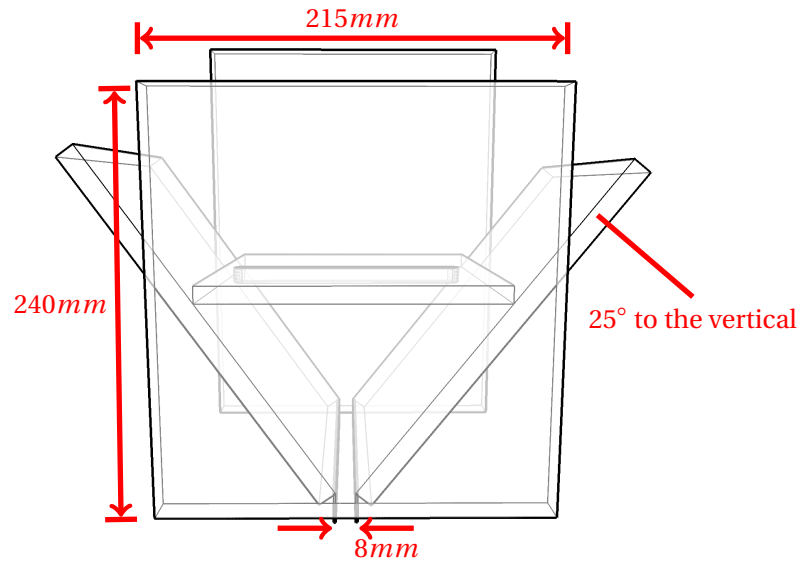


Figure 4.6: Funnel used to fill silo

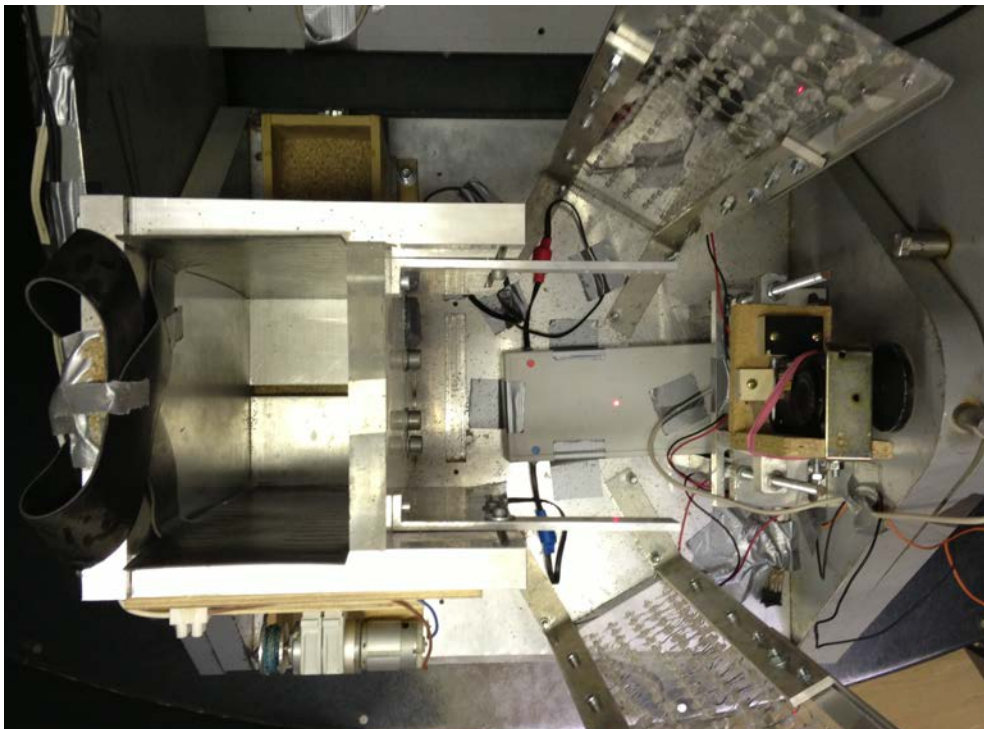


Figure 4.7: Top view of empty model silo showing pressure pads, data logger and high-speed camera

#### 4. SILO CENTRIFUGE MODEL DESCRIPTION

---

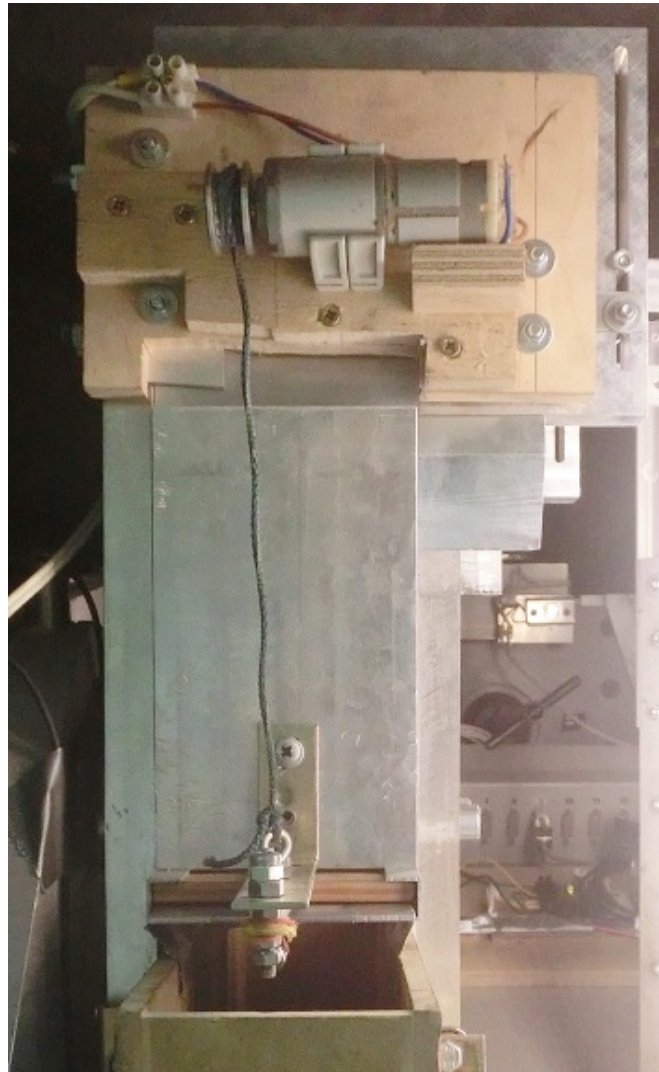


Figure 4.8: Side view of opening mechanism

---

## 4.5 Instrumentation

In this section, the instrumentation and the data analysis methodology is described. An overview of PIV is given in order to show the strengths and limitations of the technique.

### 4.5.1 High-speed video

High-speed video captures material movement behind the front Plexiglas wall during discharge. Video is recorded at 232 FPS with a resolution of  $512 \times 384$  pixels. Particle Image Velocimetry and image analysis techniques are applied to the frames to investigate flow. Figure 4.5.1 shows examples of the high-speed video captured during discharge of the silo centrifuge model.

A lighting system was custom-made for the experiments. It includes two LED arrays positioned either side of the video camera. Each array contains a grid of  $5 \times 22$  LEDs. This arrangement produces enough light to evenly illuminate the whole silo and does not create shadows or reflections which would interfere with the PIV analysis.

The frame rate of the video is verified by placing a stop watch in the frame. Any deviation from the normal frame rate of 232 FPS can then be accounted for and corrected. The frame rate quoted by the manufacturer is 240 FPS. The revised value was arrived at by repeatedly measuring the number of frames recorded over an interval ranging from 1 second to 3 seconds as recorded by the stop watch in the frame.

The output from the video frames is naturally in pixels, this is converted to absolute measurements by marking a grid onto the acrylic which contains points at a known distance from each other. Four points were marked onto the acrylic to make a rectangle of dimensions  $120\text{mm} \times 160\text{mm}$ . These points can be seen in Figure 4.9 as the black dots in white circles. (The bottom right point is behind the stopwatch and an additional point can be seen above the top brackets).

#### 4. SILO CENTRIFUGE MODEL DESCRIPTION

---



Figure 4.9: Photograph of model silo showing stopwatch and grid points

---

(a) M2 (Coarse sand), 5g

(b) M2 (Coarse sand), 15g

(c) M3 (Glass beads), 5g

(d) M3 (Glass beads), 15g

Figure 4.10: High-speed video example of silo discharge, 11.5x slower (20 FPS, original = 232 FPS), click to play

### 4.5.2 Particle Image Velocimetry

Particle Image Velocimetry is a technique for measuring the movement of solids or fluids. In this research, the open-source PIV software PIVLab (v.1.32) was used. [Tejchman \[2013\]](#) reports that that PIV is a cheap and effective optical technique for measuring surface displacements. Figure 4.5.2 shows example PIV analyses of the silo centrifuge model during discharge.

Particle Image Velocimetry was first developed to measure planar displacements and velocimetry in experimental fluid mechanics and has recently been used to measure displacements in fields other than fluid mechanics. This development has been accelerated by the rapid improvement of digital imaging technology; sensor resolution and sensitivity has increased, size, weight and cost have decreased, and even compact consumer cameras now come with limited high-speed video functionality.

PIV is useful in granular materials research because it allows observation of displacements and strain fields on the scale of grains over large areas (many grains) without disturbing the material. Key aspects of the technique are:

- **Non-intrusive velocity measurement:** PIV is an optical technique that compares sequential images of the subject material. In contrast to other measurement techniques, PIV investigations do not require that the material be disturbed by sampling or probing techniques.

If either the lighting or the spatial or temporal resolution of the imaging technique is limited then the quality of the results may be improved by using markers to increase either luminosity or contrast in the images.

- **Direct velocity measurement:** Individual particles or groups of particles may be tracked when using PIV to observe granular flow fields.
- **Spatial resolution / Whole field measurement:** PIV quantifies flow by analysing images of a flowing material. The quantification of velocity across most of the image is usually possible and therefore flow can be quantified at many locations. This contrasts with other measurement techniques that quantify flow

---

only at a single location. The spatial resolution of measurements made using PIV is therefore much higher than can be obtained with alternative methods.

The resolution of the imaging sensor will determine the maximum number of velocity vectors and thus the maximum spatial resolution of the results. If the resolution is too low or the area of interest too large, then the velocity gradients will not be tracked in sufficient detail and will be blurred which decreases the accuracy of the results.

- **Temporal resolution:** The frame rate and the exposure time both effect the temporal resolution of the analysis. As with traditional forms of photography, if movement is to be captured without blurring the image then a short shutter time must be used. Decreasing shutter time will require increasing the illumination. Also, the interval between frames needs to be significantly shorter than the duration of fluctuations or movements in the flow being observed.

#### 4. SILO CENTRIFUGE MODEL DESCRIPTION

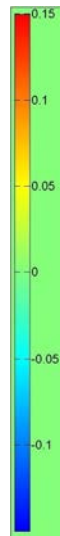
---



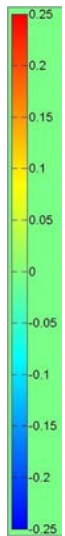
(a) M3 (Glass beads), 5g, Vertical component



(c) M3 (Glass beads), 15g, Vertical component



(e) M3 (Glass beads), 5g, Horizontal component



(g) M3 (Glass beads), 15g, Horizontal component

Figure 4.11: Example of PIV analysis of discharge from silo with flat-bottom, 19x slower (12 FPS, original = 232 FPS) click to play [m/s]

##### 4.5.2.1 Calculation of velocity vectors using PIV

Each image is divided into a large number of square regions. Each region covers a small number of grains with a unique combination of color or gray-scale values. Let one of these regions in image  $M_n$  be located at coordinates  $(u_1, v_1)$ . After some

time, the region has moved to a new location in image  $M_{n+1}$ . A search is conducted within a specified distance of  $(u_1, v_1)$  in image  $M_{n+1}$  and the correlation between the pixels at each search region and the original region is computed. Calculating the correlation value at each position results in a correlation function over the search area.

The location at which the highest correlation is found gives the new location of the region, and the vector joining the two locations is then calculated.  $(u_1, v_1)_{t_1} \rightarrow (u_2, v_2)_{t_2}$ . This process can be improved by requiring that the interpolation peak is significantly greater than the distortion of the correlation plane caused by signal noise. Sub-pixel accuracy can be attained by interpolating the correlation function around the peak. This process is repeated over the entire image to produce the vector field for an image pair.

PIV works well as long as the material has sufficient texture to generate unique interrogation areas. Sand is suitable because different grains have different shapes and colors which makes each interrogation area unique.

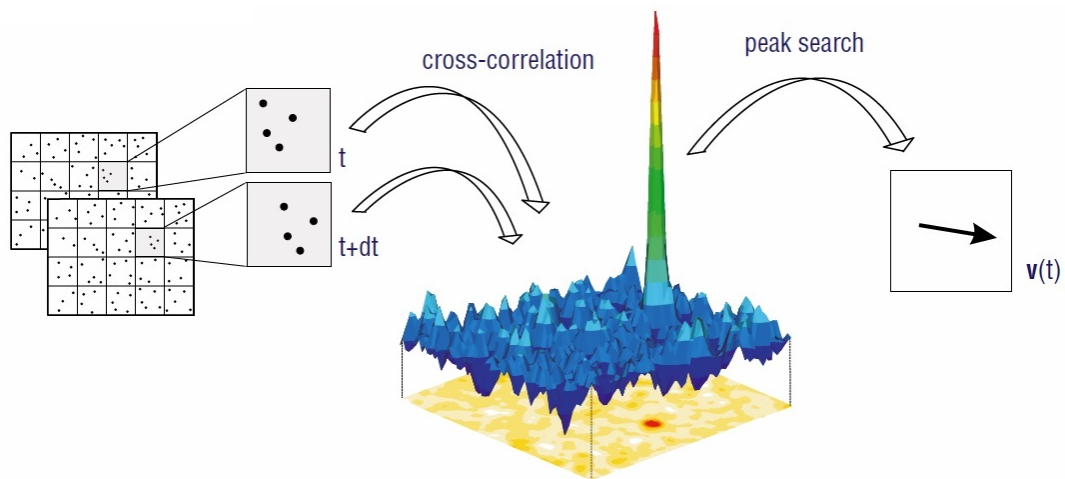


Figure 4.12: Description of PIV vector calculation

#### 4. SILO CENTRIFUGE MODEL DESCRIPTION

---

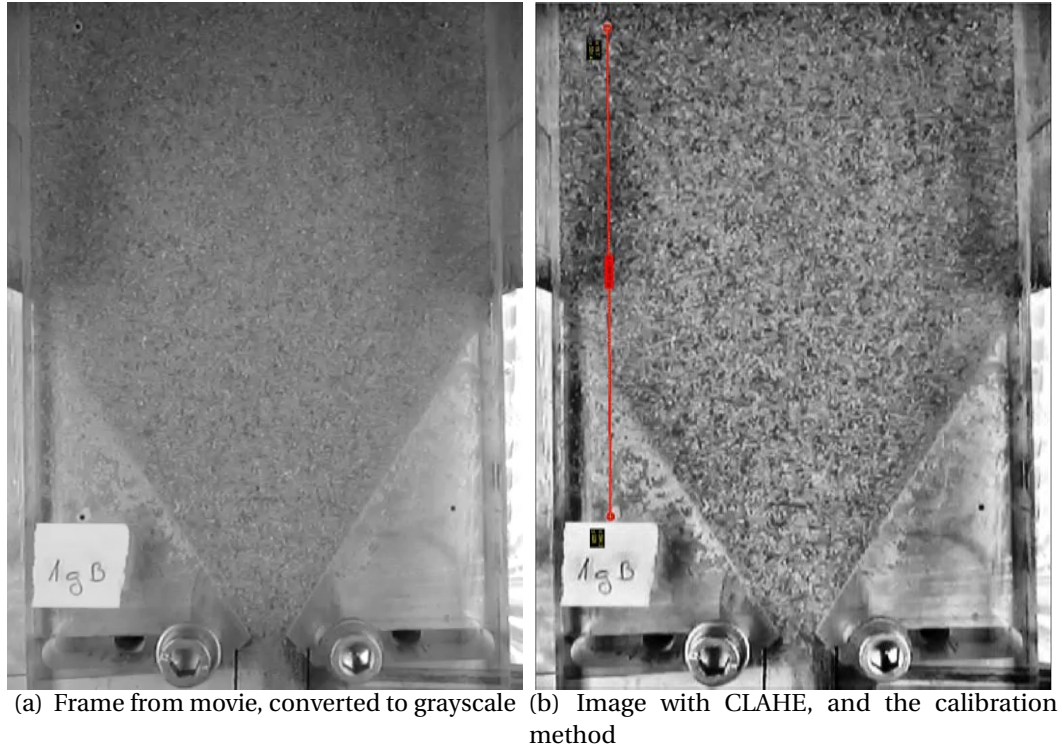


Figure 4.13: Image preparation

##### 4.5.2.2 PIVLab - an open-source Particle Image Velocimetry tool

PIVLab (v.1.32) was used for this research. It is open-source and runs from the MATLAB command line. The settings and parameters used in the analysis are now described:

- **Regions of interest and masks:** The region of interest remains constant throughout the analysis and cannot change between frames. It marks the region of the frames within which vectors will be computed.

Masks are areas of the region of interest which are not analysed. Masks are useful because the region of interest has to be rectangular but frequently flow boundaries such as the silo hopper are not rectangular.

- **Image preparation:** The video frames are enhanced using Contrast Limited Adaptive Histogram Equalisation (CLAHE). This technique increases the con-

---

trast of an image by making full use of the available range of brightness values (0 - 255) which increases the texture in the image. The effect of this enhancement is shown in Figure 4.13(b).

- **Fast Fourier Transform window deformation:** Velocity vectors are calculated using image processing algorithms. The algorithm used in PIVlab is the cross-correlation through Fast Fourier Transform (FFT) technique with linear window deformation interpolator.
- **Vector validation:** In images with poor quality it is possible for false (wild) vectors to be computed. These vectors will be dissimilar to their neighbours and can be removed using statistical techniques to identify outliers. In this research a conservative vector validation technique is used where only vectors that vary more than 7 standard deviations from the average are replaced with interpolated vectors.
- **Calibration:** The length unit of the vectors is converted from pixels to metres by specifying two points in the image which are a known distance from each other. This is shown in Figure 4.13(b). By specifying the separation of the points in metres a conversion from pixels to metres is possible. The time between frames is calculated outside of PIVLab and is manually input. The frame rate of the video was verified by using a stopwatch in the video frame.

### 4.5.3 Load cells

Load cells beneath the collection bucket record the load from the bucket and its contents. This is used to calculate the mass discharge rate from the silo during discharge. The collection bucket collects the granular material beneath the silo. Two miniature load cells are used, each has a rated capacity of  $1\text{ kN}$ . The collection bucket is kept in place by guide rails designed to apply only horizontal forces to the collection bucket. This ensures that vertical load is only transmitted through the load cells.

Two C9B  $1\text{ kN}$  miniature load cells from Hottinger Baldwin Messtechnik (HBM) are

#### 4. SILO CENTRIFUGE MODEL DESCRIPTION

---

used. They each have a diameter of  $26\text{mm}$ , a height of  $13\text{mm}$  and weigh  $65\text{ grammes}$ . Their sensitivity error is rated as  $< 1\%$ . The technical data sheet is included as Appendix C. The CATMAN data-logging software from HBM is used. This software contains a database of calibration data for the company's sensors including the C9b  $1\text{kN}$  miniature load cells. Output using the supplied calibration data is checked (Table 4.2) and the average error is a  $0.441\%$  larger force reported compared to the force applied. This error is smaller than the sensitivity error of the load cells and test results are not adjusted to consider it.

The accuracy is quantified by applying a range of forces and quantifying the error between input and output.  $3.3\text{kg}$  of coarse sand (material M1) is placed into the collection bucket so that the combined mass of the sand and the bucket is  $5.00\text{kg}$ . The sand is moved so that it had a constant height (angle of heap =  $0$  degrees) and cross-section in the bucket. The collection bucket is then put into the silo centrifuge model so that it is supported by the load cells. The distance from the centre of mass of the collection bucket and its contents to the axis of rotation of the centrifuge is  $1.235\text{m}$ .

By considering this radius of rotation, the angular velocity necessary to obtain specific centrifugal accelerations is calculated. By setting the centrifuge to these angular velocities (input as rotations per minute) the range of forces in table 4.2 were applied to the load cells.

Multiplying the mass of the sand and the bucket by the centrifugal acceleration acting at the centre of mass of the system allows the load applied to the load cells to be calculated. A range of centrifugal accelerations are chosen which apply total loads from  $0.049\text{kN}$  to  $1.954\text{kN}$  across both load cells. This range represents the range of loads which the load cells will measure during experiments. Table 4.2 shows the averaged data from a series of 3 tests to find the difference between applied force and output reading.

Table 4.2: Load cell calibration results

Gravity ratio ( $g^*/g$ ) [-]	Applied Load [kN]	Output (Averaged) [kN]	Error (Output/Applied) [-]
1.000	0.049	0.050	1.0226
9.958	0.488	0.490	1.0033
19.917	0.977	0.984	1.0071
29.875	1.465	1.470	1.0030
39.834	1.954	1.927	0.9864

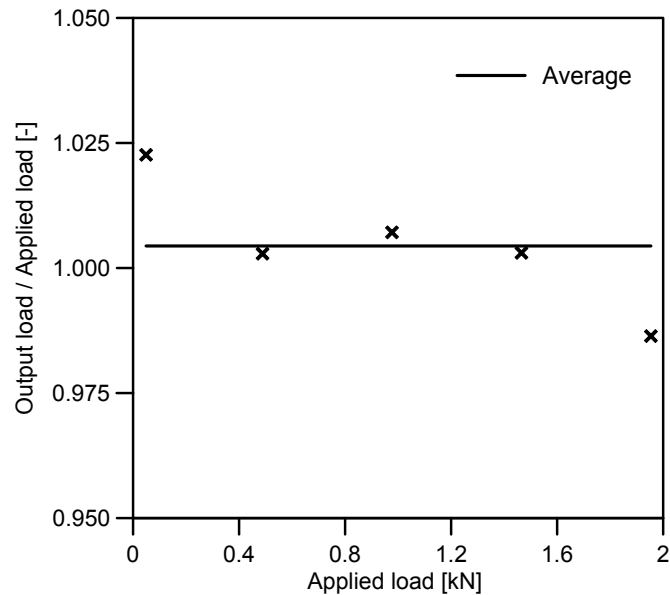


Figure 4.14: Difference between applied and output loads using 2 1kN C9B HBM Load Cells. Average error is 0.441%

## 4.6 Granular materials

Four materials are used during the tests. A poorly graded fine sand (DIN EN 12904), a poorly graded coarse sand (DIN 1164/58), a bi-disperse mixture of glass beads and a bi-disperse mixture of Polyamide granules. These are labelled M1 - M4, respectively.

#### 4. SILO CENTRIFUGE MODEL DESCRIPTION

---

Table 4.3: List of materials

Material	Label	Properties	Photograph
Fine Sand	M1	Table 4.4	Figure 4.15
Coarse Sand	M2	Table 4.5	Figure 4.16
Glass Beads	M3	Table 4.6	Figure 4.17
Polyamide	M4	Table 4.7	Figure 4.18

Material M1 is fine sand "DIN EN 12904" and is commonly used for water filtration purposes. It is used in this research because of its particle size distribution, (it is poorly graded like the standard sand), has well-defined properties and is readily available. Its bulk material properties are listed in table 4.4

Material M2 is "DIN 1164/58 Norm Sand II" and is a coarse silica sand. It is poorly graded and has well-defined properties (Table 4.5). The particle size distribution (Figure 4.20) and the angle of internal friction (Figure 4.21) is available from previous research using drained triaxial tests. (Klein [1998]) Table 4.5 shows the bulk material properties of the standard sand.

Table 4.4: Properties of material M1, Fine Sand DIN EN 12904

Property	Value
Material density $\rho_s$ [ $g/cm^3$ ]	2.65
Density range $\rho_{min}, \rho_{max}$ [ $g/cm^3$ ]	1.4 - 1.6
Void ratio $e_{min} e_{max}$ [-]	0.656 - 0.893
Coefficient of uniformity $U$ [-]	1.5
Friction angle $\theta_i$ [ $^\circ$ ]	34
Cohesion $c$ [ $kN/m^2$ ]	0

Table 4.5: Properties of material M2, Coarse sand DIN 1164/58 Normsand II

Property	Value
Material density $\rho_s$ [ $g/cm^3$ ]	2.644
Density range $\rho_{min}, \rho_{max}$ [ $g/cm^3$ ]	1.44 - 1.65
Void ratio $e_{min} e_{max}$ [-]	0.607 - 0.844
Coefficient of uniformity $U$ [-]	1.4
Friction angle $\theta_i$ [ $^\circ$ ]	34
Cohesion $c$ [ $kN/m^2$ ]	0

Table 4.6: Properties of material M3, bi-disperse mixture of glass beads

Property	Value
Particle diameters $d_1, d_2$ [mm]	$3.15 \pm 0.1, 1.45 \pm 0.1$
Average particle diameter $d_{50}$ [mm]	2.3
Material density $\rho_s$ [ $g/cm^3$ ]	2.750
Average density $\rho_b$ [ $g/cm^3$ ]	1.52
Void ratio $e$ [-]	0.809
Friction angle $\theta_i$ [ $^\circ$ ]	22
Cohesion $c$ [ $kN/m^2$ ]	0

Table 4.7: Properties of material M4, bi-disperse mixture of Polyamide

Property	Value
Particle diameters $d_1, d_2$ [mm]	$0.75 \pm 0.1, 1.5 \pm 0.1$
Average particle diameter $d_{50}$ [mm]	1.375
Material density $\rho_s$ [ $g/cm^3$ ]	1.1
Average density $\rho_b$ [ $g/cm^3$ ]	0.65
Void ratio $e$ [-]	0.692
Friction angle $\theta_i$ [ $^\circ$ ]	25
Cohesion $c$ [ $kN/m^2$ ]	0

#### 4. SILO CENTRIFUGE MODEL DESCRIPTION

---



Figure 4.15: Photograph of material M1, fine sand



Figure 4.16: Photograph of material M2, coarse sand



Figure 4.17: Photograph of material M3, glass beads mixture

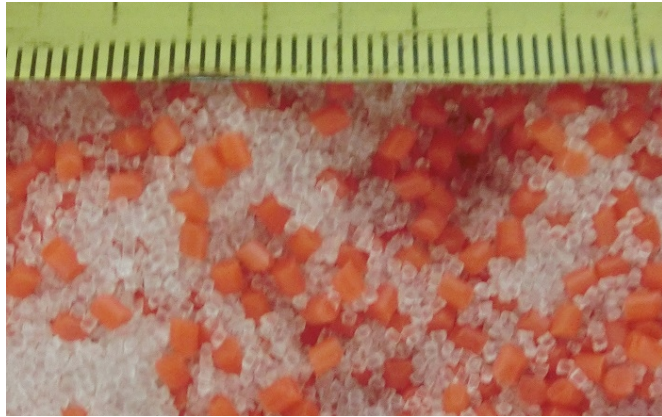


Figure 4.18: Photograph of material M4, Polyamide mixture

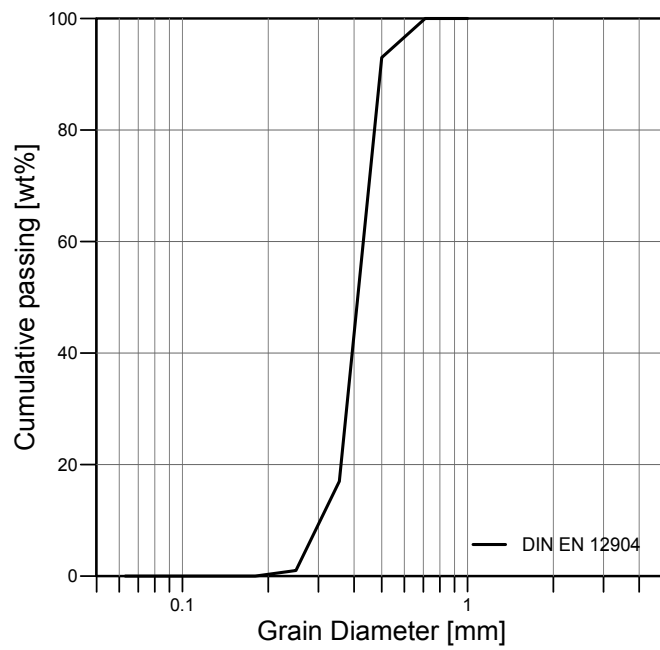


Figure 4.19: Grain size distribution of material M1: fine quartz sand DIN EN 12904

#### 4. SILO CENTRIFUGE MODEL DESCRIPTION

---

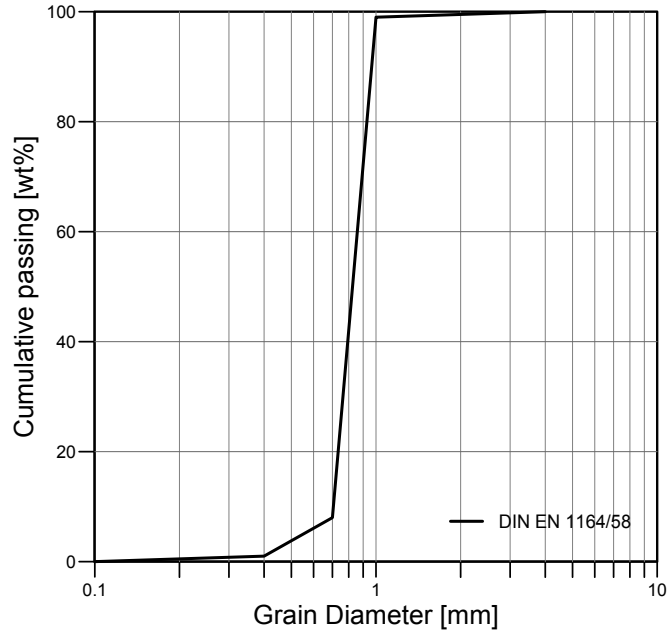


Figure 4.20: Particle size distribution of material M2: DIN 1164/58 Norm Sand II

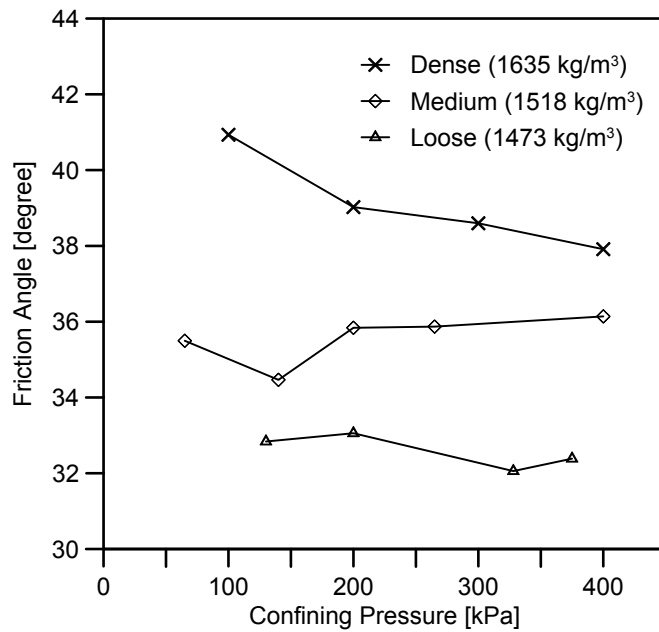


Figure 4.21: Results from triaxial tests on the coarse sand (M2) showing dependency of angle of internal friction on density and confining pressure (Klein, 1998)

---

## 4.7 Test procedure

Material is poured into the model silo through a funnel (Figure 4.6) at 1g. The mass of material in the silo is calculated by recording the mass of the storage bucket and funnel before and after filling (Table 4.8). In order to keep the video files organised, a note saying which test is about to be conducted is attached to the front of the silo so that it will be visible at the beginning of the video. The model lights and camera are then turned on. The camera must be zoomed and focused for each test and high-speed video camera begins recording before the centrifuge begins to rotate (Figure 4.22). It is not possible to remotely control the camera. Once the camera is recording the note showing which test is being conducted is removed from view and the centrifuge is closed.

In the control room, the load cell data begins to be recorded and the centrifuge is accelerated to the desired angular velocity (Table 4.10). Once the centrifuge reaches the required speed it is maintained for a short period to ensure it does not change significantly.

Silo discharge is initiated by activating the servo-motor from the control room. This causes a spindle attached to the motor to pull a string attached to a pin (Figure 4.8). When the pin is pulled the spring-loaded sliding door keeping the silo closed is pulled back to the side of the silo, leaving the opening unobstructed. The load cells then record the force exerted by the collection bucket and its contents.

Once discharge is complete, the centrifuge is decelerated until the beam is stationary. The load cell data then stops being recorded and the centrifuge is turned off. The centrifuge is then opened and the high-speed video camera is also turned off.

The collection bucket is weighed and the load cell data exported as an Excel file with with a unique name. Figure 4.23(a) shows typical data recorded by the load cells. The model is then reset. Tests at a specific acceleration are repeated until 3 tests with less than 5% variation in discharge rate are obtained (Typical data are shown in Table 4.9).

#### 4. SILO CENTRIFUGE MODEL DESCRIPTION

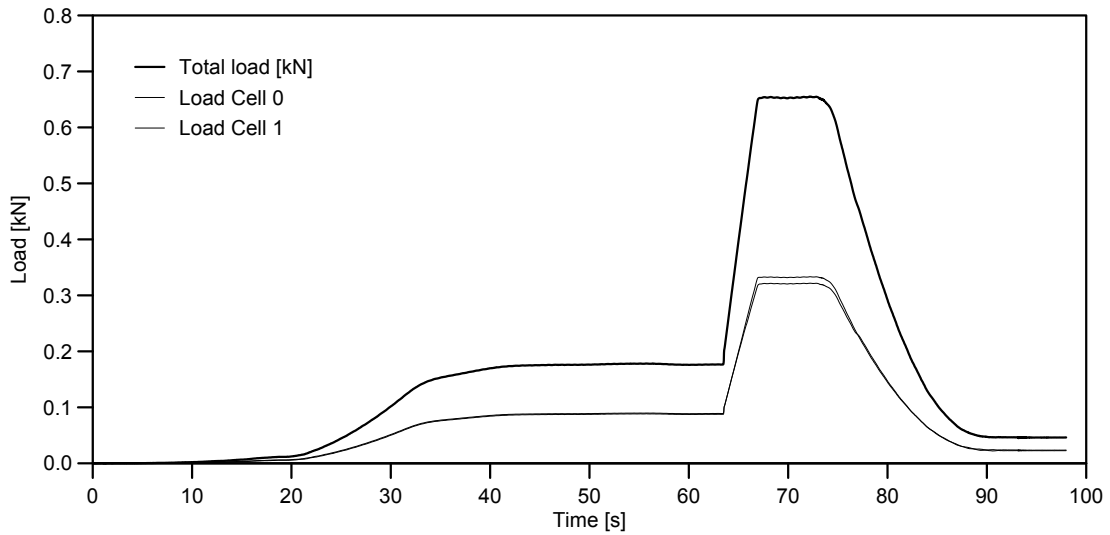
---



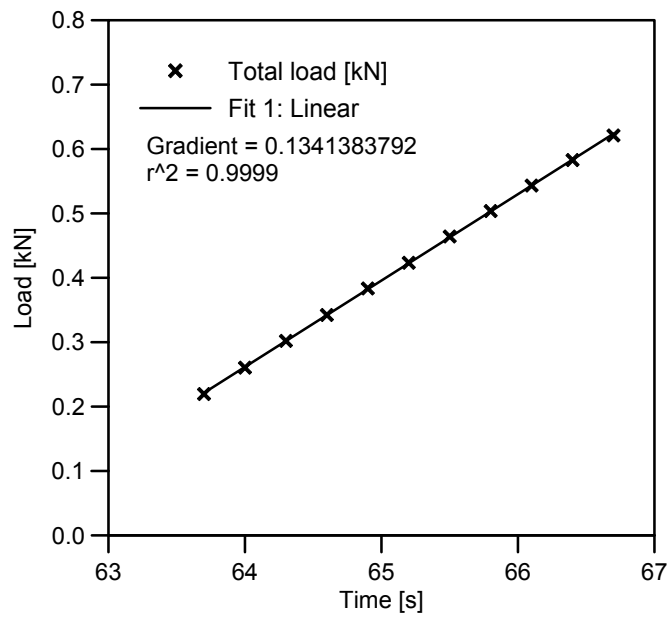
Figure 4.22: Typical test

Table 4.8: Typical tests from laboratory weighing scales. Fine Sand (M1) Model silo with 30 degree hopper

Test	Mass before filling (kg)	Mass after filling (kg)	Mass after test (kg)	Mass in silo before test (kg)	Mass discharged (kg)	Difference (kg)
15a	7.82	3.25	6.27	4.57	4.57	0.00
15b	7.80	3.22	6.25	4.58	4.55	0.03
15c	8.08	3.23	6.51	4.85	4.81	0.04
10a	8.02	3.23	6.44	4.79	4.74	0.05
10b	7.97	3.24	6.37	4.73	4.67	0.06
10c	7.90	3.25	6.34	4.65	4.64	0.01



(a) Entire test.



(b) Segment of test from which gradient is calculated.

Figure 4.23: Typical load cell result, Coarse sand, Flat bottomed silo, 10g

#### 4. SILO CENTRIFUGE MODEL DESCRIPTION

---

Table 4.9: Typical results using fine sand (M1) in flat-bottomed silo

Test	Gradient	Test	Gradient	Test	Gradient
1g A	0.0038	5g A	0.0506	10g A	0.1399
B	0.0037	B	0.0502	B	0.1405
C	0.0037	C	0.0486	C	0.1402
MEAN	0.0037		0.0498		0.1402
STD. DEV	5.7735E-05		1.0583E-03		3.0000E-03
RANGE	2.6%		3.95%		0.21%

Table 4.10: Centrifuge rotation speeds required for specified gravity at the silo outlet

N [-]	RPM [1/min]	RPS [1/sec]	Tangential speed [km/h]
1	-	-	-
5	64.50	1.08	37.04
10	91.22	1.52	52.38
15	111.72	1.86	64.15
20	129.00	2.15	74.07
30	157.99	2.63	90.72
40	182.43	3.04	104.75
45	193.50	3.23	111.11
50	203.97	3.40	117.12
55	213.92	3.57	122.83

# Chapter 5

## Experimental results

### 5.1 Introduction

In this chapter, results from the silo centrifuge experiments are presented. Four materials were each tested at 4 gravities corresponding to 1g, 5g, 10g and 15g. Experiments were conducted in a silo with a flat bottom and a silo with a hopper inclined 30 degrees to the vertical. Each test was repeated at least 3 times so that the repeatability of the test was assured. Sections 5.5 to 5.11 each present one aspect of the experimental results. A summary is included at the end of this chapter. Table 5.1 shows the values used to calculate the discharge rates predicted using the Beverloo correlation.

### 5.2 Method and instrumentation

The readings from the load cells are used to calculate the mass flow rate. The readings are adjusted to consider the increased radius of the centre of mass of the discharged material.

The high-speed camera records the movement of grains behind the transparent acrylic wall. In this way, only the front layer of particles are visible and only the front layer of particles are considered in the PIV analysis. A velocity profile is calculated

## 5. EXPERIMENTAL RESULTS

---

Table 5.1: Values used for flow rate prediction

Property	Fine sand (M1)	Coarse sand (M2)	Glass beads (M3)	Polyamide (M4)
Bulk density $\rho_b$ [ $kg/m^3$ ]	1500	1545	1520	650
Mean particle diameter $d_0$ [m]	4E-4	8.5E-4	2.3E-3	1.4E-3
$C$ [-]	1.03	1.03	1.03	1.03
$k$ [-]	1	1	1	1
Friction angle $\phi_i$ [ $^\circ$ ]	35	35	22	25
Outlet diameter $W_0$ [m]	0.01	0.01	0.03	0.03

across the width of the silo using data output from the Particle Image Velocimetry (PIV) analysis. Considering the principles of conservation of mass and planar flow, the discharge rate is calculated using this method as well as with the load cells. These two methods are independent of each other.

The discharge rate is calculated by integrating the flow profile and assuming planar flow. This gives only an approximation of the mass flow rate because some friction with the front and back walls will inevitably produce shear gradient. However since the flow rates calculated according to these two methods are nearly identical, the friction force between the front or back wall and the granular material seems to have little effect on the flow rate.

### 5.3 Results presentation

The observed discharge results are compared to those predicted using the Beverloo correlation. This is made clearer by dividing the observed value by the predicted value. This also allows quantifiable observation of the effect of gravity on the silo discharge rate, where a horizontal trend shows that discharge is proportional to the square root of gravity.

Flow profiles are analysed using a similar method. The local velocity is divided by the square root of the gravity multiplied by outlet diameter to give a dimensionless value.

---

Since the outlet diameter does not change between tests with the same material, the normalised flow profiles will be the same if local velocities are proportional to the square root of the gravity.

## 5.4 Repeatability

The repeatability of the tests from 1g to 15g is high. The differences between the individual discharge rates at each condition is less than 5% at 15g and decreases with gravity. Whilst it is possible to conduct experiments at gravities higher than 15g the repeatability of the tests decreases because the silo opening mechanism becomes less reliable.

## 5.5 Verification of centrifugal acceleration

The total discharge time of silo centrifuge tests with glass beads and Polyamide was presented. The Beverloo correlation predicts that if the silo is discharging freely under the action of gravity then the discharge time at increased gravities will be equal to the discharge time at 1g multiplied by the square root of the factor of gravity increase. This relationship can be used to check that the silo is discharging consistently and as expected.

$$W \propto \sqrt{g^*} \quad \therefore \quad \frac{t_2}{t_1} = \sqrt{\frac{g_1^*}{g_2^*}} \quad (5.1)$$

$$t_2 = t_1 \sqrt{\frac{g_1}{g_2}} = t_1 N^{-0.5} \quad (5.2)$$

where  $W$  is the mass discharge rate [ $kg/s$ ],  $t$  is time [ $s$ ] and  $g_1$ ,  $g_2$  are arbitrary accelerations due to gravity.

The correlation of the experimental results with this relationship is quantified by

## 5. EXPERIMENTAL RESULTS

---

plotting the average discharge time of tests at each gravity against factor of gravity  $N = g_2/9.81 m/s^2$ . The high correlation factor shows that the angular velocities calculated to produce apparent gravities of specific magnitudes is accurate and that the silo outlet is unobstructed.

Figure 5.1 shows data from the load cells during silo discharge. Increasing gravity is shown to decrease the total discharge time and increase the rate of loading on the load cells. The high degree of repeatability is also evident.

In Figures 5.2 and 5.3 the discharge time response to gravity is shown. The discharge time plotted on the ordinate is the total time taken for the silo to discharge. The gravity factor  $N$  plotted on the abscissa is the acceleration due to gravity divided by  $9.81 m/s^2$ . The mass of material is approximately the same at all gravities but was not kept precisely constant and a variation of upto 20 grammes between tests was recorded. This is likely the largest cause of deviation from the trend. Equation 5.1 predicts that the data lies on a trend described by a power law. The equation of the trend line for material M3 (glass beads) in the silo with flat bottom is  $t = 2.5206N^{-0.5024}$ . The equation of the trend line for material M4 (polyamide) in the silo with flat bottom is  $t = 2.3929N^{-0.6528}$ . The equation of the trend line for material M3 in the silo with 30 degree hopper is  $t = 2.2793N^{-0.5432}$ . The equation of the trend line for material M4 in the silo with 30 degree hopper is  $t = 2.0087N^{-0.5169}$ . As would be expected, the coefficient in front of the variable is very close to the value of discharge time from the silo at  $N = 1$ . The correlation between the data and the trend line is calculated using the coefficient of determination and shows good agreement ( $R^2$  is close to 1).

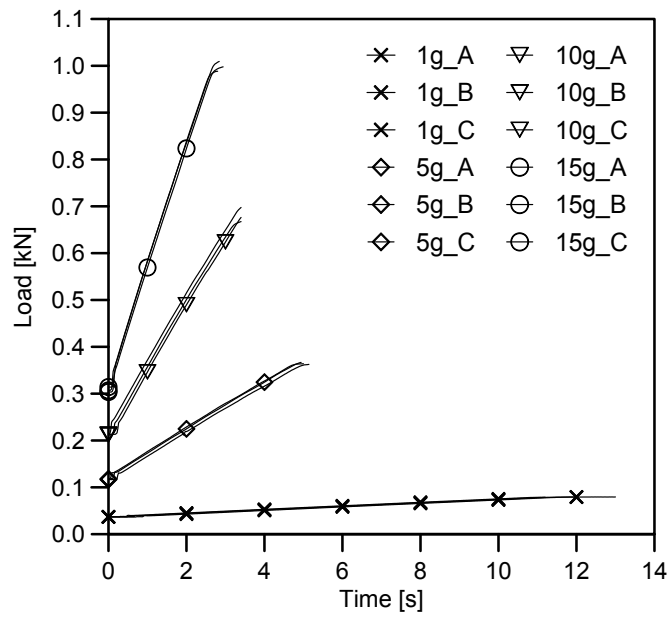


Figure 5.1: Data from load cells

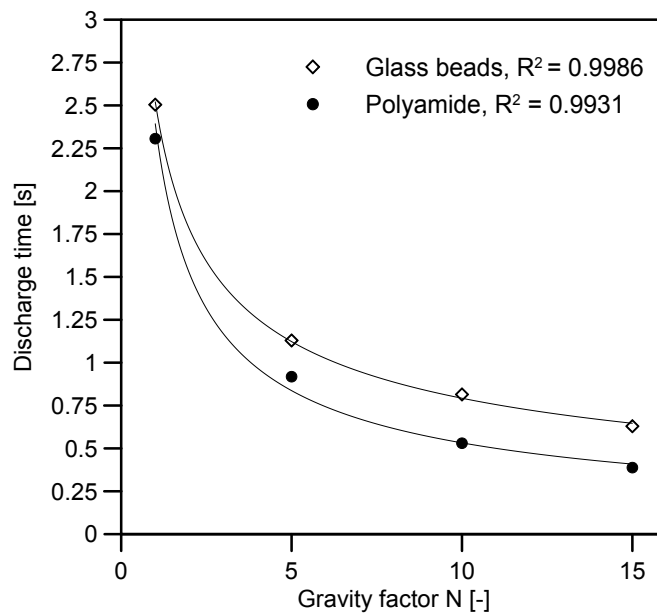


Figure 5.2: Discharge times in silo with flat bottom

## 5. EXPERIMENTAL RESULTS

---

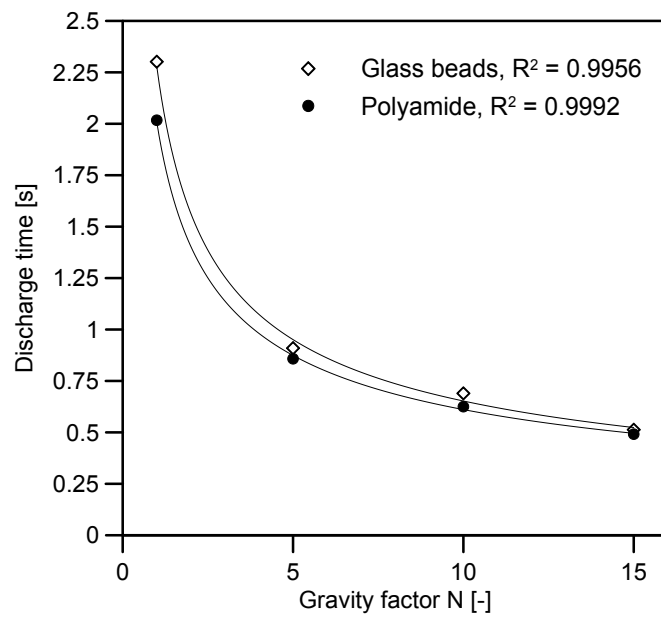


Figure 5.3: Discharge times in silo with 30 degree hopper

---

## 5.6 Flow acceleration

The acceleration of material in a region of the silo directly above the outlet was investigated in order to quantify the length of time it took for the flow pattern to become stable in the bottom half of the silo. Once it is known when the flow pattern becomes stable, a time-averaging method can be reliably used.

This time-averaging method is used in Sections 5.9 - 5.11 to find the temporally-averaged flow profile of material inside the silo along a horizontal line 112mm above the silo outlet. This is the average flow profile between 10% of silo discharge and 40% of silo discharge. The results presented in this section show that the flow pattern during discharge becomes stable at between 5% and 10% discharged. Therefore it is reasonable to average flow velocities after the silo is 10% discharged.

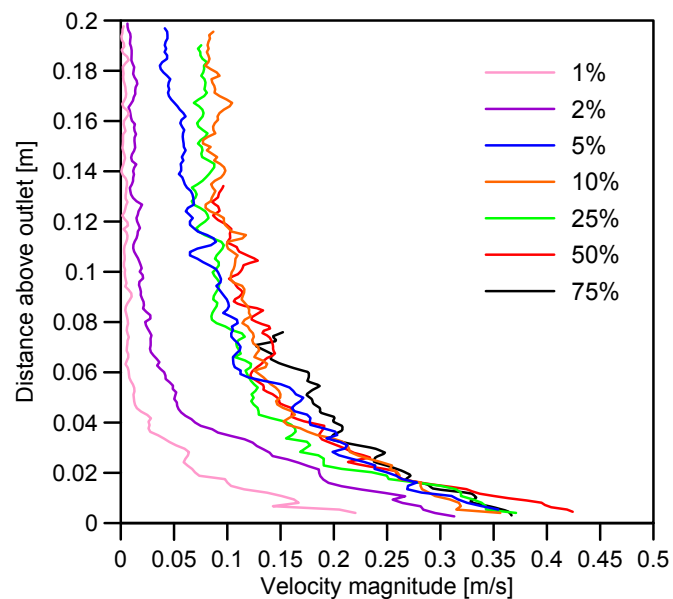


Figure 5.4: Velocity magnitude of material above outlet at different stages of discharge in silo with flat bottom

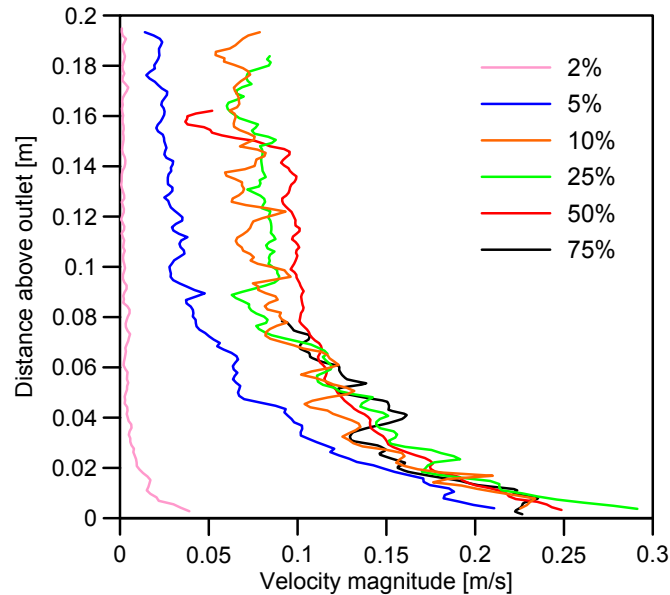


Figure 5.5: Velocity magnitude of material above outlet at different stages of discharge in silo with 30 degree hopper

## 5.7 Discharge rates

The rate of discharge of different materials from each silo at different gravities is calculated using load cells and image analysis techniques. The observed discharge rates are compared to either the Beverloo model for flat-bottomed silos, or to an adjusted Beverloo model for the silo with 30 degree hopper. The value of the  $C$  coefficient is 1.03 and the value of the  $k$  coefficient is 1.

The results show that the Beverloo model gives good predictions and the shape of the curve closely matches the observed data. The magnitude of the predicted discharge rates are approximately 10% larger than those observed. For the coarse and fine sands, the Particle Image Velocimetry analysis shows accurate results which can lead to quantitative analysis of flow profiles within the silo. The PIV results under-report the discharge rates of materials Polyamide and Glass beads, which shows the importance of material texture for PIV analysis. For these materials only a qualitative discussion of the results is possible.

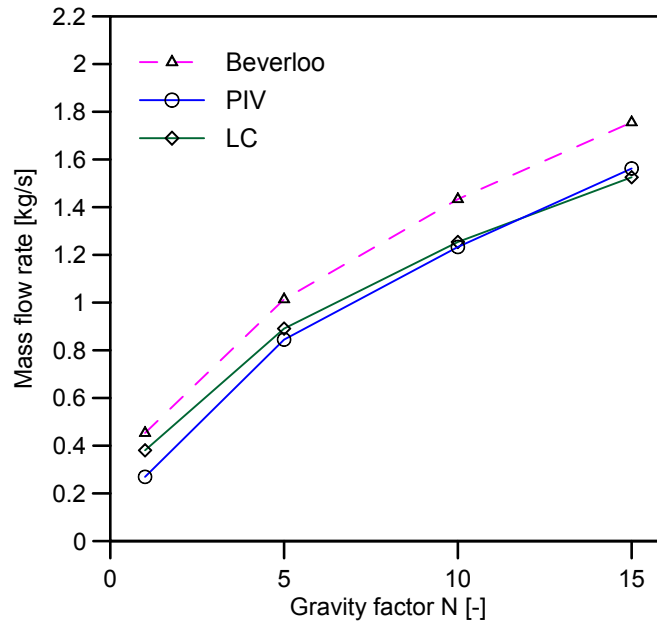


Figure 5.6: Discharge rates, Material M1 - Fine sand, Silo with flat bottom

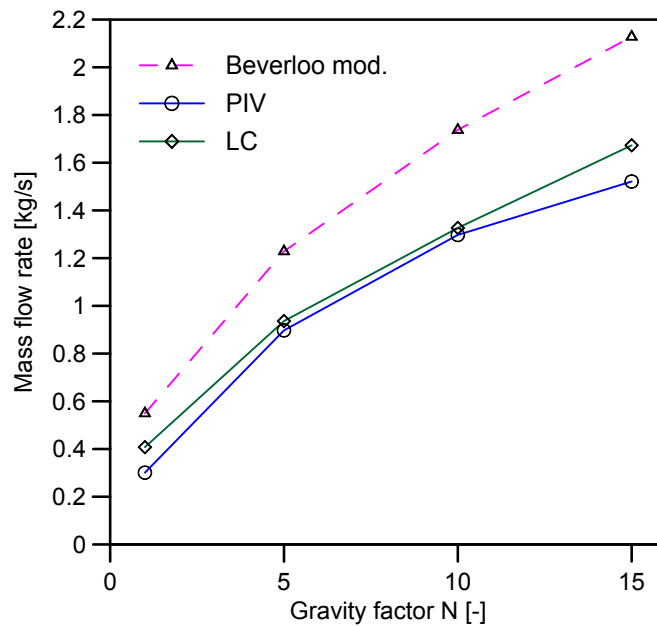


Figure 5.7: Discharge rates, Material M1 - Fine sand, Silo with 30 degree hopper

## 5. EXPERIMENTAL RESULTS

---

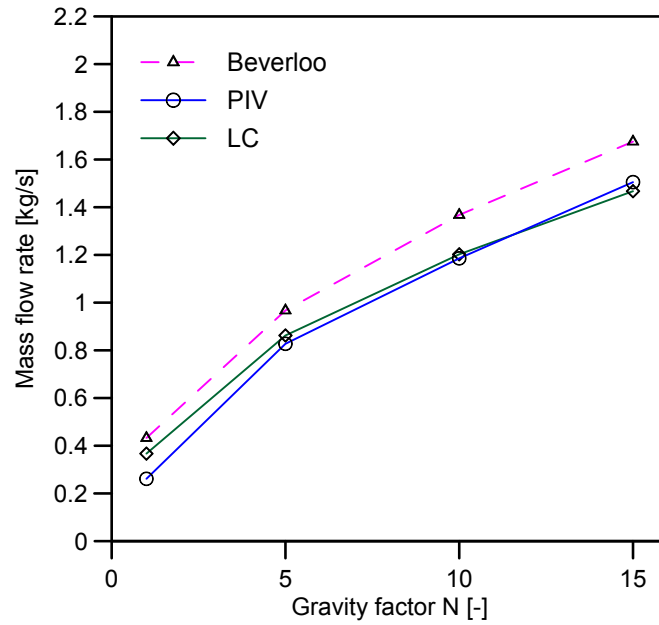


Figure 5.8: Discharge rates, Material M2 - Coarse sand, Silo with flat bottom

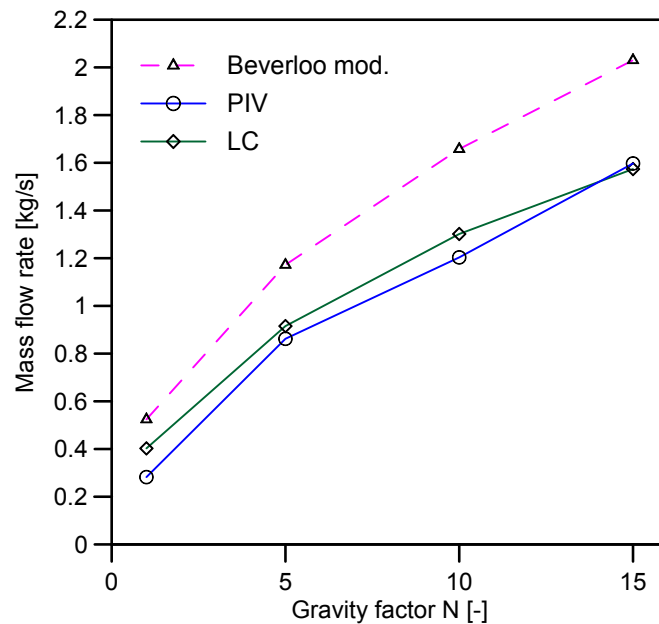


Figure 5.9: Discharge rates, Material M2 - Coarse sand, Silo with 30 degree hopper

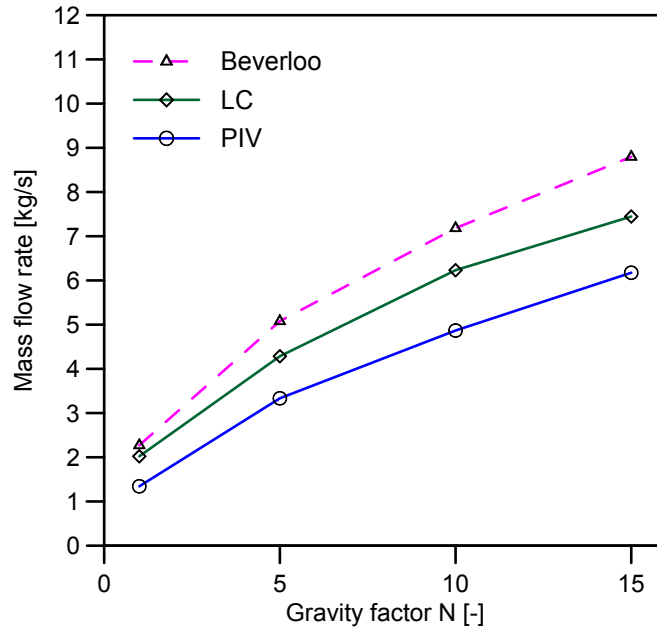


Figure 5.10: Discharge rates, Material M3 - Glass beads, Silo with flat bottom

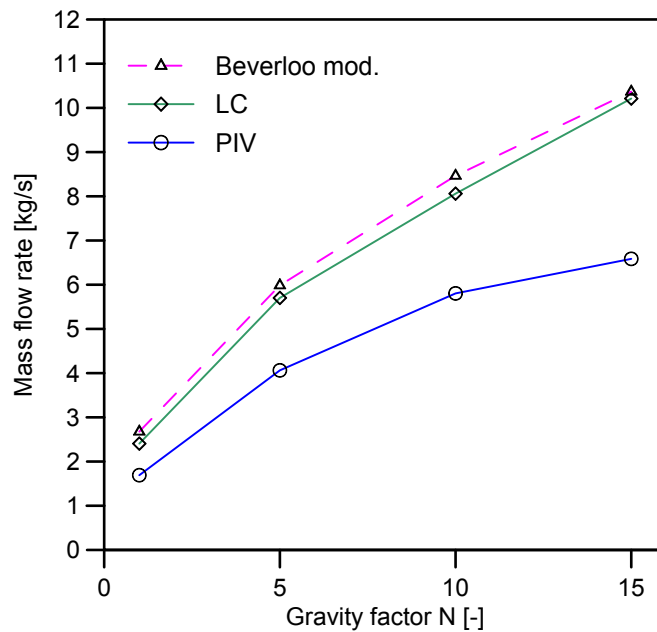


Figure 5.11: Discharge rates, Material M3 - Glass beads, Silo with 30 degree hopper

## 5. EXPERIMENTAL RESULTS

---

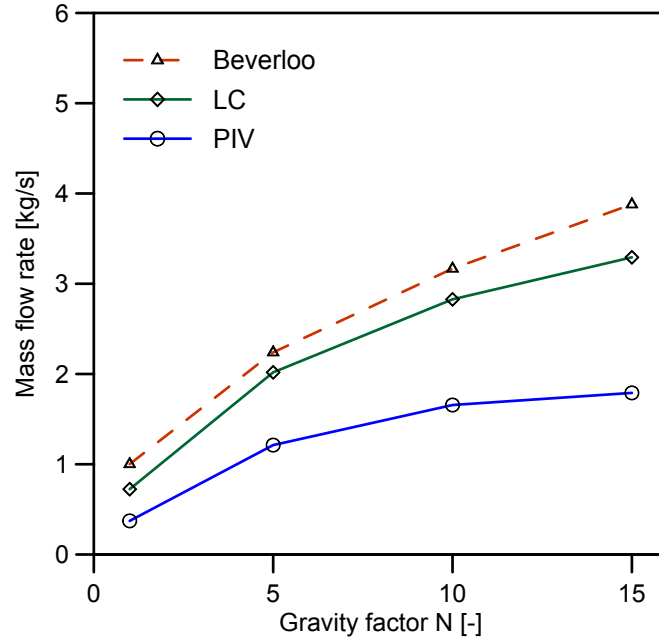


Figure 5.12: Discharge rates, Material M4 - Polyamide, Silo with flat bottom

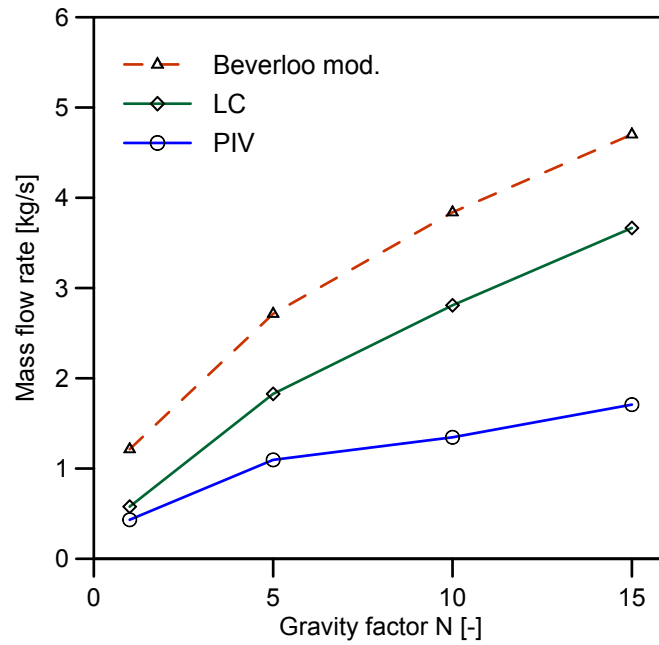


Figure 5.13: Discharge rates, Material M4 - Polyamide, Silo with 30 degree hopper

---

## 5.8 Scaled discharge rates

The ratio of observed discharge rates to predicted discharge rates is presented in order to allow comparison between different materials, silos and gravities. The results are scaled as a fraction of the value predicted using either the Beverloo correlation for flat bottom silos or a modified Beverloo correlation (Section [2.2.5](#)) for the silo with 30 degree hopper.

## 5. EXPERIMENTAL RESULTS

---

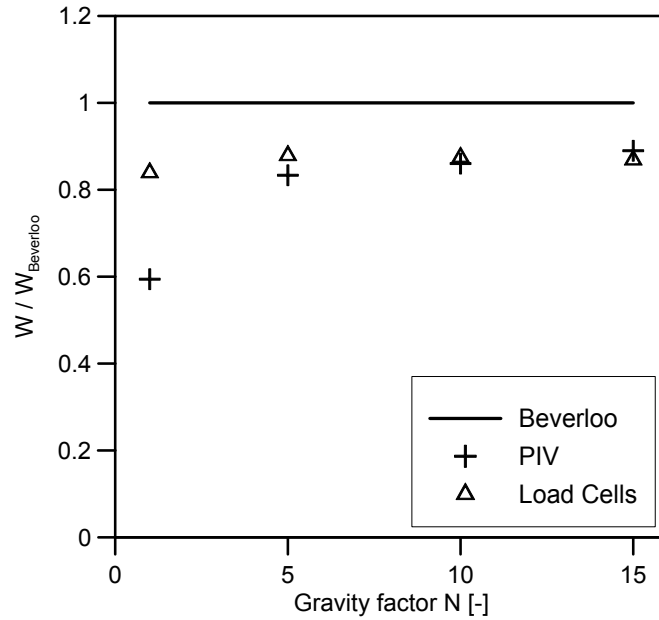


Figure 5.14: Normalised discharge rates, Material M1 - Fine sand, Silo with flat bottom

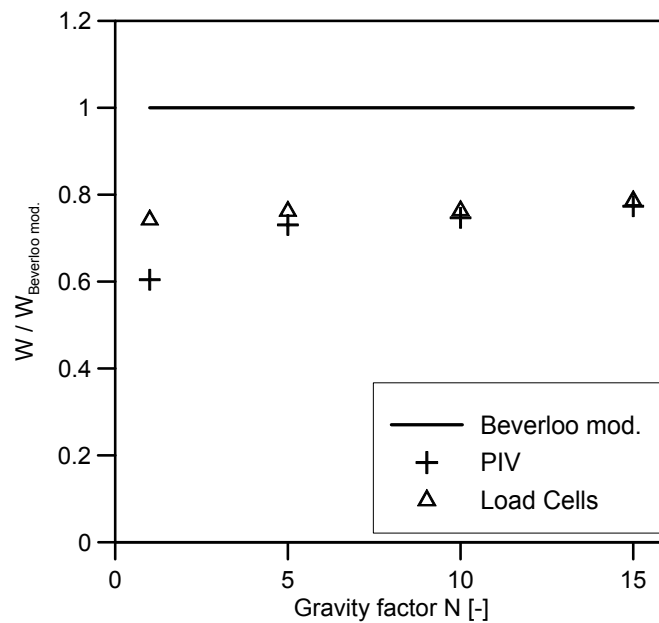


Figure 5.15: Normalised discharge rates, Material M1 - Fine sand, Silo with 30 degree hopper

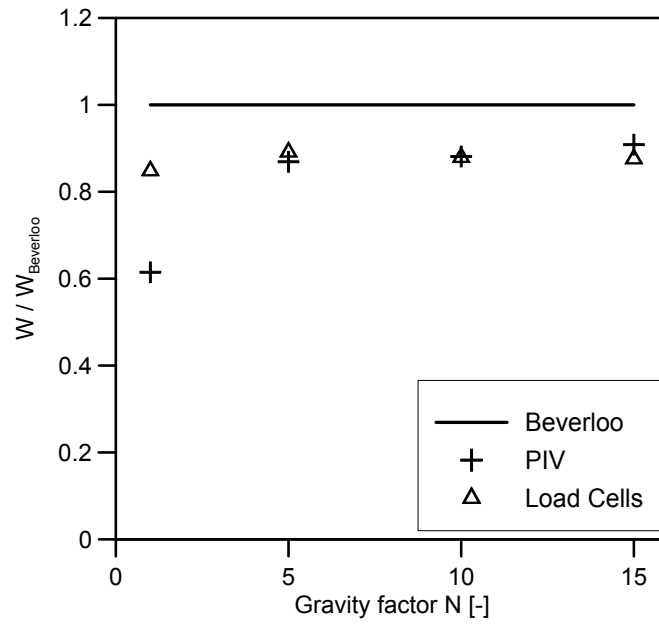


Figure 5.16: Normalised discharge rates, Material M2 - Coarse sand, Silo with flat bottom

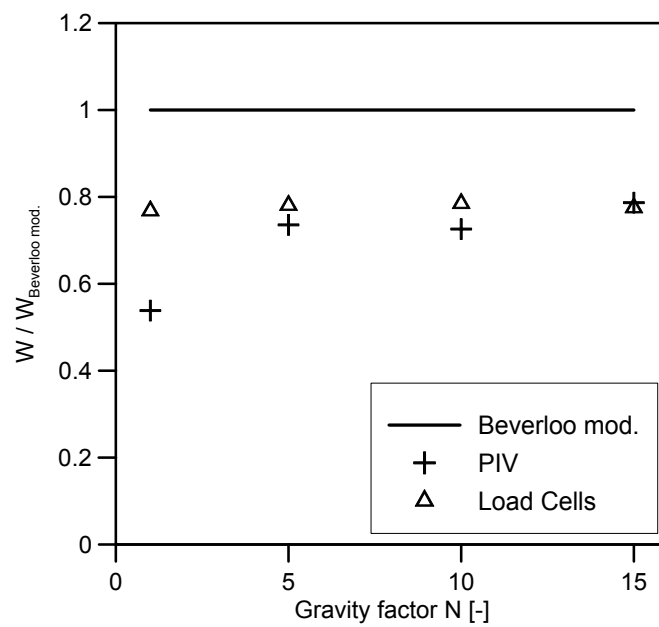


Figure 5.17: Normalised discharge rates, Material M2 - Coarse sand, Silo with 30 degree hopper

## 5. EXPERIMENTAL RESULTS

---

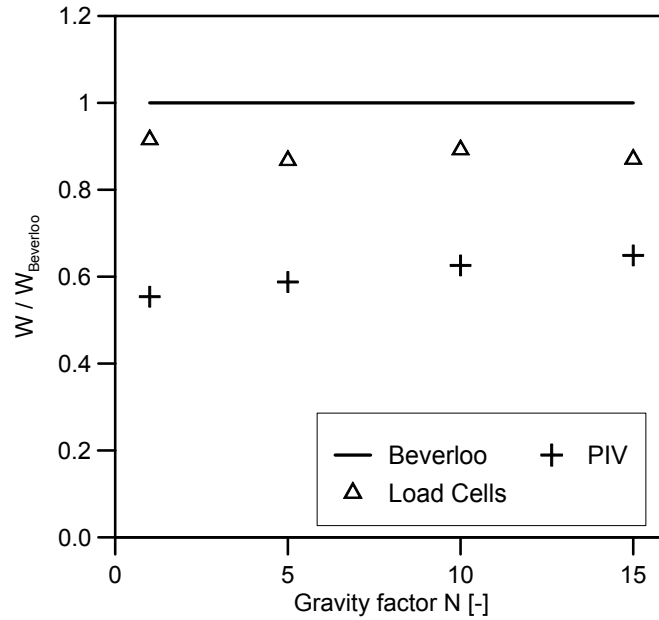


Figure 5.18: Normalised discharge rates, Material M3 - Glass beads, Silo with flat bottom

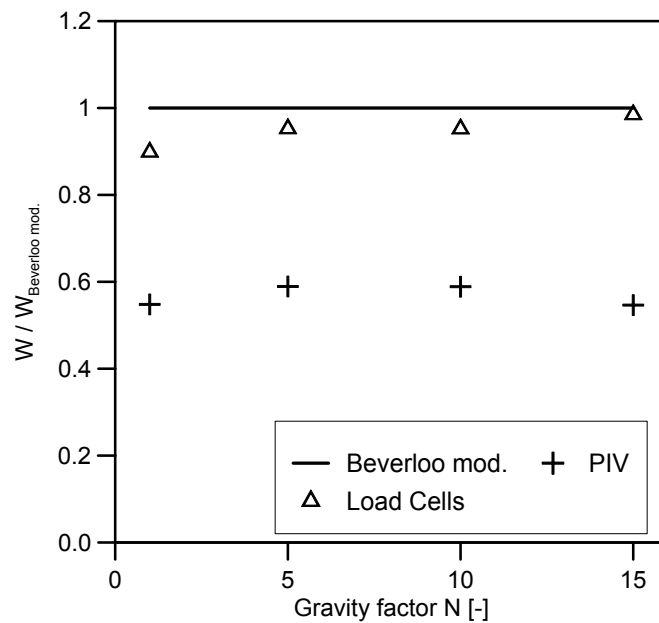


Figure 5.19: Normalised discharge rates, Material M3 - Glass beads, Silo with 30 degree hopper

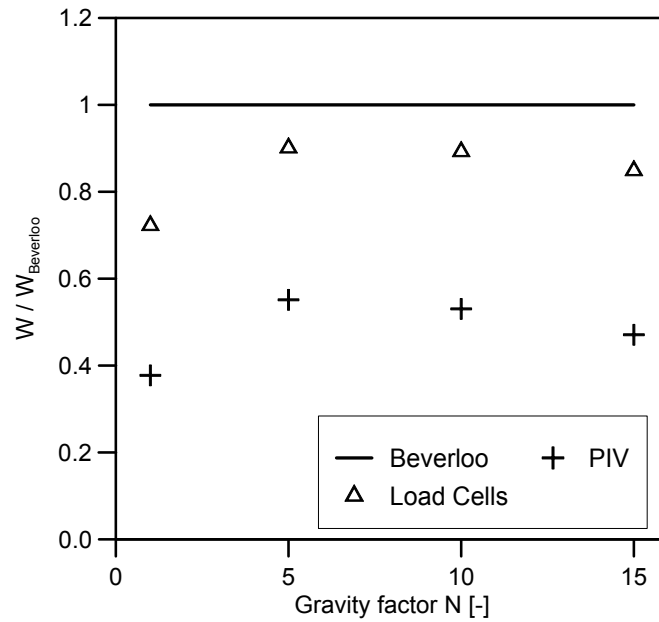


Figure 5.20: Normalised discharge rates, Material M3 - Polyamide, Silo with flat bottom

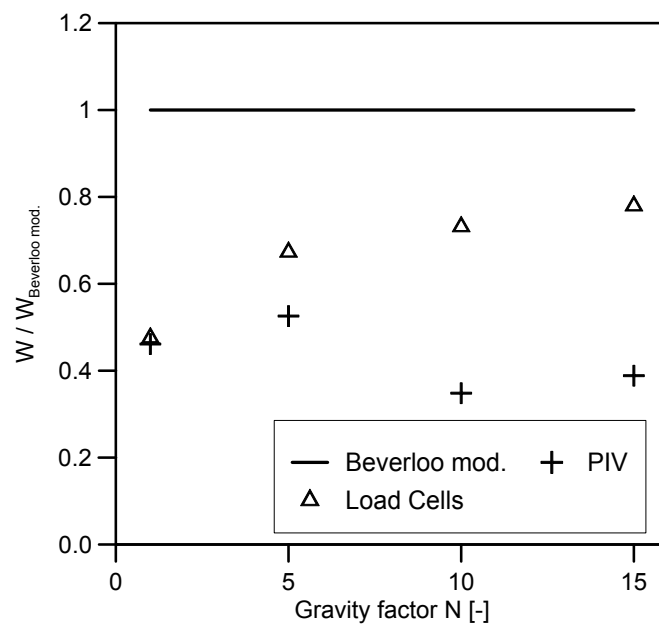


Figure 5.21: Normalised discharge rates, Material M3 - Polyamide, Silo with 30 degree hopper

## 5.9 Normalised flow profiles

The normalised flow profiles compare the internal flow behaviours of the silo during discharge at different gravities. The normalisation technique is shown in equation 5.3. The normalised profiles are calculated along a horizontal line 112mm above the silo outlet. In the silo with 30 degree hopper, this corresponds to the transition between the hopper and vertical sections.

$$V_{i,n} = \frac{V_i}{\sqrt{g^* W_0}} \quad (5.3)$$

The results show that material M1 discharges with a flow pattern at 1g that is significantly different to the flow pattern at higher gravities. This is seen from the decreased peak of the normalised velocity profile in Figures 5.22 5.23 5.30 and 5.31. At gravities 5g, 10g and 15g, the normalised flow profiles have a high degree of similarity and contrast with the flow profiles at 1g.

Material M1 shows a behaviour in the hopper that is not observed with the other materials. Figure 5.23 shows that the velocity of material sliding against the wall of the silo increases with increasing gravity. Also it is seen that the flow pattern is only proportional to  $\sqrt{g^* W_0}$  towards the centre of the silo between approximately  $\pm 75$  particle diameters. At widths greater than this, the vertical component of the flow velocity increases at a rate greater than  $\sqrt{g^* W_0}$ . However, significant asymmetry is observed and the causes and consequences of this are discussed below.

Figures 5.30 and 5.31 show the horizontal component of the materials flow velocity along the same horizontal line 112mm above the outlet. The trends are compatible with the observations drawn from the vertical component plots in Figures 5.22 and 5.23. It is seen that the normalised horizontal velocity components at 1g are significantly smaller than at gravities higher than 1g. In Figure 5.31 there is a higher degree of asymmetry which corresponds to the asymmetry observed in Figure 5.23. This suggests that the direction of flow is the same at every gravity.

For material M2, no slip is observed along the silo walls at any gravity, i.e. mass flow

---

is never observed, unlike with the fine sand (M1). This is unexpected because the two materials have similar properties including angle of internal friction ( $\theta_i \approx 34^\circ$ ) and bulk density.

Material M2 also shows a different behaviour at 1g than for other gravities. This is similar to what is observed for material M1. The normalised vertical component of the flow profile at 1g is significantly smaller than it is at 5g, 10g or 15g. In the silo with a flat bottom, the peak-normalised vertical flow at the centre of the silo is approximately 35% smaller than it is at 5g, 10g or 15g (Figure 5.24). In the silo with 30 degree hopper, the peak-normalised velocity component is 30% smaller than the average normalised velocity component at other gravities, though there is a larger variation in the results at 5g, 10g, and 15g (Figure 5.25).

Figures 5.32 and 5.33 show the horizontal component of velocity and show that the degree of symmetry is less than was observed in material M1.

Material M3 “Bi-disperse mixture of spherical glass beads” shows a very smooth set of normalised flow profiles with the highest degree of similarity observed in all four materials tested (Figures 5.34 and 5.35). Mass flow is observed in all cases, as is evidenced by the non zero normalised velocity components at the edges of the silo. The difference between the peak normalised velocity components at different gravities is also small and is considered insignificant because the accuracy of these measurements is known to be less than for materials M1 and M2.

Material M3 has a very low angle of internal friction ( $\approx 22^\circ$ ) and therefore it was expected that mass flow would be observed as well as a wide and shallow flow profile. The highest degree of symmetry is also expected in the smoothest material with the least internal shear, and this is observed. Figures 5.34 and 5.35 show that horizontal component of material flow is also highly symmetric.

The flow profiles for material M4 (bi-disperse mixture of Polyamide particles) are shown in Figures 5.28 and 5.37. The wide flat peak observed in Figure 5.28 is more pronounced than for other materials. The results are less consistent for material M4 than for materials M1 - M3 and this is probably the result of the decreased accuracy of the Particle Image Velocimetry owing to the reduced contrast in the images. Nonethe-

## 5. EXPERIMENTAL RESULTS

---

less, the expected trend is observed when discharge rate is calculated and therefore a qualitative discussion of Figures 5.28 - 5.37 is possible. In the flat-bottomed silo the normalised velocity at 1g is 25% less than at the other gravities. However, this is not observed in the silo with 30 degree hopper, where two distinct trends are observed for 1g and 5g, and then for 10g and 15g. This is attributed to the low contrast used in the PIV analysis.

Figures 5.36 and 5.37 show that there was a high degree of asymmetry in the Polyamide tests. The reason why there would be greater asymmetry for M4 than for materials M1-M3 is unclear and is perhaps either the result of a small partial obstruction at one side of the outlet due to the silo door not being completely open, or is the result of poor image quality in the PIV analysis.

Table 5.2: PIV vertical component integrals

		$(g^*/g)$				Mean
		1	5	10	15	
M1	Flat	0.0017957	0.0056321	0.0082216	0.0104150	0.0065161
	Hopper	0.0020059	0.0059821	0.0086494	0.0109720	0.0069024
M2	Flat	0.0016916	0.0053558	0.0076742	0.0097427	0.0061161
	Hopper	0.0018266	0.0055807	0.0077894	0.0102700	0.0063667
M3	Flat	0.0080477	0.0190950	0.0287580	0.0365180	0.0231047
	Hopper	0.0096501	0.0232030	0.0327840	0.0372650	0.0257255
M4	Flat	0.0058160	0.0189930	0.0258440	0.0280980	0.0196878
	Hopper	0.0086159	0.0219540	0.0205660	0.0280980	0.0198085
Mean		0.0049312	0.0132245	0.0175358	0.0214223	0.0142785

Table 5.3: PIV horizontal component integrals

		$(g^*/g)$				Mean
		1	5	10	15	(Modulus)
M1	Flat	0.00004453	-0.00010071	0.00001378	-0.00027927	0.00010957
	Hopper	0.00009339	0.00002414	-0.00042134	0.00091389	0.00036319
M2	Flat	-0.00014479	-0.00015182	0.00004874	0.00048212	0.00020687
	Hopper	0.00008961	-0.00019884	0.00004487	0.00007112	0.00010111
M3	Flat	0.00010495	0.00021839	0.00023676	0.00039210	0.00023805
	Hopper	-0.00008406	0.00094414	-0.00058267	-0.00063018	0.00056026
M4	Flat	0.00001700	-0.00078936	-0.00009784	0.00043046	0.00033367
	Hopper	-0.00006476	0.00209900	-0.00386540	-0.00319090	0.00230501
Mean		0.00008039	0.00056580	0.00066392	0.00079875	0.00052722

## 5. EXPERIMENTAL RESULTS

---

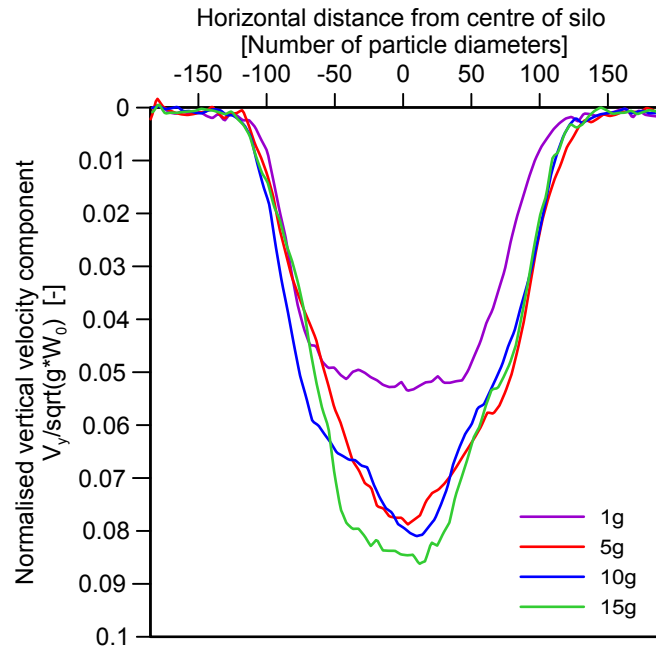


Figure 5.22: Normalised flow profiles, vertical velocity component, Material M1 - Fine sand, Silo with flat bottom

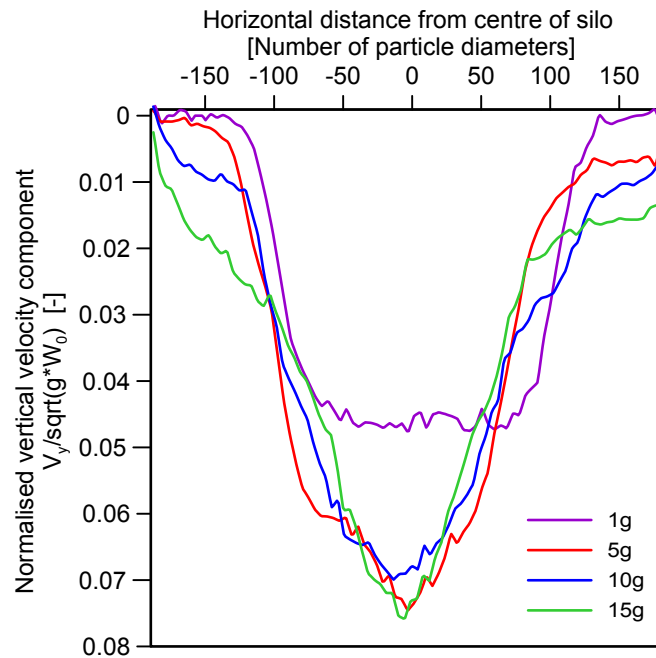


Figure 5.23: Normalised flow profiles, vertical velocity component, Material M1 - Fine sand, Silo with 30 degree hopper

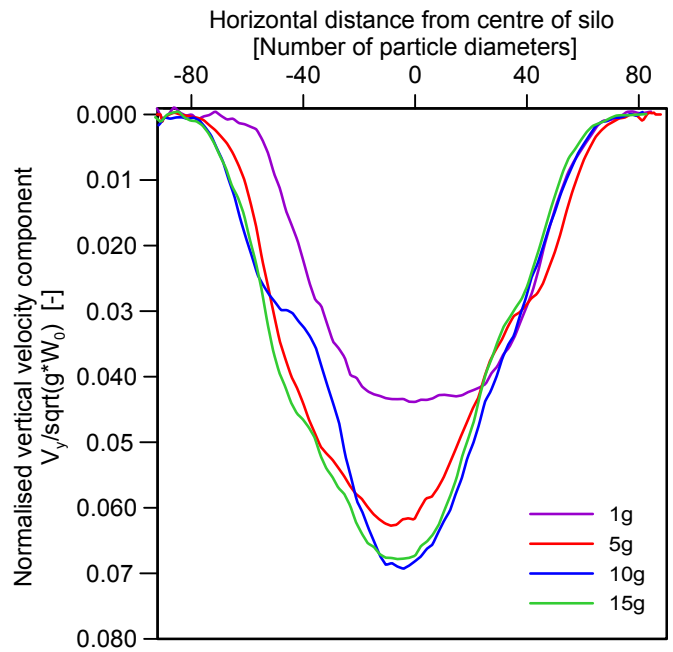


Figure 5.24: Normalised flow profiles, vertical velocity component, Material M2 - Coarse sand, Silo with flat bottom

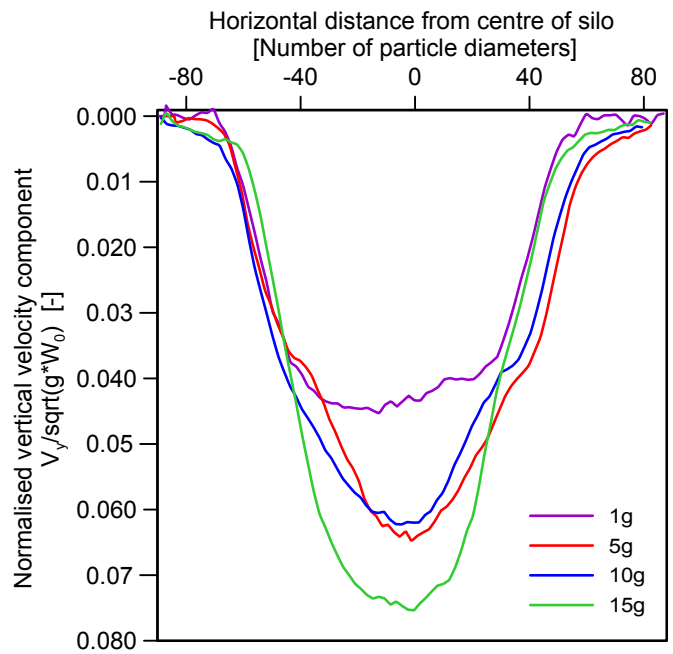


Figure 5.25: Normalised flow profiles, vertical velocity component, Material M2 - Coarse sand, Silo with 30 degree hopper

## 5. EXPERIMENTAL RESULTS

---

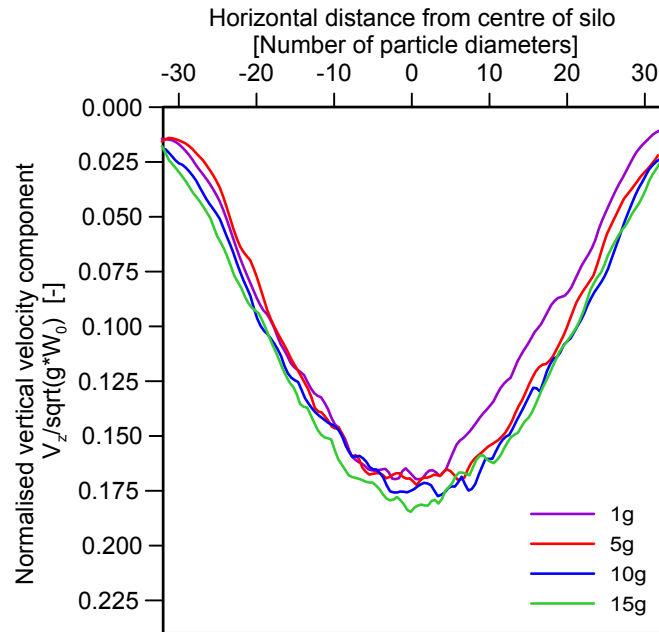


Figure 5.26: Normalised flow profiles, vertical component, Material M3 - Glass beads, Silo with flat bottom

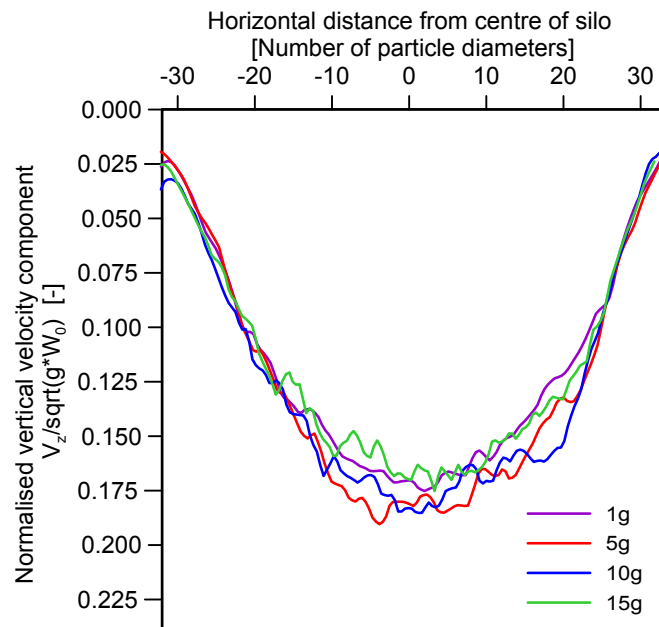


Figure 5.27: Normalised flow profiles, vertical component, Material M3 - Glass beads, Silo with 30 degree hopper

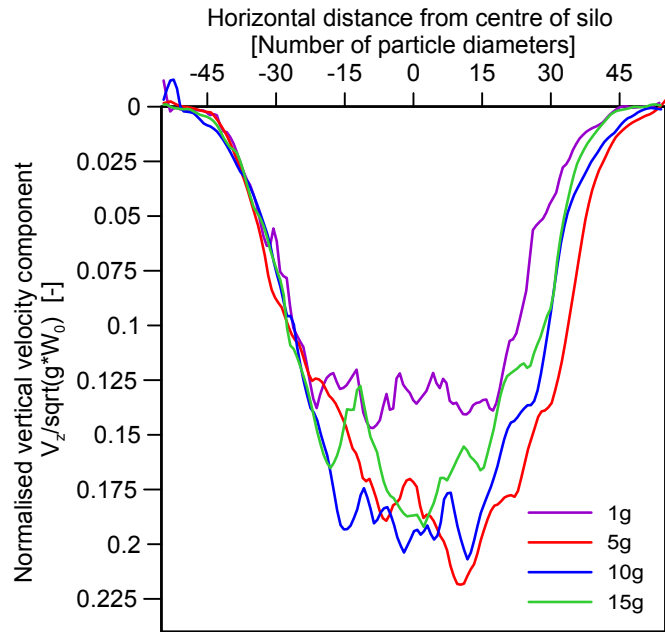


Figure 5.28: Normalised flow profiles, vertical component, Material M4 - Polyamide, Silo with flat bottom

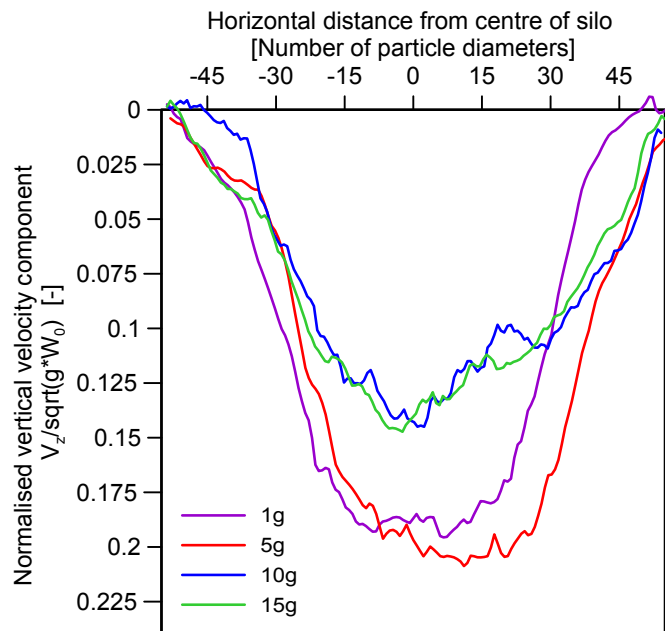


Figure 5.29: Normalised flow profiles, vertical component, Material M4 - Polyamide, Silo with 30 degree hopper

## 5. EXPERIMENTAL RESULTS

---

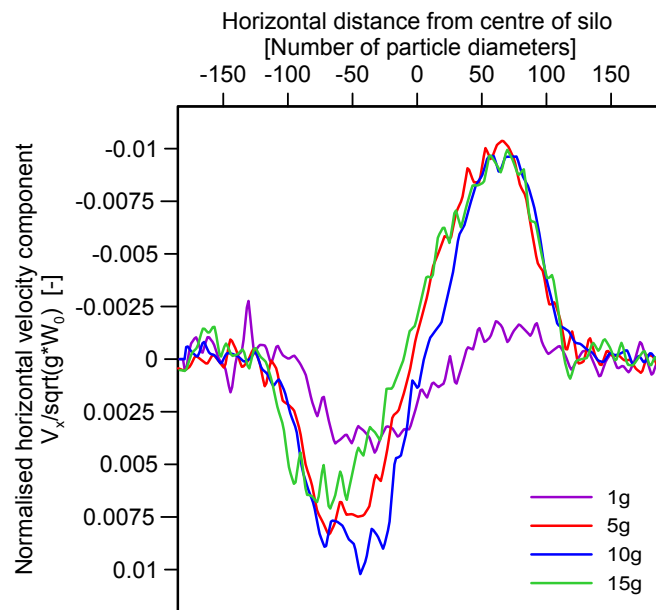


Figure 5.30: Normalised flow profiles, horizontal velocity component, Material M1 - Fine sand, Silo with flat bottom

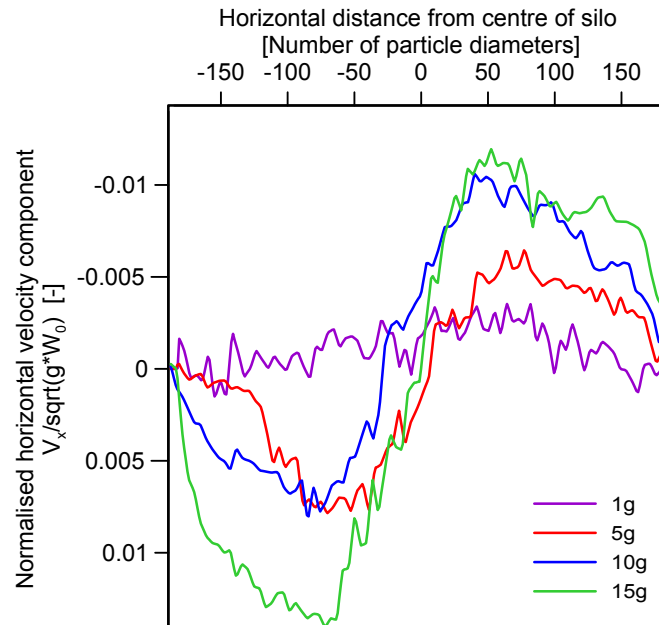


Figure 5.31: Normalised flow profiles, horizontal velocity component, Material M1 - Fine sand, Silo with 30 degree hopper

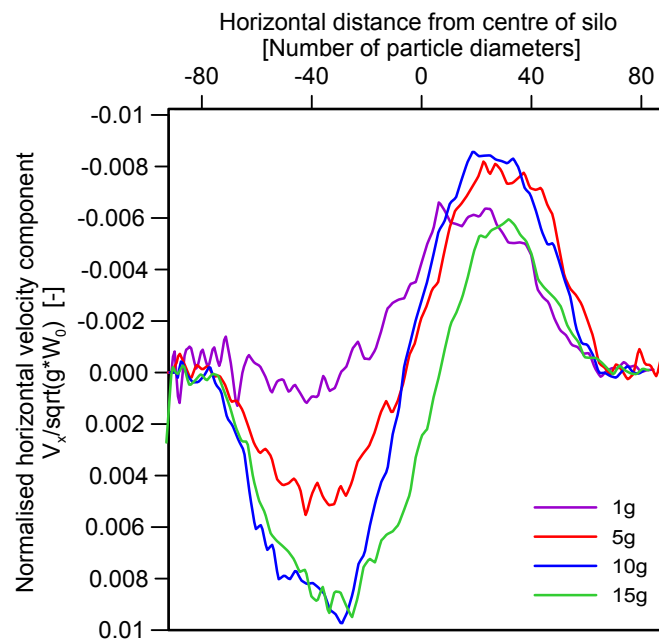


Figure 5.32: Normalised flow profiles, horizontal velocity component, Material M2 - Coarse sand, Silo with flat bottom

## 5. EXPERIMENTAL RESULTS

---

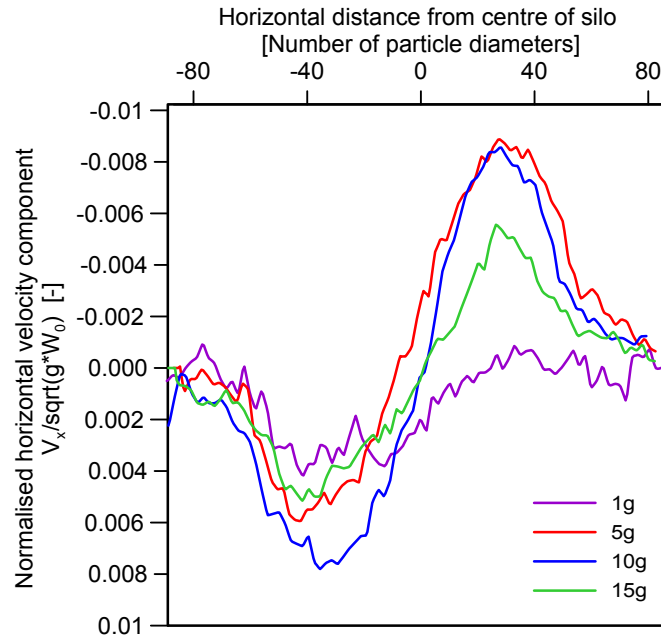


Figure 5.33: Normalised flow profiles, horizontal velocity component, Material M2 - Coarse sand, Silo with 30 degree hopper

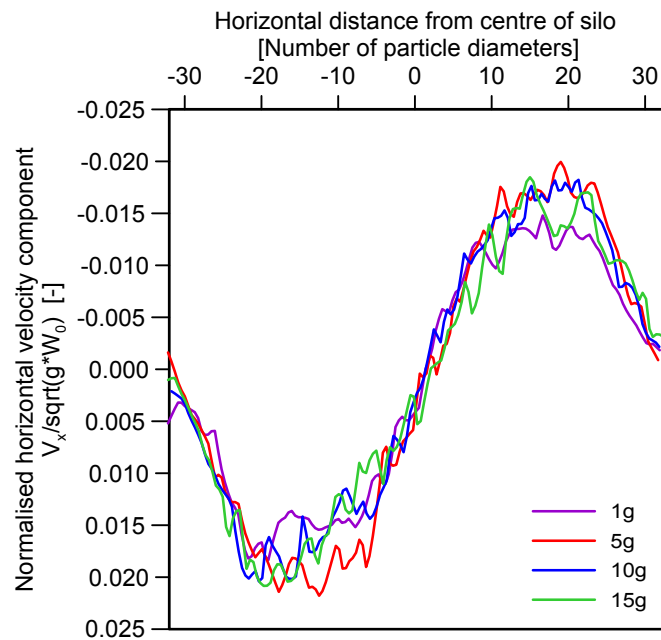


Figure 5.34: Normalised flow profiles, horizontal component, Material M3 - Glass beads, Silo with flat bottom

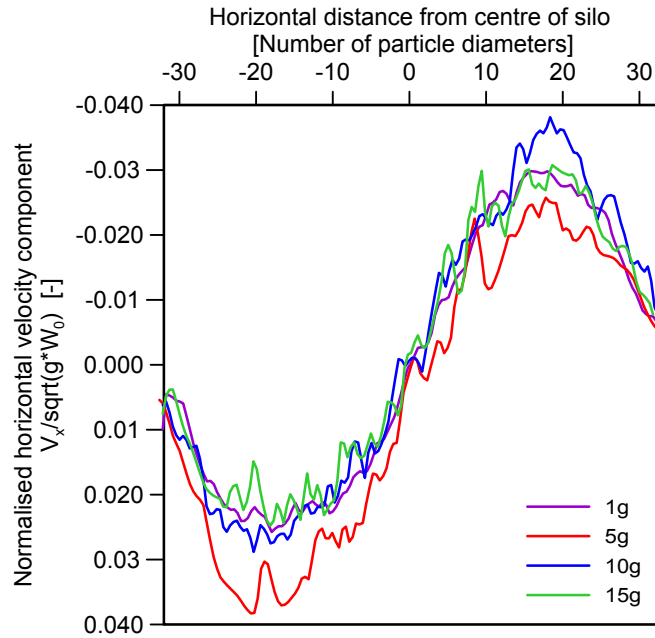


Figure 5.35: Normalised flow profiles, horizontal component, Material M3 - Glass beads, Silo with 30 degree hopper

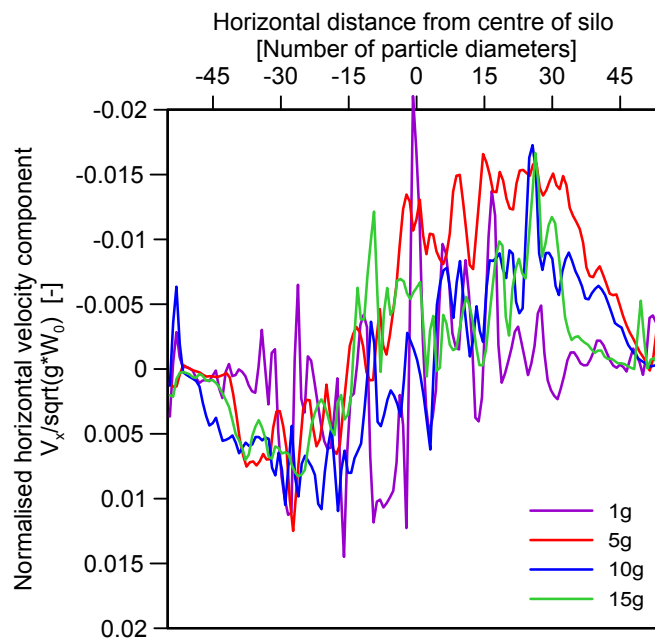


Figure 5.36: Normalised flow profiles, horizontal component, Material M4 - Polyamide, Silo with flat bottom

## 5. EXPERIMENTAL RESULTS

---

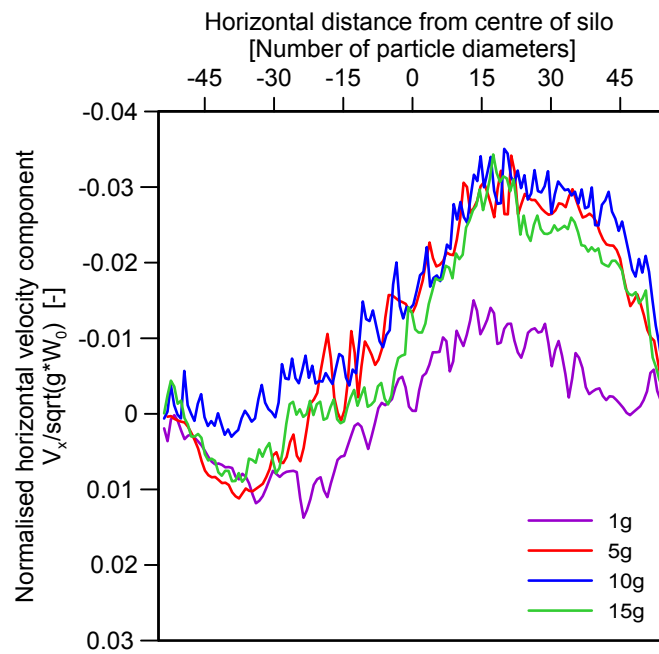


Figure 5.37: Normalised flow profiles, horizontal component, Material M4 - Polyamide, Silo with 30 degree hopper

---

## 5.10 Flow profiles at different heights

This section presents the averaged velocity components of discharging material at different locations. The velocity magnitude is temporally averaged between 10% and 20% discharged. The results in Section 5.6 show that this is a representative average.

Figures 5.38 - 5.41 show the vertical velocity component of glass beads discharging from the flat-bottomed silo from 1g to 15g. The same trend is observed at all gravity levels where the velocity of discharging material decreases as height above the outlet increases. The flow profile is most peaked at a  $z/w$  ratio of 0.37 corresponding to 55.5mm above the outlet and the flow profile is flattest at the maximum  $z/w$  ratio of 1.1 ( $z = 165mm$ ).

It is seen that the normalised velocity profiles always cross each other at approximately  $\pm 0.2x/w$  ( $\pm 30mm$ ) and this shows that the shape of the flow pattern is independent of gravity.

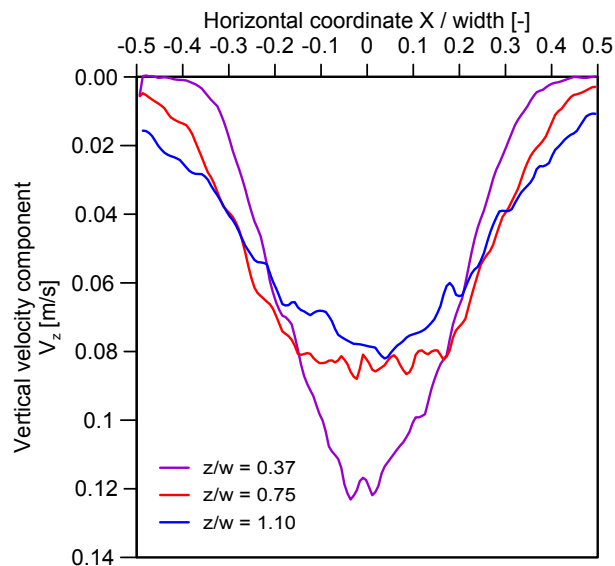


Figure 5.38: Normalised flow profiles at 3 different heights at 1g, Material M3 - Glass beads, Silo with flat bottom

## 5. EXPERIMENTAL RESULTS

---

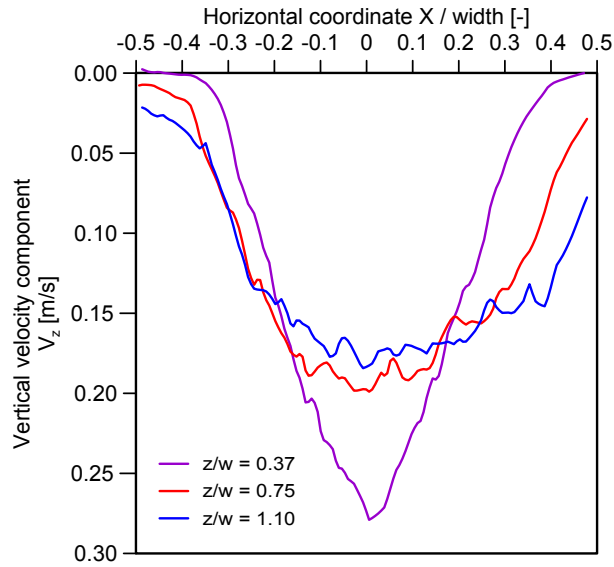


Figure 5.39: Normalised flow profiles at 3 different heights at 5g, Material M3 - Glass beads, Silo with flat bottom

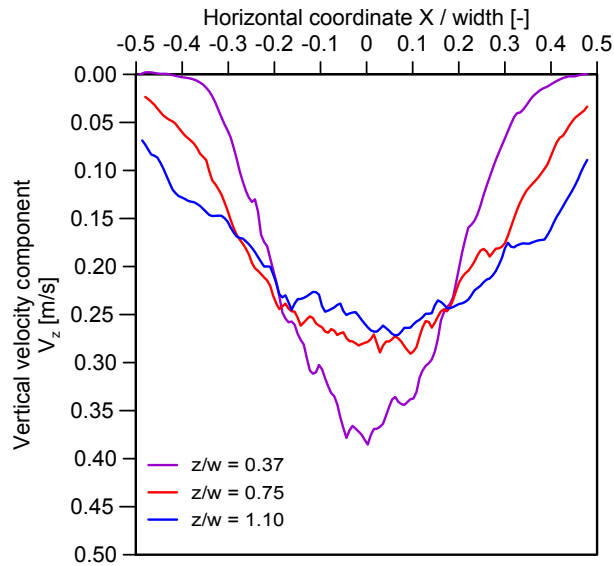


Figure 5.40: Normalised flow profiles at 3 different heights at 10g, Material M3 - Glass beads, Silo with flat bottom

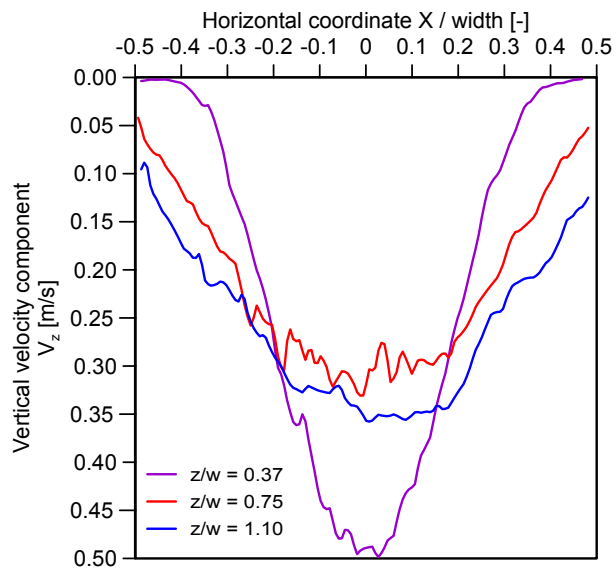


Figure 5.41: Normalised flow profiles at 3 different heights at 15g, Material M3 - Glass beads, Silo with flat bottom

### **5.11 Flow profile comparison with different silo geometry**

This section compares the influence of silo geometry on the flow profiles. The flow profiles are the average velocity magnitude between 10% and 20% discharged at 10g using the glass beads mixture. It can be seen that the hopper increases the velocities of the discharging material at the sides of the silo but does not increase the peak velocity, which is governed by gravity.

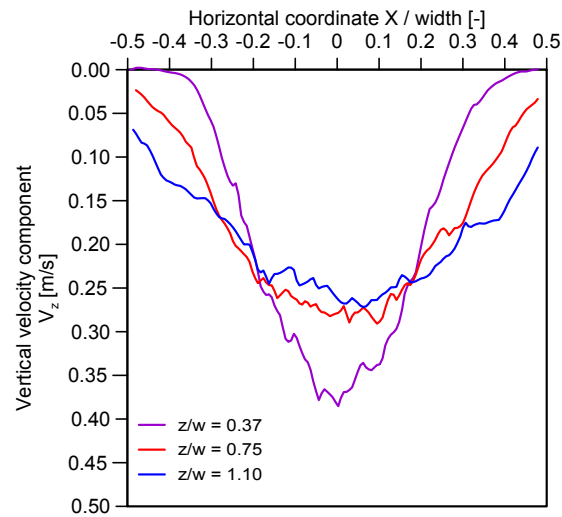


Figure 5.42: Normalised flow profiles at 3 different heights at 10g, Material M3 - Glass beads, Silo with flat bottom

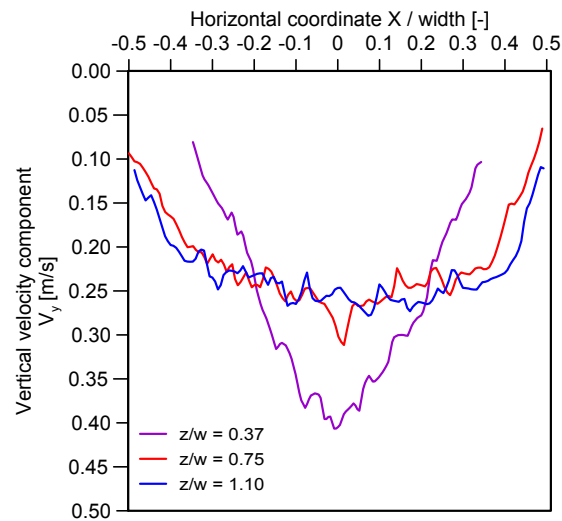


Figure 5.43: Normalised flow profiles at 3 different heights at 10g, Material M3 - Glass beads, Silo with 30 degree hopper

### 5.12 Settlement

#### Background

As centrifugal acceleration increases, the body forces exerted on the material will also increase and this will result in settlement of the material as the body forces are redistributed. This will produce an increase in the bulk density and a decrease in the volume and height of the top surface of the material. The amount of settlement is quantified so that changes in density can be calculated, which allows more accurate estimation of bulk characteristics including the friction angle and the lateral stress ratio. The density increase in material M2 “Coarse sand” as a result of centrifugal acceleration is presented.

#### Method

After pluvial filling from a narrow central outlet, a symmetrical heap with constant height from the front to the back of the silo is produced. The material is poured from a constant height throughout filling and therefore the material falls further at the beginning of filling than towards the end. The filling height ranges from 306mm to 0mm. The bulk density immediately after filling in a 1g environment has an average value of  $1497.6\text{kg}/\text{m}^3$ . This was calculated by measuring the mass and volume of the sand in the silo.

The front wall of the silo is made of transparent acrylic. High-speed video recorded the front layer of grains behind the acrylic during centrifugal acceleration from 1g up to the test conditions. Material movement during this time was tracked using a Particle Image Velocimetry (PIV) analysis using GeoPIV. The final displacements were used to calculate settlement. Planar displacements were assumed.

Figure 5.44 shows the regions that were used in the analysis. The PIV code “GeoPIV” was used to assess the settlement of the material because a Lagrangian PIV code is required to track deformation over multiple time steps. This is necessary because total deformation is calculated by tracking deformation across a series of frames. The

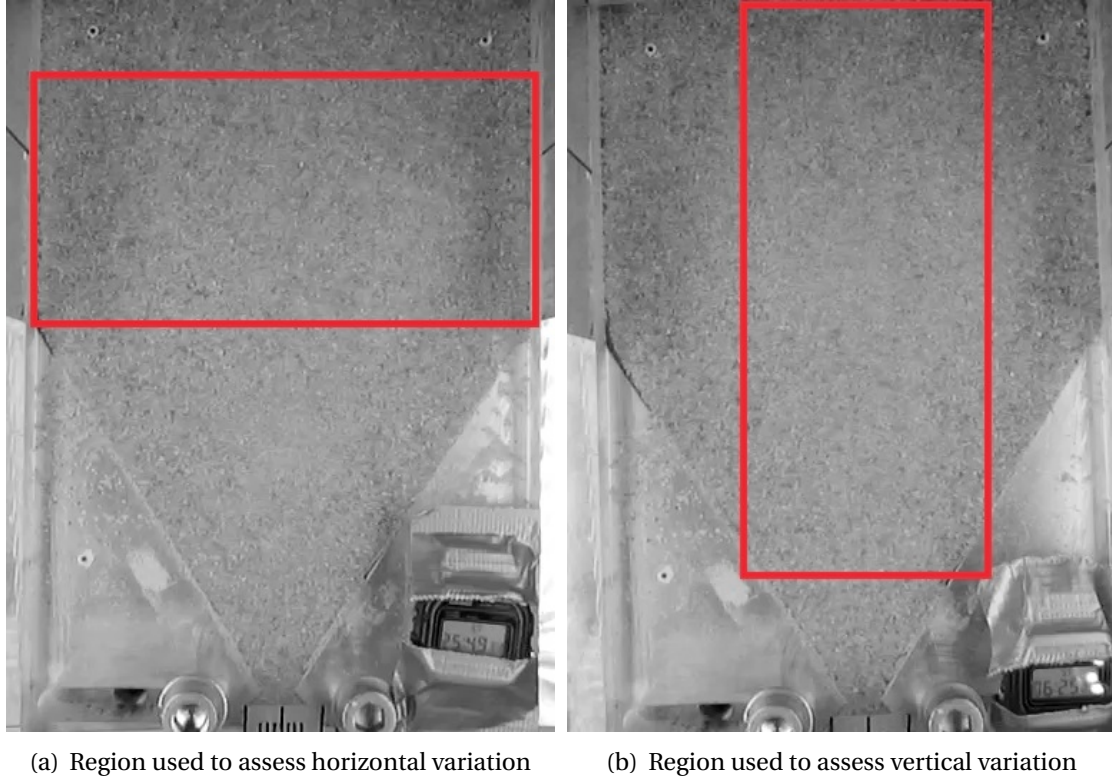


Figure 5.44: Region of silo used in PIV settlement analysis

resulting mesh deformation shows how the material settles during the acceleration phase of silo centrifuge tests. The settlement across a large part of the silo's height was investigated (Figure 5.44(b)).

## Results

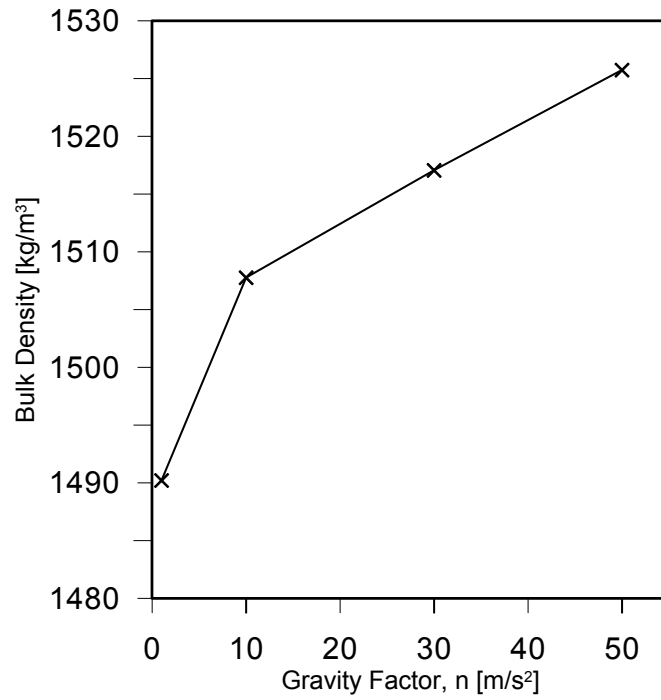


Figure 5.45: Density increase as a result of increased gravity

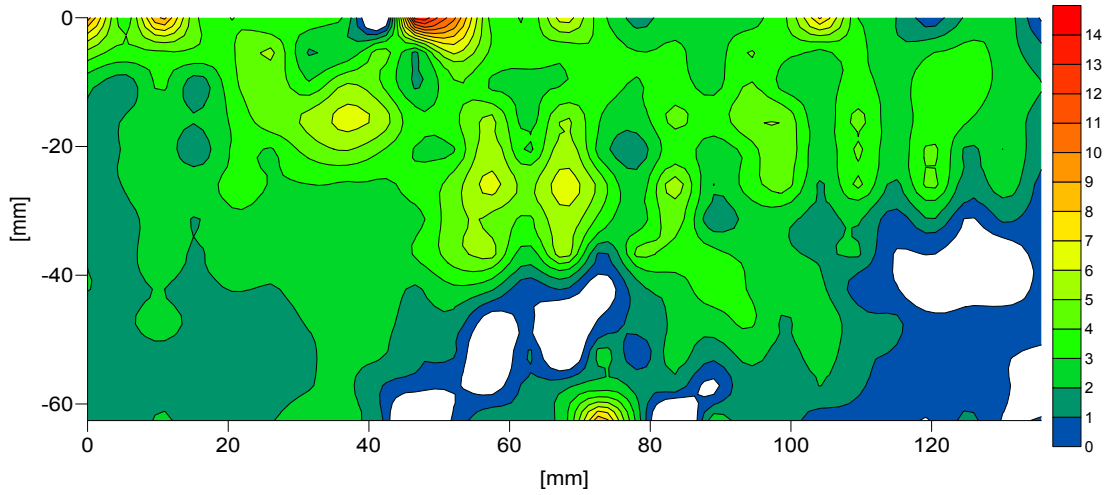


Figure 5.46: Consolidation across the width of silo above the hopper. [mm]

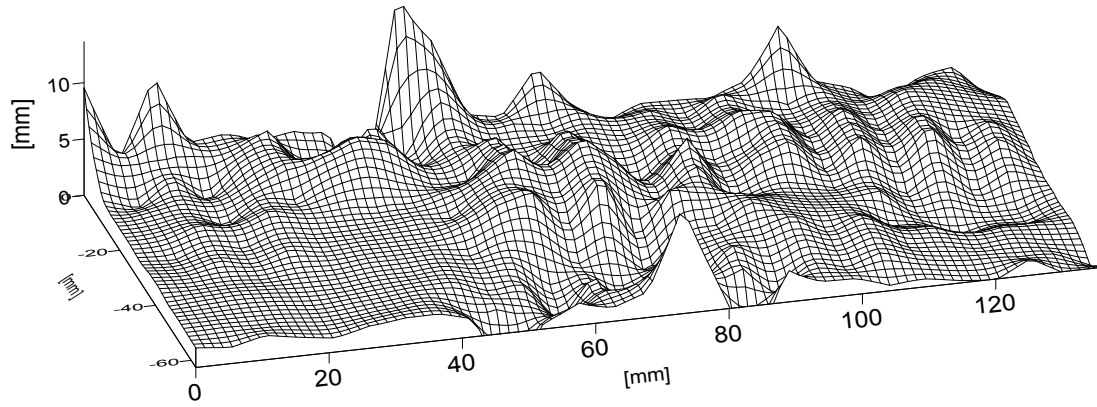


Figure 5.47: Consolidation across the width of silo above the hopper. [mm]

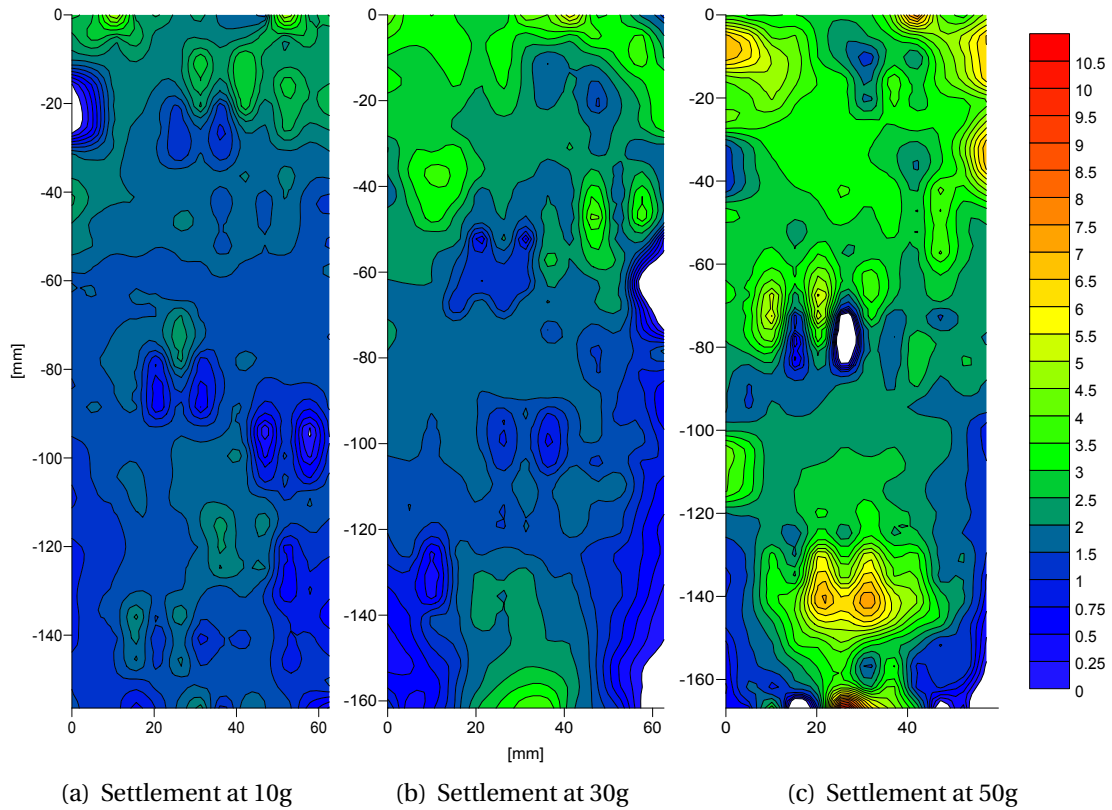
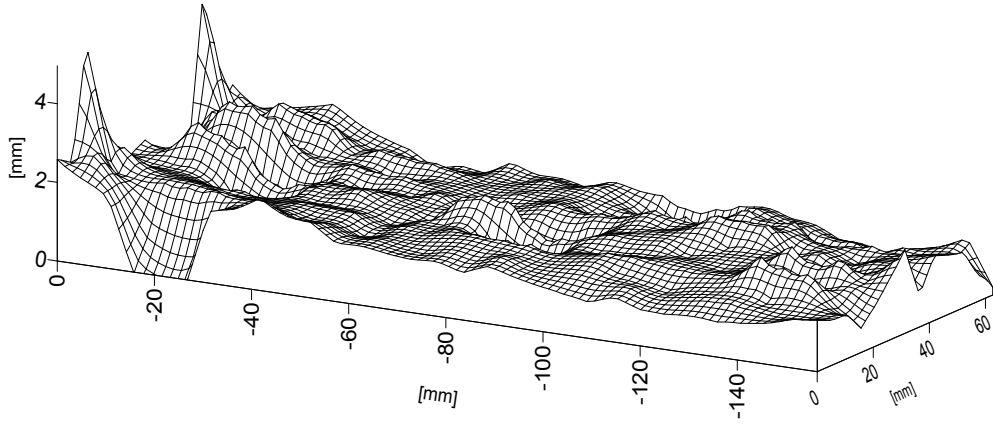


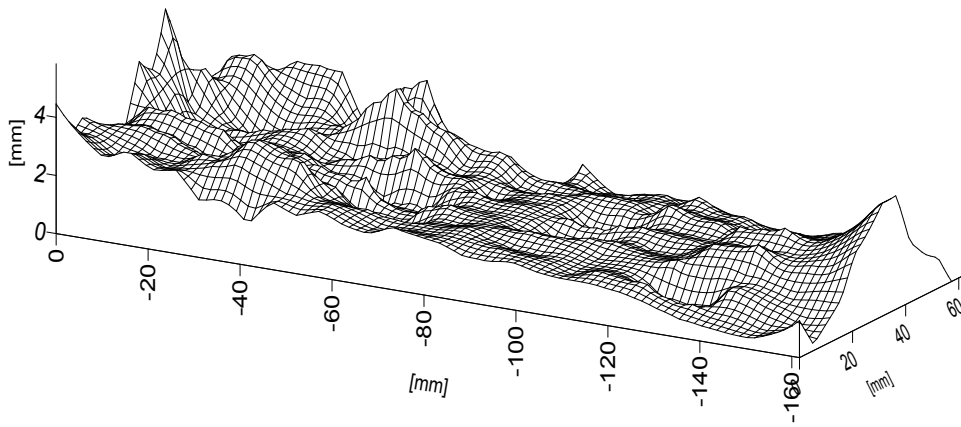
Figure 5.48: Contour maps of consolidation in vertical direction. [mm]

## 5. EXPERIMENTAL RESULTS

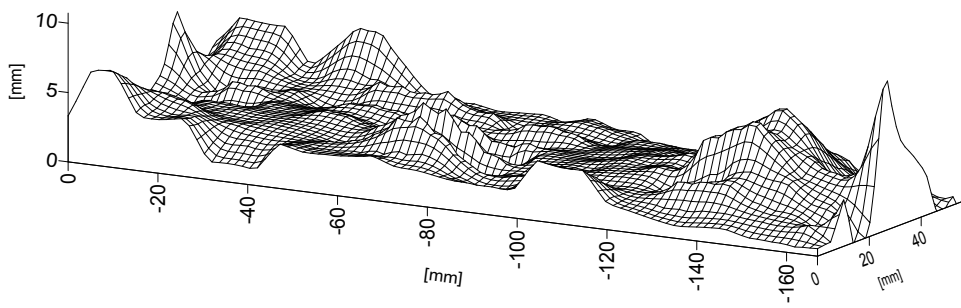
---



(a) Settlement at 10g



(b) Settlement at 30g



(c) Settlement at 50g

Figure 5.49: Displacement in vertical direction. [mm]

---

## Conclusions

Settlement across the width of the silo above the hopper was assessed. Figure 5.46 shows that there is more settlement towards the centre of the silo than at the edges. This is because of the influence of the hopper beneath the region being investigated. There is a greater depth of material beneath the region in the centre than at the edge, and therefore the total settlement is greater towards the centre than the side.

The results in Figures 5.48 and 5.12 show that the material deformation is anisotropic but that the average settlement at a given depth is linearly proportional to the depth. Settlement is also proportional to the increase in self-weight. The change in density as a result of this settlement behaviour is an equal increase in density throughout the silo. In figure 5.45 the density before discharge is plotted against centrifugal acceleration.

Figure 5.12 shows that at 10g, 30g and 50g, the settlement is approximately linearly proportional to the height above the bottom of the silo. The results also show that the material does not deform homogeneously. The increase in density resulting from this settlement is plotted against factor of gravity  $N$  in figure 5.45. The results show that from 1g to 50g there is a 2.3% increase in density and that density increases linearly at gravities greater than about 10g.

### 5.13 Normal wall pressures before and during discharge

#### 5.13.1 Introduction

The prediction of the pressures exerted on a silo wall by stored material is an important part of the structural design of a silo. Vertical pressure distributions are generally well predicted using the Janssen equation (Equation 2.13), but observing detailed circumferential and vertical pressure variations simultaneously is challenging due to instrumentation limitations.

Force sensing resistors (FSRs) are an emerging pressure measurement technology and may offer new pressure measurement opportunities in silo structures. In this chapter their performance is assessed. In the silo centrifuge model, a pressure pad is attached to the left and right silo wall and pressure readings are recorded throughout a test. Pressure readings begin being recorded as the centrifuge accelerates from 1g to the target acceleration and continue until discharge is complete.

Force sensing resistors are already used in medical and industrial applications including Podiatrics and automobile manufacture. The pressure pads are made from arrays of FSR's. The pads used in this investigation are 10cm wide, 30cm tall and approximately 2mm thick. They contain an array of 12 × 20 individual sensors of size 8.3mm × 5mm. Technical data is taken from a technical overview produced by Electrade GmbH and supplied by Medilogic GmbH [Electronics, 1993].

Figure 5.50 shows a typical FSR construction. Two polymer films are prepared and on one film a sheet of interdigitating electrodes is deposited. Finger-width and spacing is typically approximately 0.4mm. The other polymer film is covered in a semi-conductive sheet and the sheets are faced together so that the conducting fingers are shunted by the conducting polymer. The resistance of the conducting polymer is inversely proportional to the force applied to it. When no force is applied to the polymer, the resistance is approximately 1MΩ. As force increases, the resistance reduces following an inverse power law. Figure 5.51 shows a typical plot of resistance versus force.

---

The sensors are of interest because they measure pressure distribution with a high resolution equal to the size of the individual FSRs. They are also relatively inexpensive, thin, durable and environmentally resistant. Although they are recommended for semi-quantitative measurements, their quantitative performance will be assessed. Figure 5.52 suggests that a high degree of repeatability can be expected.

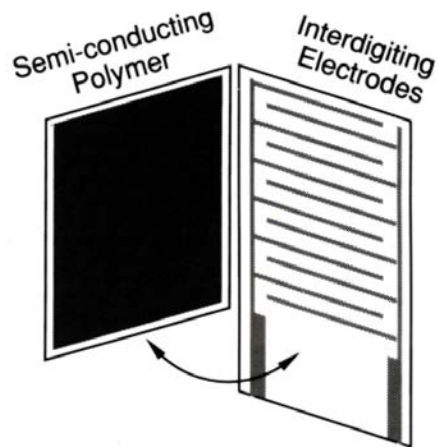


Figure 5.50: Typical FSR construction

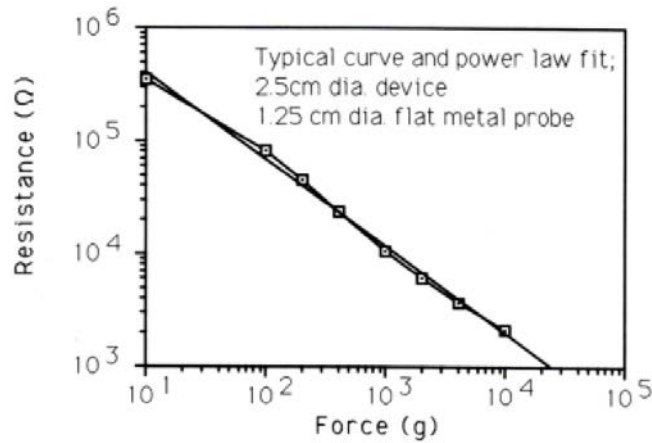


Figure 5.51: FSR force resistance characteristic trend

## 5. EXPERIMENTAL RESULTS

---

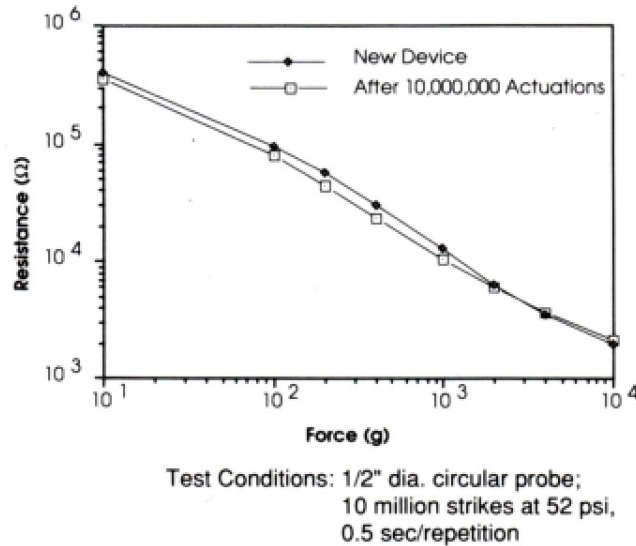


Figure 5.52: FSR longevity test

### 5.13.2 Sensor specification and calibration

The sensors used in this investigation are modified by the supplier (Medilogic GmbH) to increase their sensitivity and decrease their range from  $0 - 640kPa \pm 5\%FSO$  to  $0 - 60kPa \pm 15kPa$ . They are supplied with a data logger and PC software. The data logger is paired with the pressure pads and contains calibration data from tests conducted by the supplier. The data logger is connected to a laptop which uses purpose-built software to interpret and display the readings. In this way the pressure pads and data logger make a pressure measurement system.

The pressure pads response to pressures in the range of  $0-60 kPa$  is investigated by conducting calibration tests using hydrostatic pressure distributions adjusted by centrifugal acceleration. Centrifugal speeds are calculated to produce hydrostatic pressures at the bottom of the sensor in  $10kPa$  increments from  $10kPa - 60kPa$ . The pressure pads could not be completely sealed in a water tight covering and therefore the top of the pad is above the water surface. Thus only the bottom 16 rows of sensors are calibrated because the surface of the water was just above the 16<sup>th</sup> row. Close to the surface of the water the hydrostatic pressure is small and therefore lower pressures are applied than at the bottom of the sensor.

---

## Calibration method

1. Each pressure sensor is placed in a flexible plastic bag and the bag is secured to a rigid metal plate so that the sensor remains flat.
2. The assembly is placed into water at an angle of 31 degrees to the vertical so that the bottom of the sensor is 20.5cm beneath the water surface.
3. The assembly is put into the centrifuge.
4. The magnitude of the hydrostatic pressure is controlled by varying the angular acceleration of the centrifuge.
5. Six pressure states are applied to the pressure pad. These are labelled according to the pressure exerted on the bottom sensor row. Each pressure pad is tested 5 times and the average response to each pressure state is calculated. The expected reading is calculated by considering the water depth, the inclination of the pressure pad and the change in gravity at different radii and water depths.

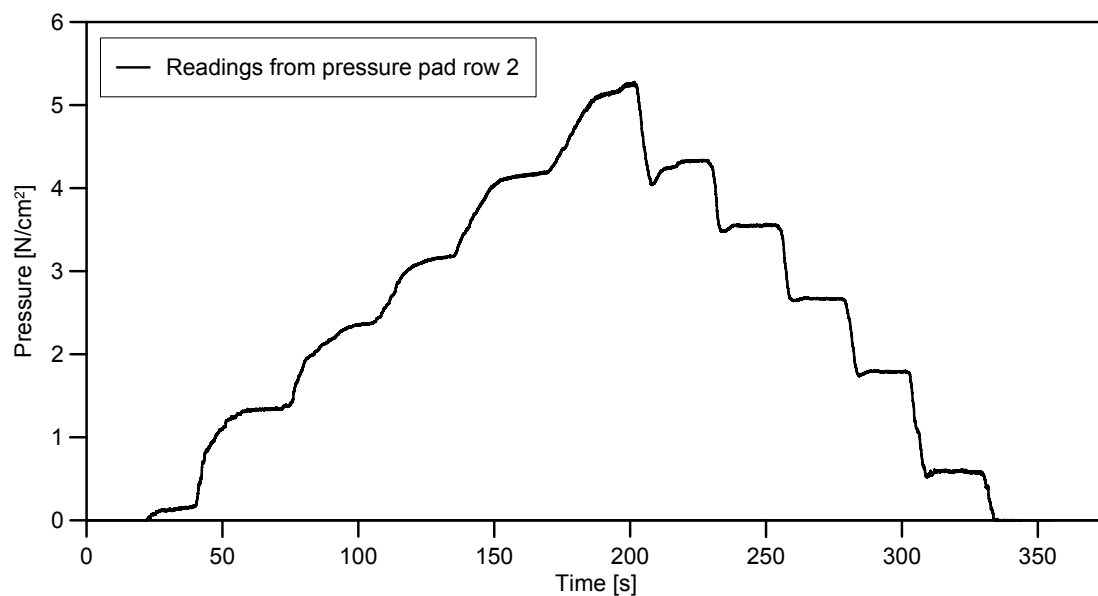


Figure 5.53: Typical data from a pressure pad calibration test

Figure 5.53 shows the pressures exerted on the bottom row of the sensor. It shows how the pressure varied as the centrifuge velocity increased and decreased.

## 5. EXPERIMENTAL RESULTS

Calibration curves are calculated by comparing the output pressure to the applied pressure.  $P_E$  is a function of the sensors distance below the water surface, its radius of rotation, the speed of the centrifuge and the density of water.

$$C_f = \frac{P_E}{P_O} \quad (5.4)$$

where  $C_f$  is the calibration factor  $P_E$  is the expected pressure and  $P_O$  is the output pressure.

### Pressure pad calibration curves

Figures 5.54 and 5.55 show a clear and similar power trend. The pressure pads are generally accurate at pressures above  $10\text{kPa}$ . Below  $10\text{kPa}$  the accuracy of the sensors quickly decreases. A power law trend based on the calibration results but omitting outliers is shown.  $R^2$  values of 0.90 and 0.79 are obtained.

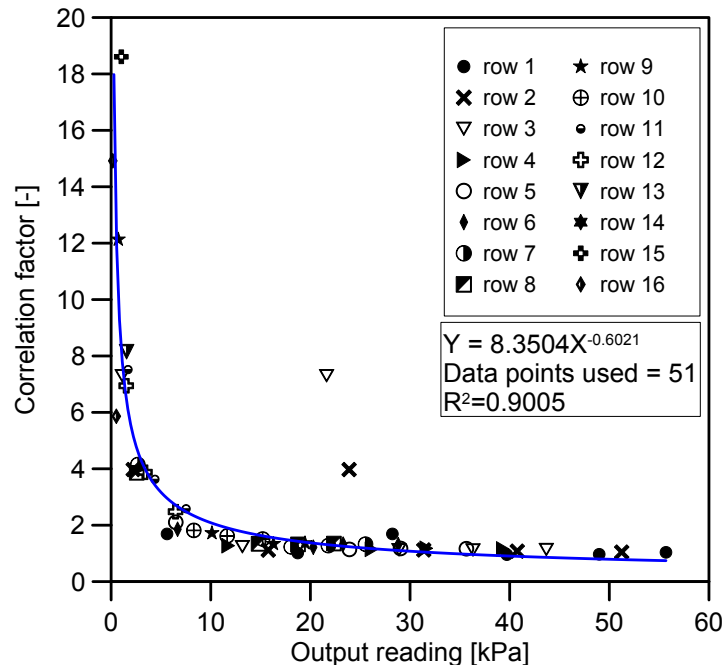


Figure 5.54: Calibration curve for blue pressure sensor using averaged data

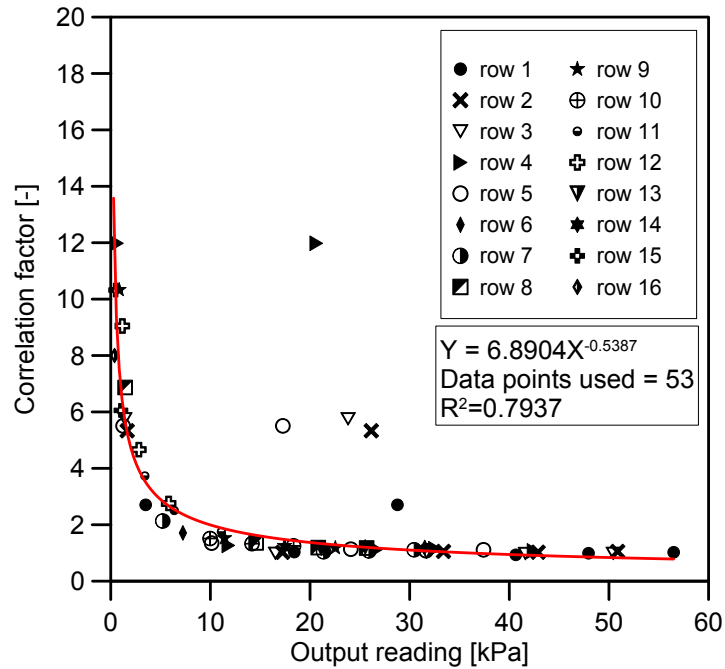


Figure 5.55: Calibration curve for red pressure sensor using averaged data

### 5.13.3 Silo centrifuge tests with pressure sensors

The coarse sand (Material M2) was used in tests to observe the normal wall pressures in 3 model silos before and during discharge. The tests were carried out at 50g in order to produce wall pressures large enough to be measured by the pressure pads. Pressure measurements were recorded at a frequency of 125Hz. The average pressure for the middle 50% of each row of the sensors is considered, this corresponds to the 6 FSRs in the center of each row and ignores the reading from the 3 FSR's at either end of each row. Only the middle 50% of the sensor is used in order to ignore wall effects. The pressure pad row numbering system ascends with height, row 1 is at the bottom and row 10 is furthest from the outlet. The center of each pressure pad row is 15mm from the centre of adjacent rows.

### Wall pressures for the silo centrifuge model with flat bottom

Figure 5.56 shows the normal wall pressures for the bottom 10 rows of the pressure pad throughout a successful test with the flat-bottomed silo centrifuge model at 50g.

The results show that during the acceleration phase of the experiment ( $t = 22s$  to  $t = 60s$ ) the normal wall pressures do not increase at the same rate relative to each other. For example pressure pad row 4 records a smaller pressure than pressure pad row 2 until  $t = 39$  seconds and afterwards it records a greater pressure.

Once the centrifuge has been accelerated to the target velocity ( $t=66$  seconds) the wall pressure readings are almost constant and there are small variations in the readings between  $t = 60s - t = 87s$  during which time the angular velocity of the centrifuge is constant. The cause of the pressure reading fluctuations is unclear. If they are caused by granular reorganisation resulting from the recently increased stress state then the magnitude of the fluctuations would decay with time. However, this is not observed.

Figure 5.57 shows a subsection of the results in 5.56 focussing on the time period around discharge initiation. It can be seen that at  $t = 87.5s$ , silo discharge begins and the wall pressures transition to different values by  $t = 88.3s$ . The time taken for the wall pressures to adjust as a result of the silo outlet being opened is  $t_t = 0.8s$ . At the onset of discharge, pressure pad rows 3, 4 and 5 give an increased pressure reading. Pressure pad rows 7, 8, 9 and 10 record pressure decreases. Pressure pad rows 1, 2 and 6 record a constant pressure during the time-period around discharge initiation.

Pressure pad rows 1 and 2 gave unusual pressure readings throughout the duration of the test, pressure pad row 1 remained very close to 0 at all times. Readings from pressure pad row 2 did not decrease below  $\approx 14kPa$  once the silo was opened. The cause of these readings is unclear. Pressure pad row 6 behaved as expected before and after discharge was initiated. Therefore, the unobserved change in pressure at the beginning of discharge is not attributed to the same cause as the readings from pressure pad rows 1 and 2.

Figure 5.58 shows the vertical normal wall pressure distribution in the model silo with flat bottom at 3 times;  $t = 87s$ ,  $t = 87.7s$  and  $t = 88.5s$ . These times are chosen

to show the pressure states before discharge, at the onset of discharge, and during discharge. The results show that the pressure distribution does not closely match wall pressures predicted using Janssen's wall pressure theory. Below  $z = -0.08m$  the normal wall pressures are consistently lower than those predicted using Janssens silo wall pressure theory. Below a depth of  $z = -0.12m$  the normal wall pressures are approximately proportional to those predicted. However at depths greater than  $z = -0.24m$  the normal wall pressure quickly decreases. At shallow depths the normal wall pressure spikes from approximately  $0kPa$  at  $z = 0m$  and  $z = 0.08m$  to  $20kPa$  at  $z = 0.06m$ . The cause of these is unclear.

At depths between  $z=-0.12$  and  $z=-0.26$  the pressure distribution can be seen to change at the onset of discharge. Before discharge a distribution similar to that predicted by Janssen for filling pressures is observed. During discharge a more linear distribution is observed, as is expected during emptying.

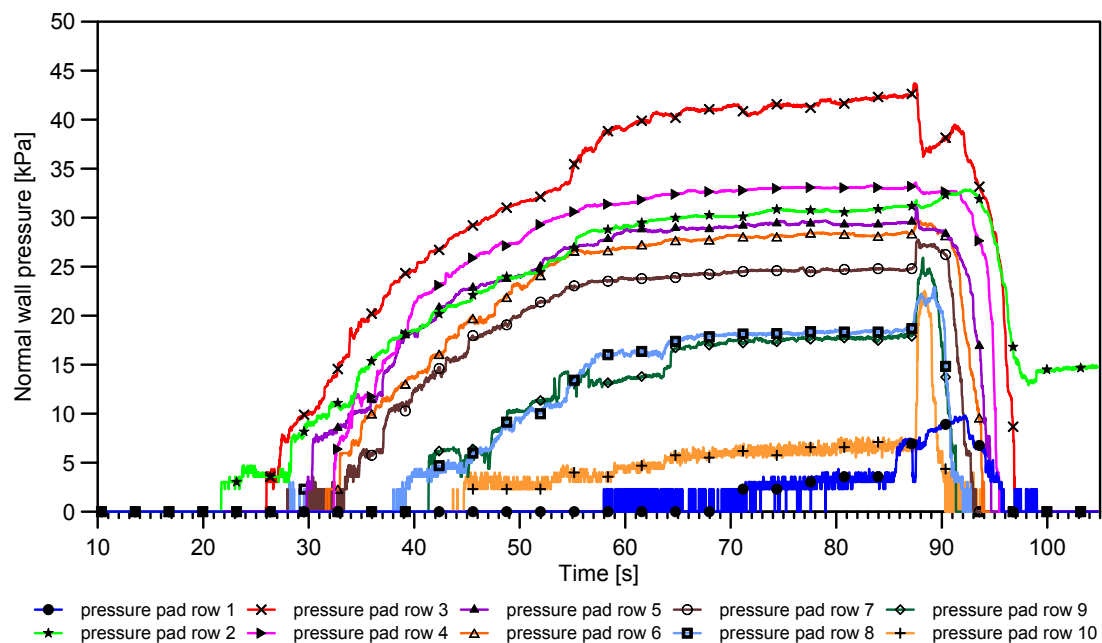


Figure 5.56: Wall pressures during test with coarse sand in flat bottom silo, 50g

## 5. EXPERIMENTAL RESULTS

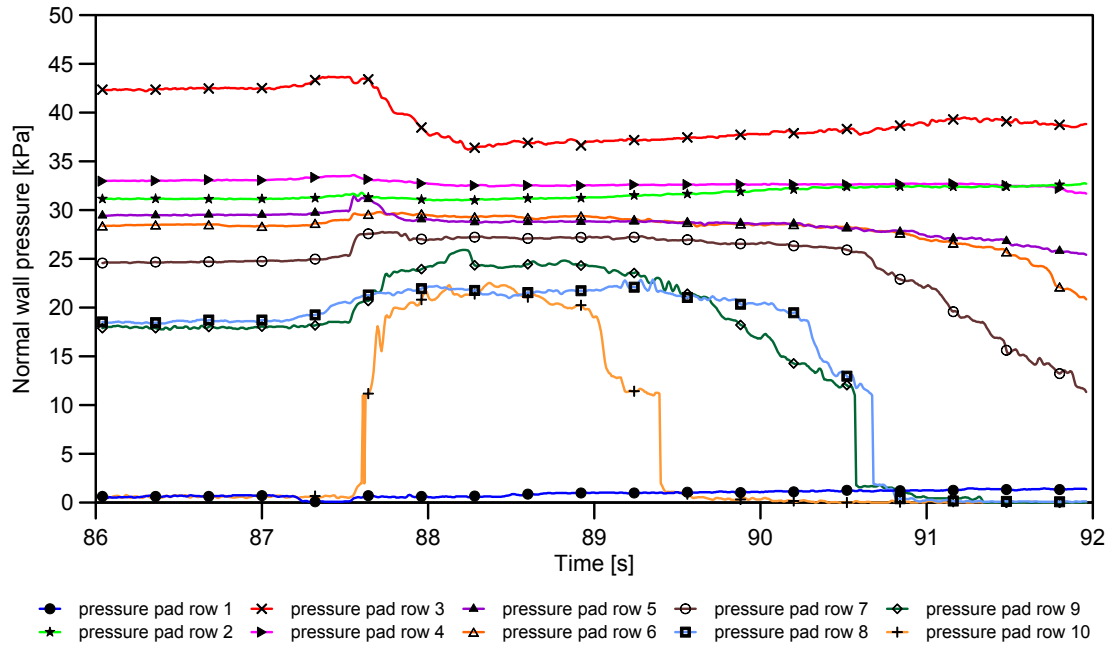


Figure 5.57: Wall pressures during test with coarse sand in flat bottom silo, 50g

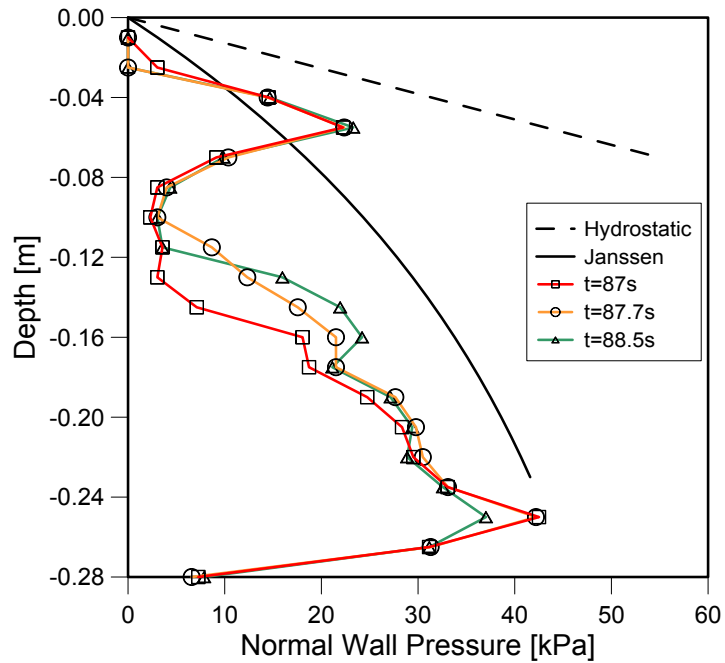


Figure 5.58: Normal wall pressures at 3 times. LHS, coarse sand in flat bottom silo, 50g

---

### Wall pressures in the model silo with 60 degree hopper

In the silo with 60 degree hopper, the change in normal wall pressures at the onset of silo discharge is less pronounced than in the silo with flat bottom. (Figures 5.59 and 5.60). The largest reduction in pressure is seen for pressure pad row 2, which reduces from  $49kPa$  to  $39kPa$  in approximately 0.9 seconds. Pressure pad rows 1, 3 4 and 5 record smaller decreases in wall pressure at the onset of discharge. Pressure pad row 6 records a small decrease in pressure for approximately 0.4s before increasing again. Pressure pad rows 9 and 10 record an increase in pressure at the onset of discharge. Pressure pad rows 7 and 8 record the maximum possible pressure of  $60kPa$  throughout the test so it is possible that the pressure did reduce at the onset of discharge but remained above  $60kPa$ .

The transition time ( $t_t$ ) required for the pressures in the silo to change from the filled state to the discharging state are the same for the flat-bottomed silo and the silo with 60 degree silo ( $t_t \approx 0.9s$ ).

Figure 5.61 shows that the wall pressure distribution before discharge is similar to that predicted using Janssen wall pressure theory. A small reduction in wall pressure in the vertical section of the silo is observed at the onset of discharge and a small increase in pressures is recorded in the hopper during discharge. The normal hopper wall pressures are lower than those predicted because the maximum pressure pad reading is  $60kPa$ . The increase in normal wall pressure in the region of the hopper begins at a shallower depth than that predicted using the theories of Walker and Janssen. This may be due to their assumption of mass flow during discharge. At depths higher than  $z = -0.4m$  the pressure readings are 0. This suggests that the pressure pads are not able to reliably measure pressures smaller than approx  $10kPa$ .

There is a very good agreement between observed and predicted normal silo wall pressures before discharge for the silo with 60 degree hopper at depths below  $z = -0.4m$ . It is unclear why the qualitative agreement between expected and observed results varies to such a great extent between different silo models.

## 5. EXPERIMENTAL RESULTS

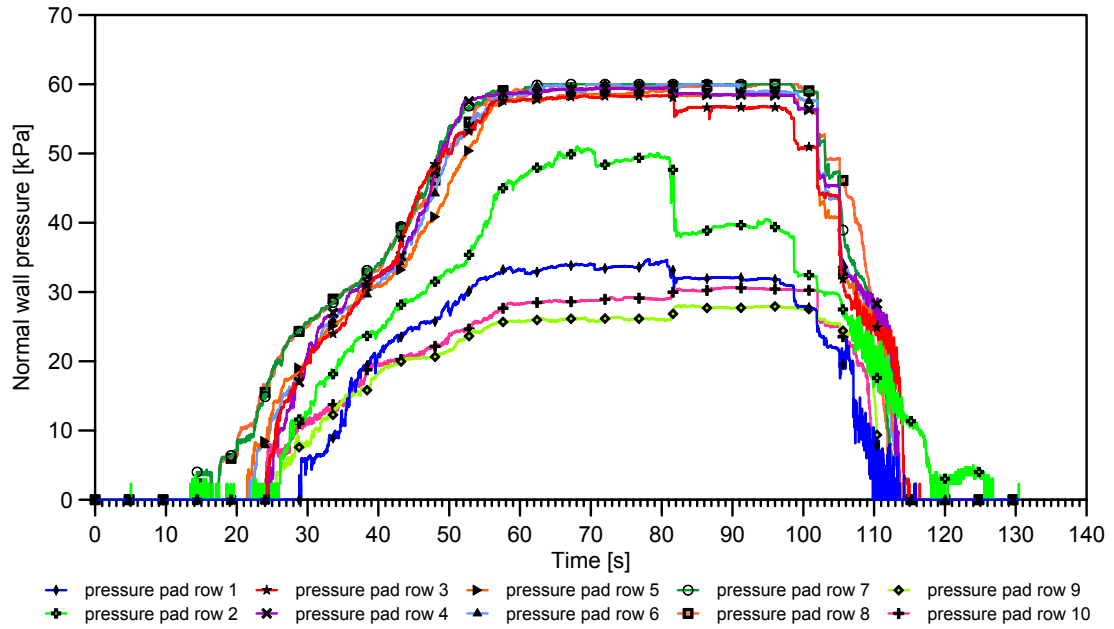


Figure 5.59: Silo wall pressures, coarse sand in silo with 60° hopper at 50g

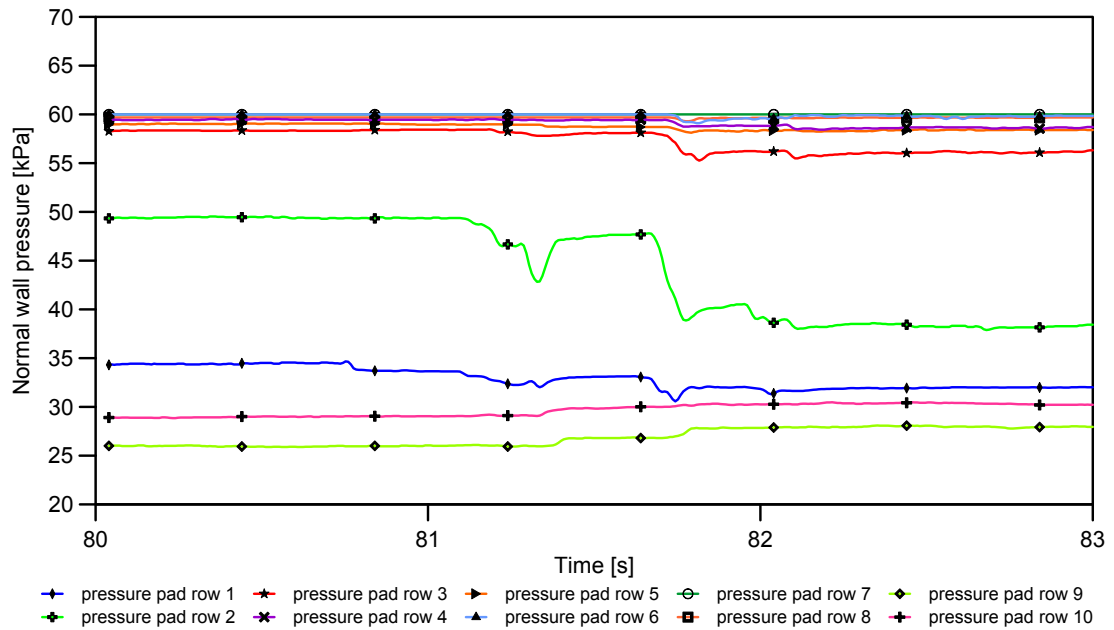


Figure 5.60: Silo wall pressures, coarse sand in silo with 60° hopper at 50g

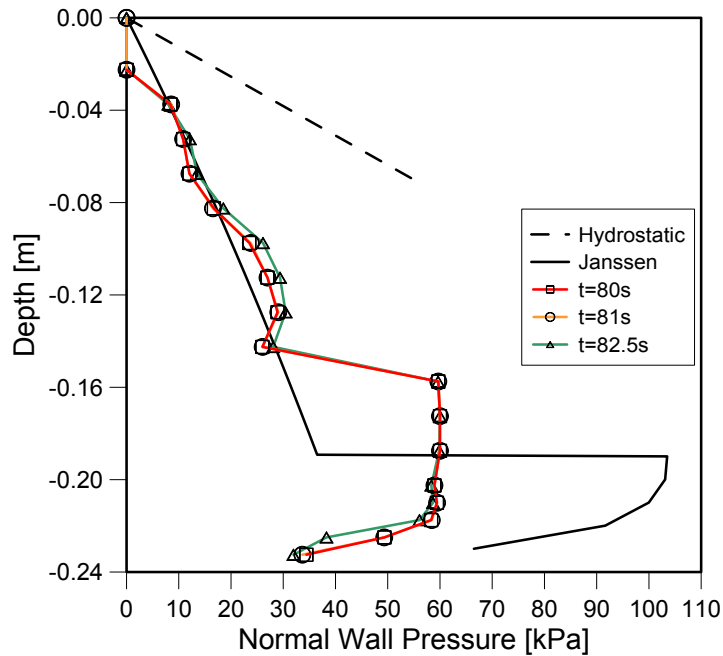


Figure 5.61: Normal wall pressures at 3 times. LHS, coarse sand in silo with 60 degree hopper at 50g

### Wall pressures in the model silo with 30 degree hopper

In the model silo with 30 degree hopper, the wall pressure response to the onset of discharge is different to that observed in either the model silo with flat bottom or with 60 degree hopper.

Pressure pad rows 1, 2 and 4 record a decrease in pressure at the onset of discharge. Pressure pad rows 5, 9 and 10 record an increase in pressure at the onset of discharge. The remaining pressure pad rows record approximately constant pressures at the onset of discharge and then decrease as material in the model silo discharges.

The transition time required for the stress state to change from filling to discharging is unclear and a transition time of  $t_t \approx 0.25s$  is suggested. The short total discharge time of approximately 1.75s makes it harder to observe a change resulting only from the onset of discharge. At the onset of discharge, the wall pressures between  $z = -0.04$  and  $z = -0.20$  decrease and at depths below  $z = -0.20$  they increase. The

## 5. EXPERIMENTAL RESULTS

maximum output pressure of  $60\text{ kPa}$  is recorded at  $z < -0.20\text{ m}$ . Once the stress state has changed from filled to discharging, the pressures at depths shallower than  $z = -0.16\text{ m}$  become 0. This is the largest reduction in stress due to discharge that was observed in any of the model silos and is probably caused by granular flow against the pressure pads.

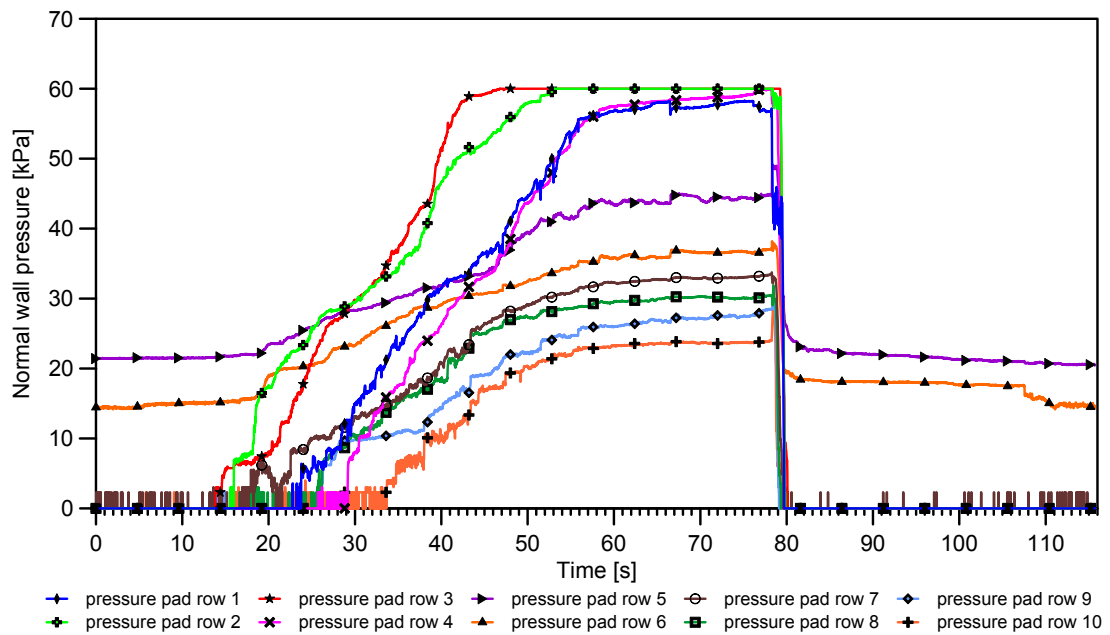


Figure 5.62: Silo wall pressures, coarse sand in silo with  $30^\circ$  hopper at  $50\text{ g}$

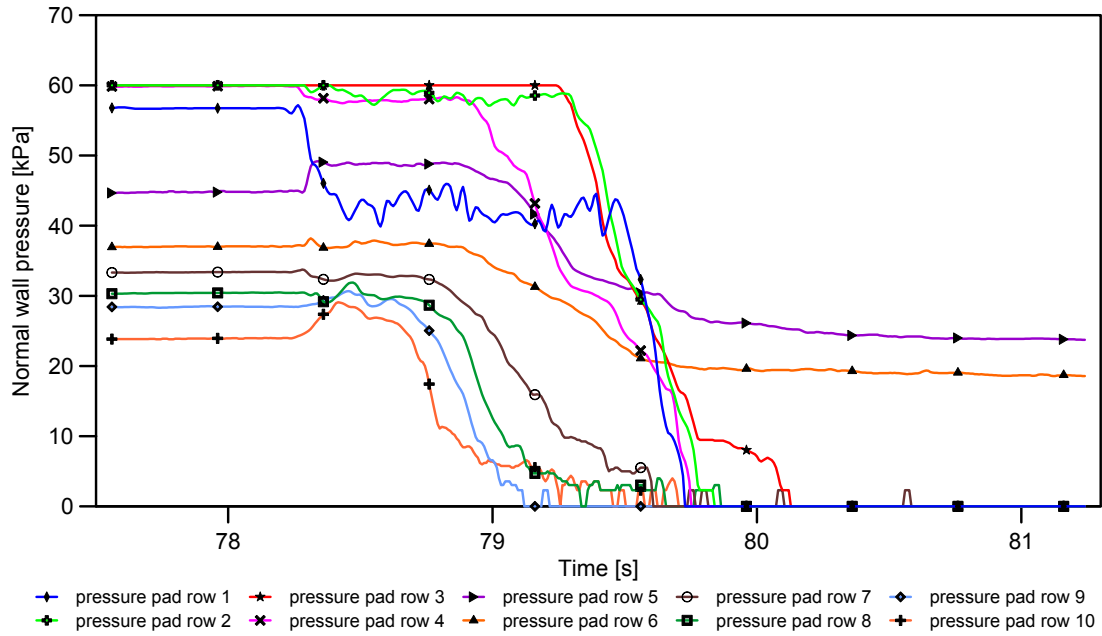


Figure 5.63: Silo wall pressures, coarse sand in silo with 30° hopper at 50g

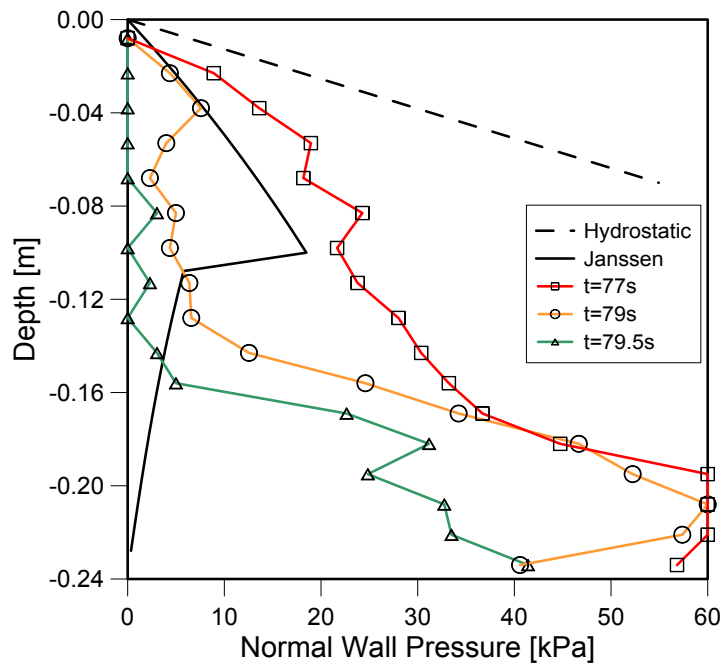


Figure 5.64: Normal wall pressures at 3 times. LHS, coarse sand in silo with 30 degree hopper at 50g

### 5.13.4 Conclusions

The pressure pads gave qualitative results for all three model silos and showed varying degrees of agreement with predictions based on the wall pressure theories of Janssen and Walker. The high frequency of readings (125Hz) allowed the transition of wall pressures from filling to discharge conditions to be assessed. The influence of the shear stress has not been quantified but is expected to be influencing the results. This is because the pressure pads cannot distinguish between normal and shear forces and only measure the reduction in resistivity of the semi conducting polymer as a result of the total pressure applied to it.

Different pressures are observed during filling and discharge for each silo geometry. In the silo with flat bottom a qualitative agreement with the Janssen wall pressure theory was observed between  $z = -0.12m$  and  $z = -0.24m$ . In this zone the pressure distribution changed during discharge towards the expected linear distribution, although the difference is small.

In the silo with 60 degree hopper, the wall pressure distribution is very similar to that predicted using Janssen's wall pressure theory at depths greater than  $-0.06m$ . The increase in pressure above the transition from hopper to vertical section is explained by considering that funnel flow was produced and not mass flow, which the wall pressure theories of Janssen (vertical section) and Walker (converging hopper section) assume. There is a small reduction in pressure during discharge but no appreciable change in pressure distribution. This is also perhaps due to the funnel flow condition. In the hopper there is an increase in wall pressures during discharge which is expected.

The model silo with 30 degree hopper had the shortest vertical section of the three model silos, because of the steep hopper. It was therefore the most squat silo, with a height to width ratio for the vertical section of only 0.8. This is expected to influence the results. An approximately linear wall pressure increase with depth is observed before discharge. During discharge the normal wall pressures reduce to approximately 0 in the vertical section and in the upper third of the hopper. The normal wall pressures immediately after discharge ( $t = 79s$ ) show a consistent transition from the

---

filling to discharge pressure state at all depths.

In the silo with 30 degree hopper, the hopper is classed as steep and mass flow is observed at the onset of discharge (before returning to funnel flow once the depth of fill reduces). In the silo with 30 degree hopper, the grains against the pressure pads will move once discharge begins and this would produce the observed pressure reduction. A possible reason for pressures greater than 0 below  $z = -0.16$  is the beginning of arching effects arising from proximity to the silo outlet.

## 5. EXPERIMENTAL RESULTS

---

# Chapter 6

## Discrete element model of silo discharge

### 6.1 Model design

A numerical model was designed to investigate silo discharge using the Discrete Element Method (DEM). The numerical model was designed to be as similar as possible to the physical model in order to minimise sources of error. Both physical and numerical silos were filled by pouring material from the top and center of the silo. In order to mimic the physical model, the gravity was  $9.81\text{m/s}^2$  during filling and was increased after filling had completed and particle velocities were very close to 0. When the gravity was increased the model was cycled in order to approach equilibrium again before discharge was initiated. As a result of this, the velocities of the particles at the beginning of discharge were very close to 0.

Outputs from the numerical and physical silo discharge tests are compared by designing the numerical model so that output data is of the same type as data output from the physical model. Results from the numerical model include mass flow data and flow pattern data, as well as additional quantities than cannot be measured in the physical silo model such as porosity.

### 6.1.1 Dimensions

The numerical silo model represents a silo of the same width and height as the physical silo. The DEM model takes advantage of the planar design of the physical model by using periodic boundaries. The distance between the periodic boundaries is 2.95 times greater than the largest particle diameter. Using periodic boundaries removes the need to either model every particle in the physical model, which is not practical because of the computational resources it would require, or greatly increase the size of the particles. Even with these design features, the diameter of the particles in the numerical model needed to be increased to twice the diameter of the physical material, in order to reduce the number of particles in the model.

### 6.1.2 Parameters

The particles are spherical, with a linear size-distribution corresponding to the central region of the PSD (Particle Size Distribution) of material M2. Figure 6.1 shows that the coarse sand used is poorly graded and approximately 90% by mass of grains are within the region between 0.7mm and 1.02mm diameter. The particle size distribution in the numerical model was chosen to represent this range.

Table 6.1: Wall parameters

Parameter	Value
Wall normal stiffness [N/mm]	1e8
Wall shear stiffness [N/mm]	1e8
Wall friction coefficient [-]	0.4
Outlet width [mm]	20
Periodic thickness [mm]	5.95

Table 6.2: Ball parameters

Parameter	Value
Particle size [mm]	1.40 - 2.00
Material density [kg/m <sup>3</sup> ]	2655
Ball normal stiffness [N/mm]	1e7
Ball shear stiffness [N/mm]	1e7
Ball friction coefficient [-]	2.2

Table 6.3: Other parameters

Parameter	Value
Time step	$0.5dt_{crit}$
Results output frequency	0.05 seconds

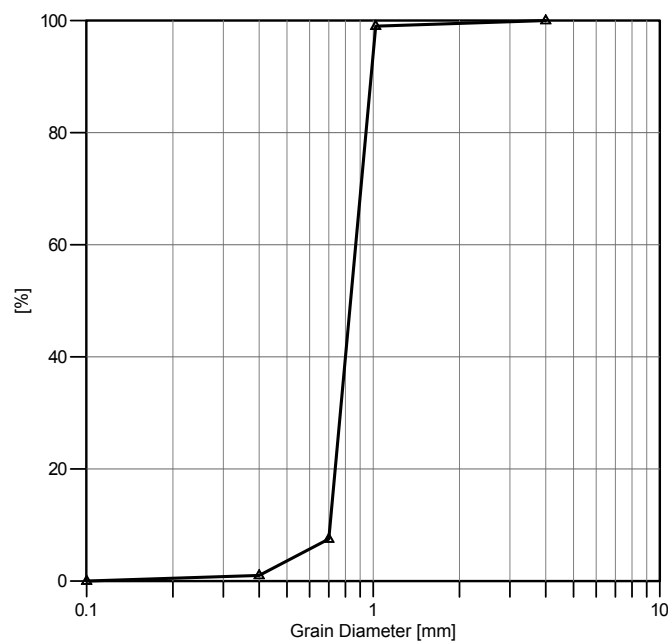


Figure 6.1: Particle size distribution of material M2, DIN 1164/58 Norm Sand II Klein (1998)

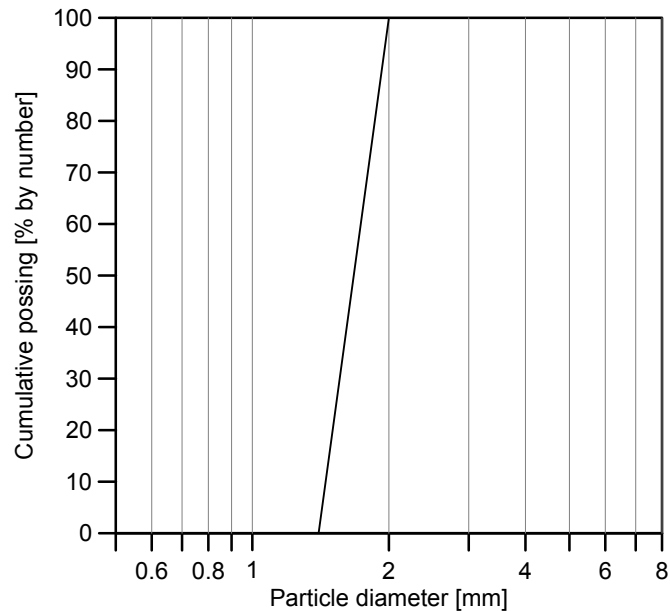


Figure 6.2: Particle size distribution in numerical model

### 6.1.3 Filling

The silo was filled by generating particles in a region at the top of the silo. The width of the region was half of the silo width, centred about the outlet. Particles were generated in the region and then fell under the action of gravity. After a time period in which all the particles had fallen out of the region and more particles were then generated. This was repeated until the silo was full.

This method was chosen because it is similar to the physical silo centrifuge model and other methods would generate a bulk material with different density and porosity properties.

### 6.1.4 Discharge

The discharge was recorded by obtaining ball data every 0.05 seconds. The number of balls in the silo at each output time is recorded and discharge rate is calculated from this data. Data output included the coordinates of the ball centres and ball

---

velocity components. The data was exported using an array in PFC and writing the array in a .CSV file. This file was converted to a .xls file using a visual basic macro as part of Microsoft Office. The .xls file was finally imported to MATLAB where the data could be efficiently analysed.

## **6.2 Calibration process for numerical model**

The numerical material was designed to have the same angle of internal friction as the physical material, as well as other properties including density and porosity. This was achieved by varying the material properties and running a series of numerical triaxial tests. The particle stiffness and friction properties were changed until the bulk characteristic behaviour of the numerical material was similar to the physical material.

Two criteria needed to be met:

1. A decrease in the angle of internal friction with increasing confining pressure, similar to that observed in the physical triaxial tests.
2. An angle of internal friction close to 34 degrees at high confining pressures.

## 6. DISCRETE ELEMENT MODEL OF SILO DISCHARGE

---

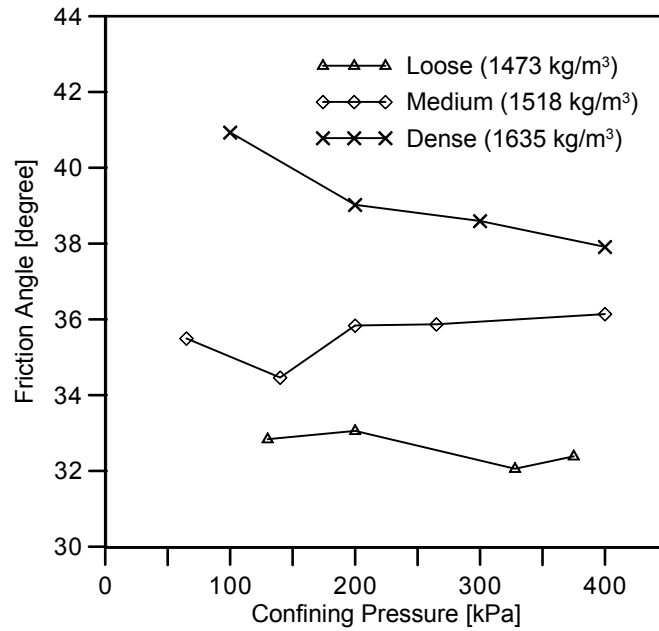


Figure 6.3: Variation of friction angle with confining pressure for physical samples of different initial density

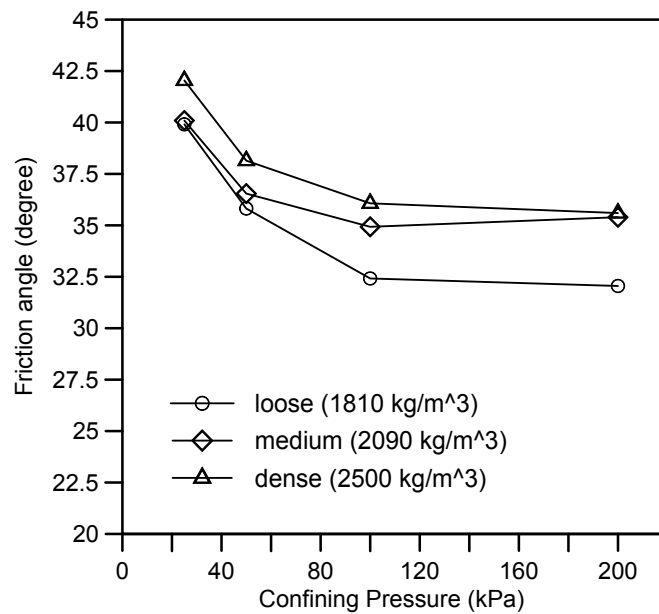


Figure 6.4: Variation of friction angle with confining pressure for DEM samples of different initial density

---

Figures 6.4 and 6.3 show that the DEM model produces the correct trend where friction angle reduces with increasing confining pressure ( $\sigma_3$ ). As confining pressure increases, the angle of internal friction approaches a constant value that is close to 34°.

The effects of initial sample density are also similar to what is observed in physical triaxial tests, where lower initial density results in a lower angle of internal friction and higher initial density increases the angle of internal friction. In the DEM model the particles are spherical but in the physical model the sand grains are angular. This is one of the fundamental differences between the two models and the effects of this difference can be seen in the different bulk density values for the two models. Because the numerical model material is spherical, the packing naturally becomes more efficient than with angular material in the physical model. Additionally, the angularity of the physical material increases the bulk frictional resistance in addition to the material roughness. This cannot be considered with spherical particles and therefore the coefficient of friction of the numerical material must be increased to compensate for the geometric regularity and smoothness.

## 6.3 Density increases at higher gravities

### Method

The increase in density as a result of increase in gravity was calculated. In order to achieve a representative value a large region was chosen in order to calculate bulk density. Figure 6.5 shows the region of the silo that was used for the silo with 30 degree hopper. The dimensions and position of the region were chosen to maximise the height of the region whilst making the region rectangular. The width of the region from -40mm to +40mm was kept the same for all silo geometries, whilst the bottom and top dimension were varied to maximise the height of the window whilst staying centred for each type of silo. In this way, the width of the region was always 80mm, and the height of the region was always as great as it could be, whilst maintaining that no part of the region was outside the boundary of the bulk material and the region was centred vertically and horizontally.

The bulk density was calculated using a MATLAB script written for the analysis. During the DEM simulation, results were output 20 times per simulated second as .CSV tables. These were converted to Excel files using a macro script and the number of balls within the region was counted. The average particle radius is known and therefore the average ball volume and therefore the total volume of balls in the region was calculated. In this way the bulk density was calculated.

### Results

The increase in gravity increases the density of the material. Figure 6.6 shows that the increase in density in both silos between 1g and 50g is approximately equal, but the results also show that the bulk density is different in each type of silo. The bulk density varies from approximately 1800kg/m<sup>3</sup> to 2100kg/m<sup>3</sup> depending on gravitational acceleration and silo geometry.

Whilst it is expected that an increase in gravity will result in an increase in the bulk density, the effect of silo geometry is not expected. The filling technique, including

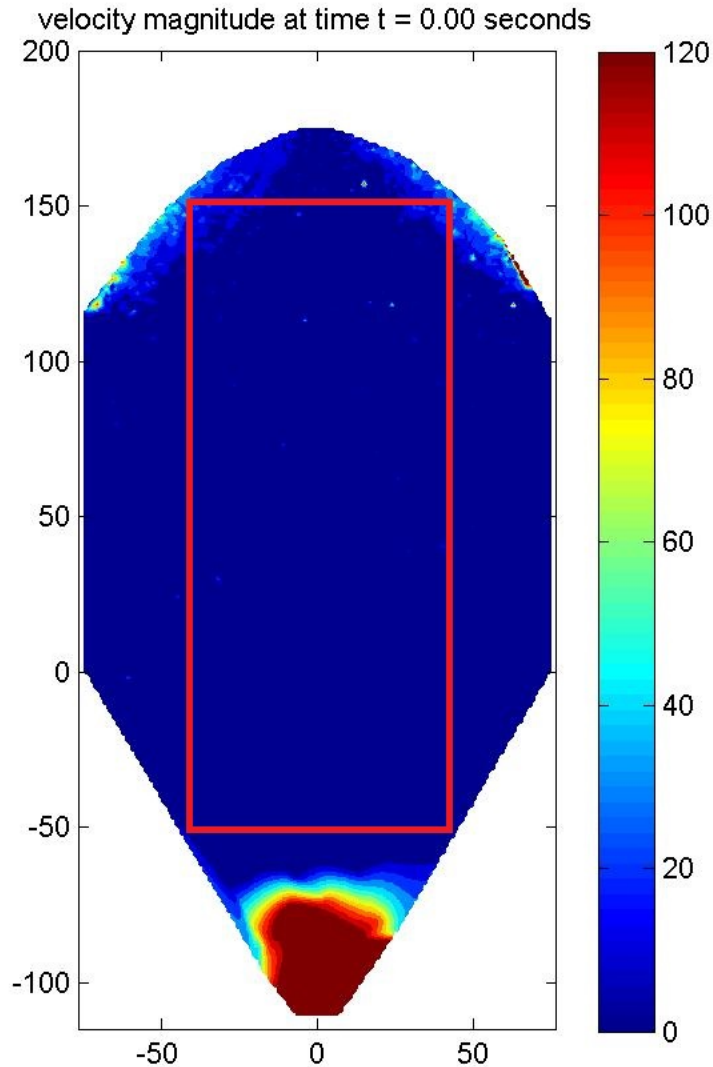


Figure 6.5: Region used to calculate bulk density in silo with 30 degree hopper

height and area, was the same in all simulations which makes the influence of silo geometry a surprising result.

## Conclusions

Figure 6.6 shows that for each silo, the increase in density from factors of gravity 1 to 50 is approximately 11%. This magnitude of the increase is approximately the same for both types of silo and therefore does not vary significantly with silo geometry. The

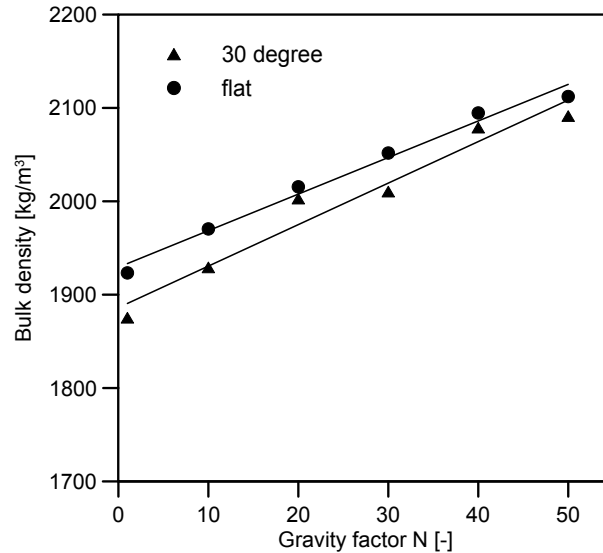


Figure 6.6: Bulk density of granular material in different silos at different factors of gravity

corresponding void ratios for these bulk densities is  $e_{1g} = 0.475$  and  $e_{50g} = 0.264$ .

An increase of 11% in the bulk density is much larger than the increase that was observed in the physical silo, where the increase in bulk density from a gravity of 1g to 50g was  $1490 \text{ kg/m}^3$  to  $1525 \text{ kg/m}^3$ , an increase of 2.3%.

Thus, the density increase in the DEM model is 4.8 times larger than the increase observed in the physical silo model. Two explanations of this could be the difference in the shape of the particles, and the stiffness model used in the DEM model. The particles in the numerical model are spherical, therefore the packing will naturally be more efficient than the packing of the angular sand particles in the physical model.

## 6.4 Mass flow rate

### Background

The mass flow rate of the discrete element model is evaluated. The particle diameter in the numerical model was required to be larger than the particles in the physical

---

silosilofluence model in order to decrease the number of particles. The outlet width was increased by the same factor in order that the ratio of outlet diameter to particle diameter is the same in both the numerical and physical models. The particle diameter in the numerical model is twice as large as the diameter of particles in the physical model.

The mass flow rate is influenced by more properties than are included in the Beverloo correlation. Due to this, a comparison of mass flow rate between two similar models is useful. However, it is also limited because it does not isolate individual factors for consideration and an analysis of which factors are most influencing the discharge rate is not possible.

## **Method**

The mass flow rate was calculated using a MATLAB script to analyse the .CSV files output during the DEM simulation. The flow rate was calculated by comparing the the number of balls in the silo between two points in time, and from there calculating the mass flow rate by considering the average mass of a ball, the number of balls, and the time difference between the two measurements.

## **Results**

The DEM model had a thickness of 5.5mm. The silofluence model had a thickness of 100mm. In order to compare the results, the DEM discharge rates will be increased by a factor of  $100/5.5$ , or 18.18. This conversion factor is used in the following results.

The mass flow rate was not steady as was expected. The mass flow rate tended to fluctuate greatly at the beginning of discharge and then fluctuate with smaller oscillations about an average value after an initial period. The mean value of all data points is reported. Excluding values in the first second of discharge made no significant difference to this mean. Figures 6.7 and 6.8 show the discharge rate through time for the silo with flat bottom and silo with 30 degree hopper respectively.

## 6. DISCRETE ELEMENT MODEL OF SILO DISCHARGE

---

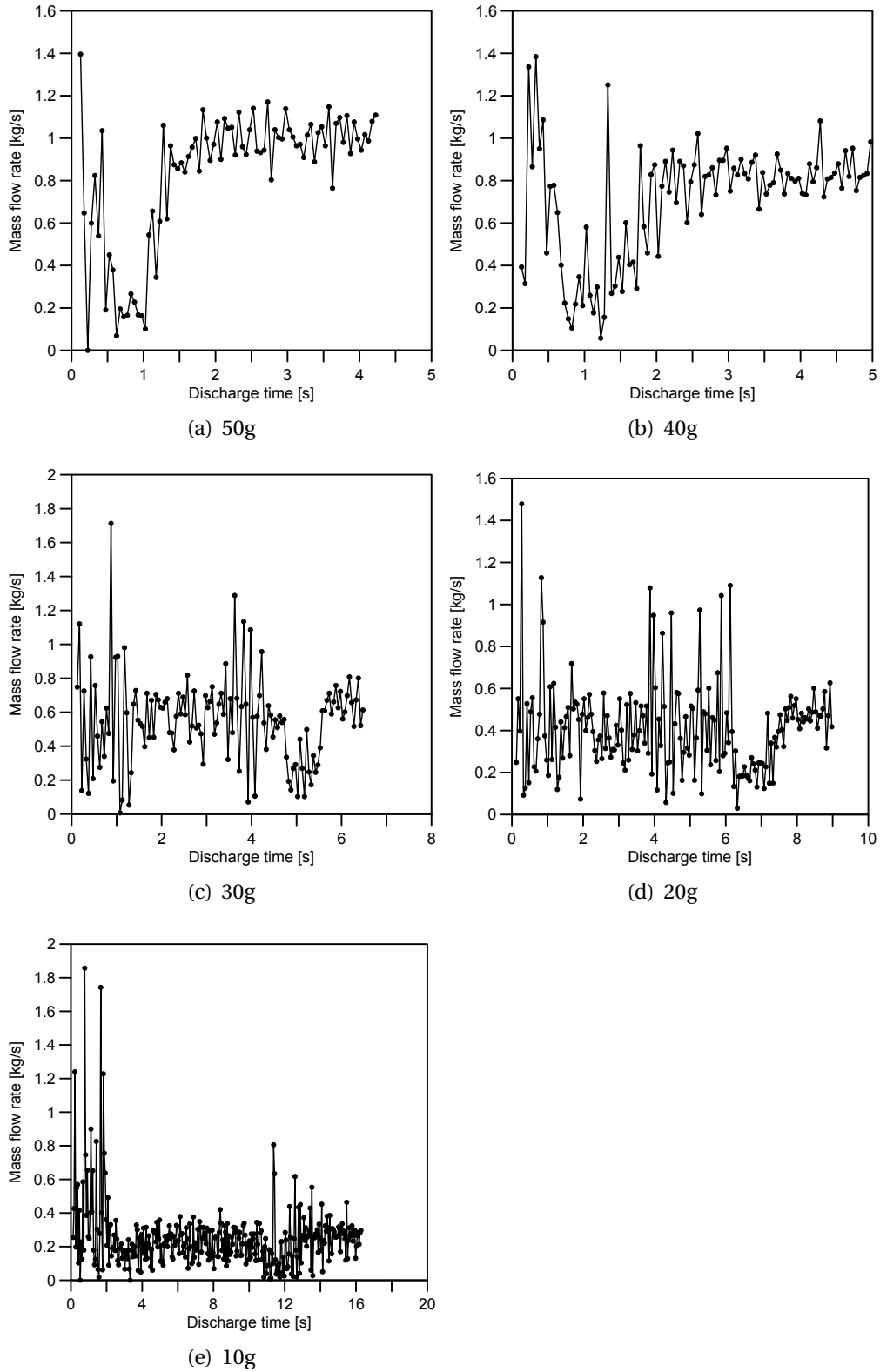


Figure 6.7: Discharge rate through time, silo with flat bottom

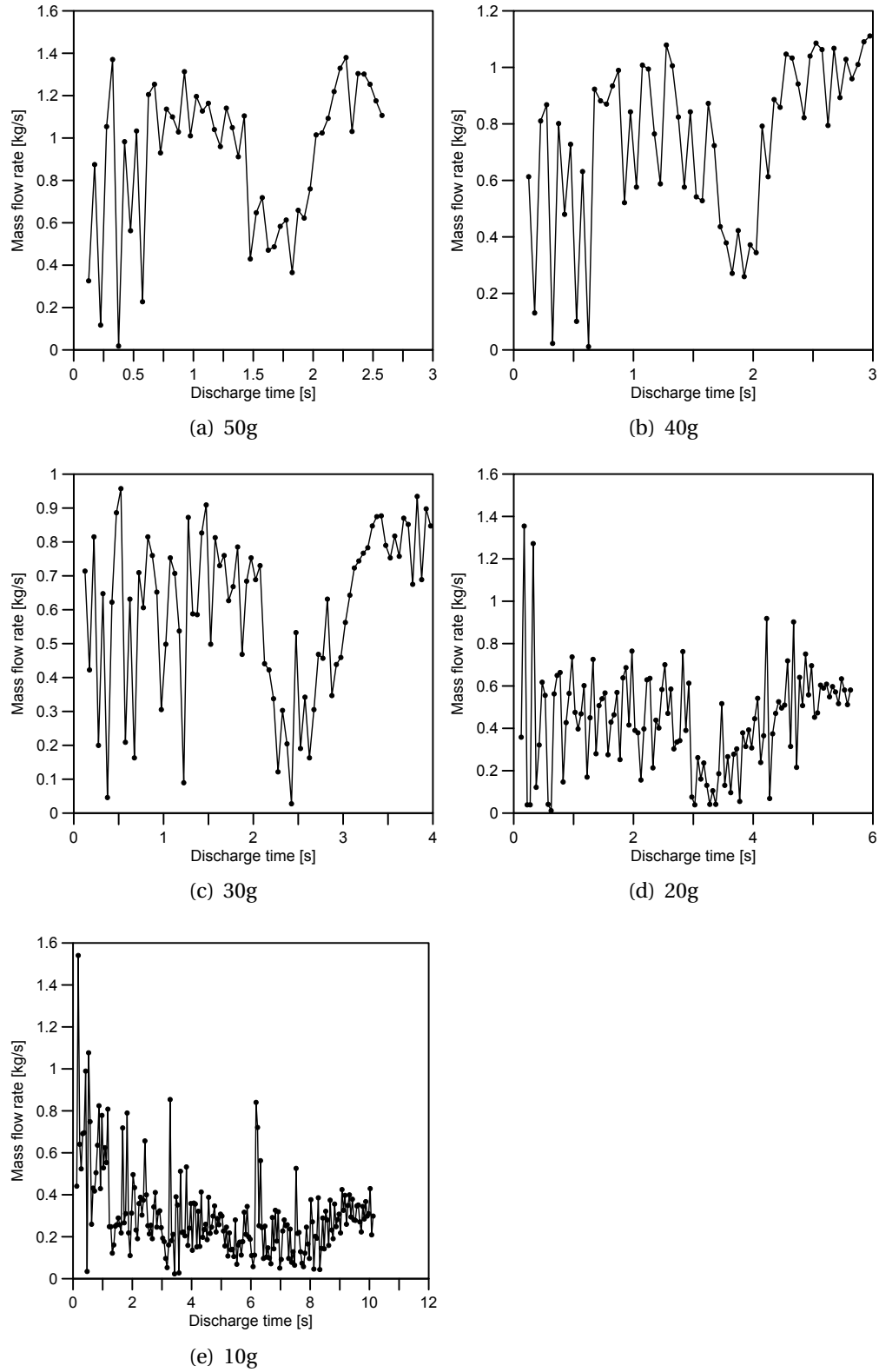


Figure 6.8: Discharge rate through time, silo with 30 degree hopper

## 6. DISCRETE ELEMENT MODEL OF SILO DISCHARGE

---

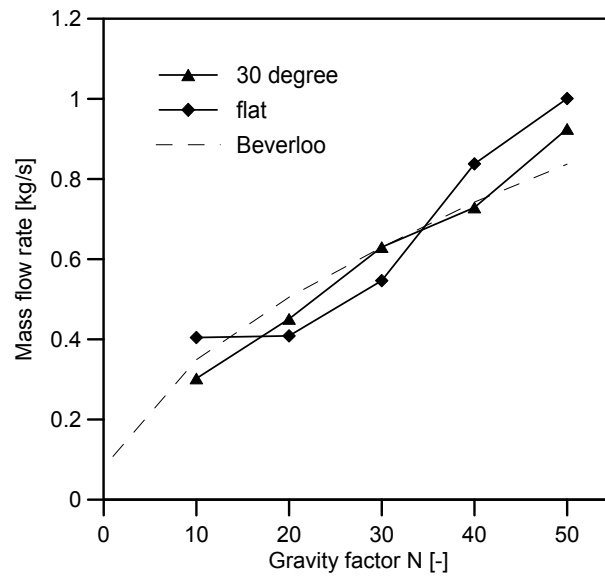


Figure 6.9: Observed discharge rates compared with Beverloo prediction

---

## Conclusion

The rates of discharge from the numerical model show larger fluctuations than were expected. The silo did not discharge at 1g as was expected and observed in the physical model (with the same  $d/W_0$  ratio). In the physical model, the discharge rate was lower at 1g than was predicted by the Beverloo equation suggesting that arching effects were present in the numerical model. The reason for the difference between the two models is thought to be the effect of particle shape, which is a large difference between the two models.

Another difference between observed and expected results from the numerical model is the relationship of discharge rate to gravity. The magnitudes of the discharge rate are close to those predicted using the Beverloo correlation. The amount of scatter is unexpected, since the initial conditions of all tests were the same, requiring that the causes of the scatter all originated after the gravity increased.

Finally, the effect of the silo geometry on the discharge rate is also not what was expected. A hopper should result in an increased flow rate compared to a silo with flat bottom. The Beverloo correlation in its standard form is applicable to a flat-bottomed silo, so that discharge rates from silos with hoppers would normally be greater than those predicted using the Beverloo correlation.

## 6.5 Flow patterns during discharge

### Background

The flow pattern in a silo is an important consideration in silo design and operation because not only is it closely related to discharge rate, it also greatly affects the forces exerted on the silo structure. It is therefore associated with two main types of silo failure, flow failure and structural failure, [Ooi et al. \[1998\]](#).

No reliable method yet exists to predict the angle at which the flowing material will intersect the wall boundary and therefore new information or observations about

internal flow patterns are needed.

### **Method**

The particle positions and velocities were output from PFC and processed in MATLAB. Delaunay triangulation was used to create an interpolation function in order to produce a continuous contour map from the discrete data points. The data points for the contour function were entered into a matrix with the same dimensions as the contour plot. A three-dimensional matrix was used for this with the size of the matrix in the third dimension being equal to the number of time steps in the analysis. The matrix was simply averaged in the third direction to produce a contour plot of average velocity magnitudes.

### **Results**

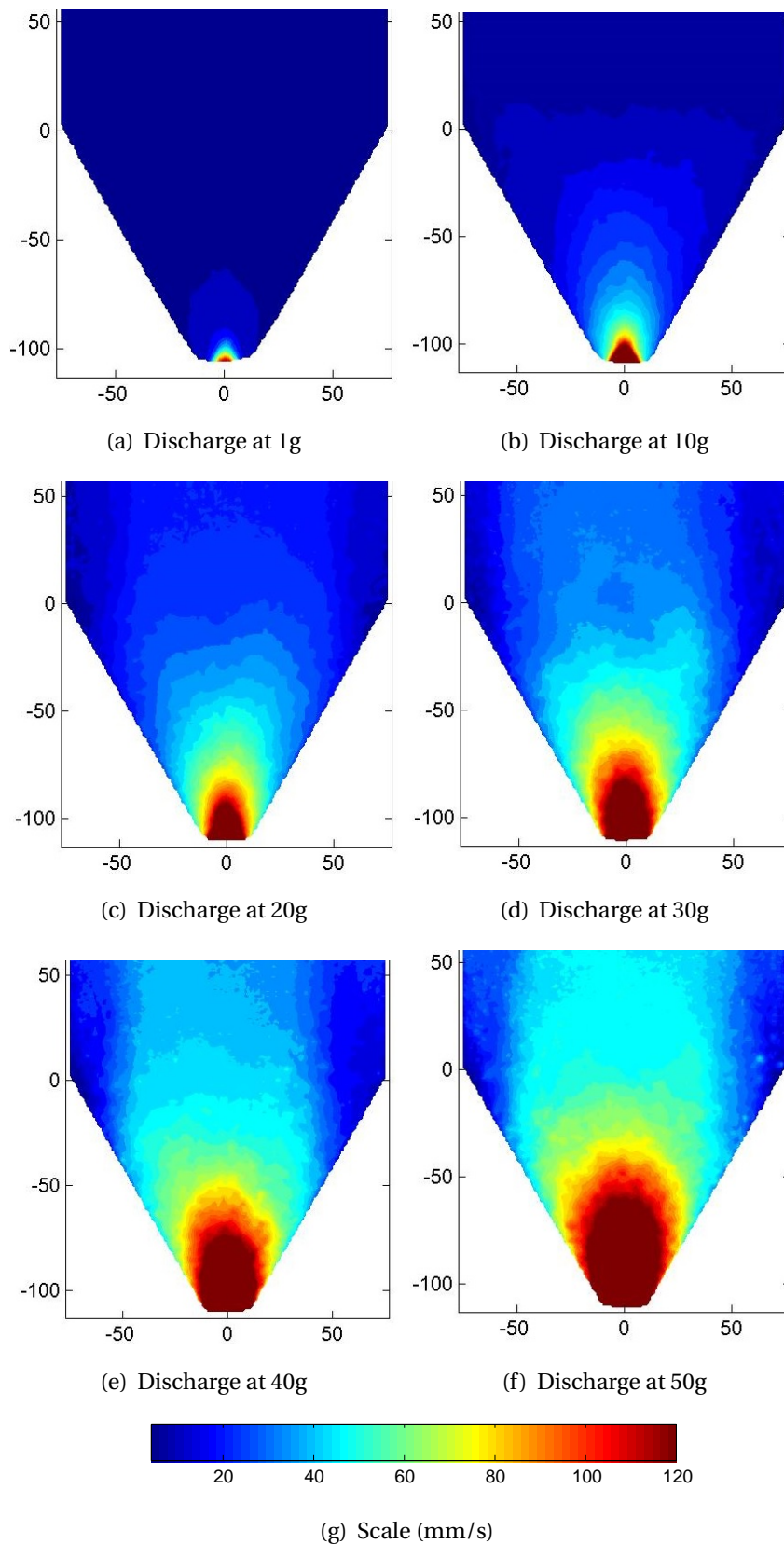


Figure 6.10: Flow pattern in model silo with 30 degree hopper

## 6. DISCRETE ELEMENT MODEL OF SILO DISCHARGE

---

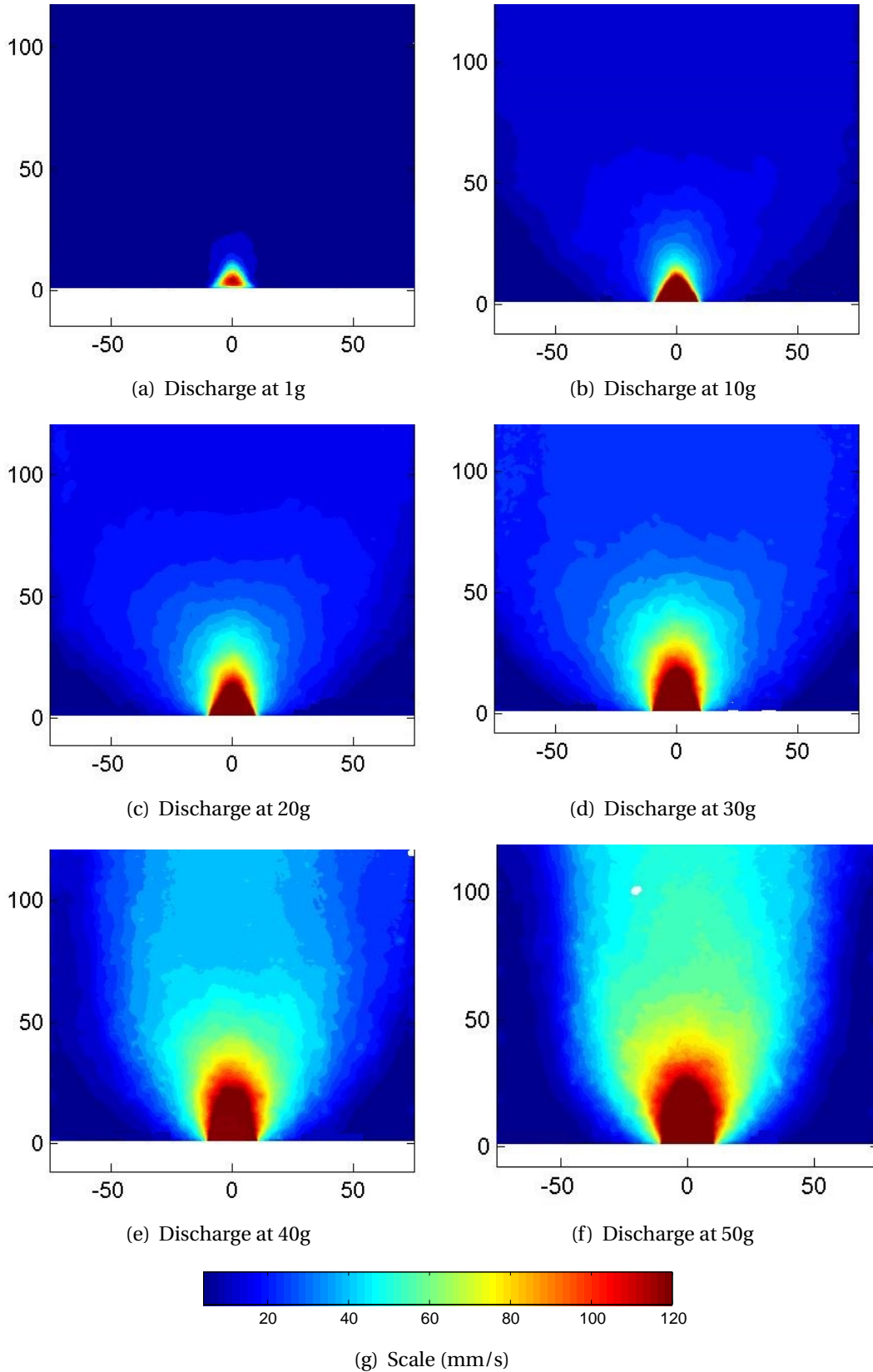


Figure 6.11: Flow pattern in model silo with flat bottom

---

## **Conclusions**

The averaged velocity magnitude contour plots show magnitudes that are smaller for the DEM model than in the physical silo centrifuge model. In the contour plots from the DEM model, the contour boundaries are often vertical at the left and right. This contrasts with the physical contour plots which shows contour boundaries propagating away from the centre as height above the outlet increases. This suggests that the stress field in the physical model is radial (with origin at the outlet or hopper apex) but in the numerical model is a function of height.

Despite the calibrated friction coefficients used in the numerical model, the interaction of the granular material against the hoppers is different in the numerical and physical models. In the numerical model, the velocity of the material is not dependent on its distance from the hopper wall, but in the physical model, the hopper wall appears to influence flow.

## 6. DISCRETE ELEMENT MODEL OF SILO DISCHARGE

---

# Chapter 7

## General conclusions and suggestions for further work

This thesis investigates the effects of gravity on a discharging silo centrifuge model. Four materials are investigated at gravities between 1g and 15g using high-speed video, Particle Image Velocimetry, load cells and a novel pressure-mapping system. Silo design methods and criteria, design standards and a literature review are presented in order to show the strengths and limitations of the current state-of-the-art.

Tests were conducted in a silo centrifuge model developed for use in the geotechnical centrifuge at the BOKU, Vienna. The granular response to gravity is investigated by measuring mass discharge rate, internal flow velocities and wall pressures before and during discharge. A Discrete Element Model of the silo centrifuge model was developed to validate the physical experimental results.

### Silo discharge rates at increased gravities

Silo discharge rate is shown to be proportional to the square root of the gravity. The mass discharge rate is quantified using two independent instrumentation types. Load cells beneath the collection bucket give one measure of discharge rate while calculations based on PIV analysis give another independent measure. The two methods are in agreement when the granular material has adequate texture. Materials

## 7. GENERAL CONCLUSIONS AND SUGGESTIONS FOR FURTHER WORK

---

with adequate texture for the PIV analysis are M1 and M2, while M4 has the poorest texture and material M3 gives mediocre quality results.

The observed discharge rate is compared to the discharge rate predicted using the Beverloo correlation. The Beverloo correlation in some cases gives a slightly better prediction of the discharge rate at 5g and higher, compared with the results at 1g when the normalised discharge rate is 5% lower than at higher gravities. Polyamide (M4) is the only material for which a large difference between the normalised discharge rates at 1g and other higher gravities is observed.

The Beverloo correlation was calculated using a  $k$  value of 1 throughout the analysis and this led to a consistent over-prediction at all gravities, although the magnitude varied between materials. For materials M1 and M2 (poorly graded sands) the Beverloo discharge rate was approximately 10% larger for the silo with flat bottom than was observed. For the silo with 30 degree hopper the modified Beverloo correlation predicted a rate that was 25% larger than observed.

The predicted discharge rates for material M3 (glass beads) were very close to those observed. For the flat-bottomed silo the error was on average 10% but for the silo with 30 degree hopper, the difference was less than 5%. M3 particles were spherical and smooth which may explain why there was a closer agreement between observed and predicted discharge rates.

Material M4 had the largest variation in the results and does not appear to have a discharge rate that is proportional to  $\sqrt{g^*}$ . For both the flat-bottomed silo and the silo with 30 degree hopper, the normalised discharge rate at 1g is  $\approx 25\%$  smaller than at other gravities. The average error between the rate predicted using the Beverloo correlation and the observed discharge rates is  $\approx 20\%$  for the silo with flat bottom and 40% for the silo with 30 degree hopper.

A value of  $k = 1.6$  gave the smallest error across all 4 materials.

### **Flow profiles during discharge at increased gravities**

Determination of the factors controlling funnel flow or mass flow conditions would benefit granular materials engineering. In this thesis it is shown that the location of

---

the flow intersection with the wall is independent of gravity and therefore the flow pattern is independent of gravity.

The velocity of the granular material during discharge was investigated in the following ways:

1. The vertical component of flow was quantified at 4 different gravities: The flow is recorded using high-speed video and analysed using PIV. When the vertical component of the flow is considered it is seen that normalising the velocity distribution according to  $u_{z,n} = u_z / \sqrt{g^*}$  produces flow profiles that take approximately the same shape and magnitude. This shows that  $u_z$  is proportional to  $\sqrt{g^*}$ .
2. The horizontal component of the flow was considered at the same gravities and the same normalisation method was applied  $u_{x,n} = u_x / \sqrt{g^*}$ :

Considering the horizontal component of the flow, the same relationship with gravity is seen where  $u_x$  is proportional to  $\sqrt{g^*}$ . Intriguing sign waves are produced with 0 amplitude at the walls and silo centre line and the same normalised amplitude.

3. The vertical component of the flow at 3 distances from the silo outlet were compared:

As the distance from the silo outlet increases the flow channel becomes wider and grain velocities decrease. The results in Section 5.10 suggest that in a region approximately 30mm-45mm from the vertical axis of symmetry, the velocity of the discharging material is a constant value and does not depend on its height above the silo outlet. Further analysis might show this to be an inflection point along the velocity profile at each height.

The only analytical method to calculate discharge rate from a hopper (and not a flat-bottomed silo) is Hour Glass Theory. This predicts discharge rates that are typically twice as large as observed and is therefore not suitable for application. It assumes a radial flow field and smooth silo walls which leads to assumed mass flow with no

internal shear gradient. In industry, the empirical work by [Rose and Tanaka \[1956\]](#) is recommended.

### **Silo centrifuge modelling**

Results from reduced-scale silo models in 1g environments are difficult to apply to silos of different scales also at 1g. This is due to the unknown nature of the stress dependency of the constituent relations of granular materials, and is a key limitation of the state-of-the-art and a priority for advancement. Centrifuge modelling is of interest because it can overcome the decrease in stress resulting from reductions in scale.

One of the fundamental differences between centrifuge modelling and other techniques is the different gravity magnitude experienced at different locations in the centrifuge model. The results in section 5.5 show that the variation of the apparent gravity did not have an observable effect on the discharge rate. This is explained by considering that many features of silo discharge including discharge rate are controlled by conditions near the outlet, and that the packing efficiency of material stored in silos does not affect its discharge rate. It is also clear that during discharge the acceleration of grains which are not close to the outlet is always less than the magnitude of gravitational acceleration.

The silo centrifuge model was designed as a quasi-two-dimensional planar silo and the results suggest that conditions very close to planar flow were achieved.

Key silo centrifuge model limitations are as follows:

1. The silo height is limited by the design of the centrifuge, in particular, the radius of rotation. Using a larger centrifuge would have allowed a taller silo to be modelled, allowing investigation of flow conditions and wall pressures across a greater range of depths. However because silos are generally tall and slender even a model in a very large centrifuge would have a small size compared to other silo models.
2. The silo opening mechanism caused more problems during tests than any other individual component. The frictional forces it would need to overcome

---

in order to open quickly were not properly appreciated and a more powerful opening mechanism should have been used. The limited force available to overcome friction caused by the increased self weight of the silo fill is the primary reason that the reported tests do not exceed 15g.

3. The high-speed camera gave remarkably good results for a consumer grade camera. However, both higher resolution and higher frame rates would have improved this research by allowing more accurate PIV analysis, and investigation of flow at greater discharge rates. Greater frame rates and resolutions incur increases in camera size and data-storage requirements which would be difficult to implement in the confined space available in the centrifuge swing basket.

Analysis of the time required to discharge the silo has led to the observation of a scaling law (Equation 5.1) for silo centrifuge models, which is useful for centrifuge models involving granular flows.

In a silo model discharging cohesionless material, time scales with gravity according to the following law:

$$t_m = t_p N^{-1/2}$$

### **Silo wall pressure measurements**

The tests using FSR arrays show that the sensor pads need to be improved before they can reliably be used in silo centrifuge models. Whilst in each test some of the results agree with wall pressures predicted according to theoretical design practices, a significant number of the FSR rows do not. The degree of agreement between pressure readings and predicted pressures varies between tests.

A large amount of variation between different pressure pad rows in each test is observed. The change in the readings recorded after changes in the applied forces often do not correspond with the magnitude of the change of applied forces. This may be influenced by shear stresses.

The FSR pressure pads do not give consistent enough readings for quantitative

## 7. GENERAL CONCLUSIONS AND SUGGESTIONS FOR FURTHER WORK

---

research. They correctly showed qualitative trends, but at a lower resolution than that of individual rows of FSR sensors.

### **The Discrete Element Model**

The results from the numerical model show that:

1. Despite giving good results for triaxial tests, the coefficient of friction used in the DEM model was unreasonably high. This caused significant dissimilarity between the physical and numerical models.
2. Spherical particles pack more efficiently than angular particles, resulting in higher bulk density and lower porosity.
3. Increasing the value of the coefficient of friction to counteract the effects of smooth spheres is not a complete solution. Although it does increase the angle of internal friction, it does not deal with the decreased porosity and increased bulk density which arise when using spherical particles.
4. The narrower particle size distribution used in the DEM model may mitigate, to an extent, the effects of the efficient packing of spheres. Spheres will pack more efficiently than angular particles, resulting in a granular mass that requires more energy to deform because it must dilate first, however the DEM model will also have a smaller fines fraction. The fines fraction of a granular material adds strength to a granular mass by increasing the interlocking of the particles. Ignoring the fines fraction will result in a granular mass that is easier to deform. The counteracting effects of spherical particles and a narrower particle size distribution have not been quantified.

### **Next steps**

Advances in digital photography and portable computing made the imaging analysis of the discharging silo centrifuge model possible as the methods used in this research would not have been possible five years ago. In the future, more detailed analysis will be possible using higher resolution video taken at a higher frame rate. Open-source

---

PIV codes are useful in many areas of research and it will be especially exciting for granular materials when patch rotations can be quantified as well as translations.

In a PIV analysis, the selection of an optimum patch size requires the optimisation of two conflicting interests. Large patches allow greater precision but smaller patches allow greater detail in areas of high strain gradient and prevents the strain gradient being “blurred out”. Guidelines for best practice in PIV analyses of granular materials should therefore be developed. In fluid mechanics this has been developed through the “PIV challenge” initiative but due to the experimental differences between fluid mechanics and other fields, many recommendations are not directly transferable. Therefore a granular materials centric method to quantify image texture and optimise PIV calibration and validation parameters for granular flows would be useful.

Modern instrumentation makes silo centrifuge modelling viable to a greater extent than in previous decades. This thesis shows that discharge rate is proportional to gravity as the Beverloo correlation predicts, that Janssen wall pressures probably scale as continuum theory predicts and has presented a scaling law for time in a centrifuge model. It is therefore reasonable to believe that further valuable insight may be gained from additional silo centrifuge model investigations.

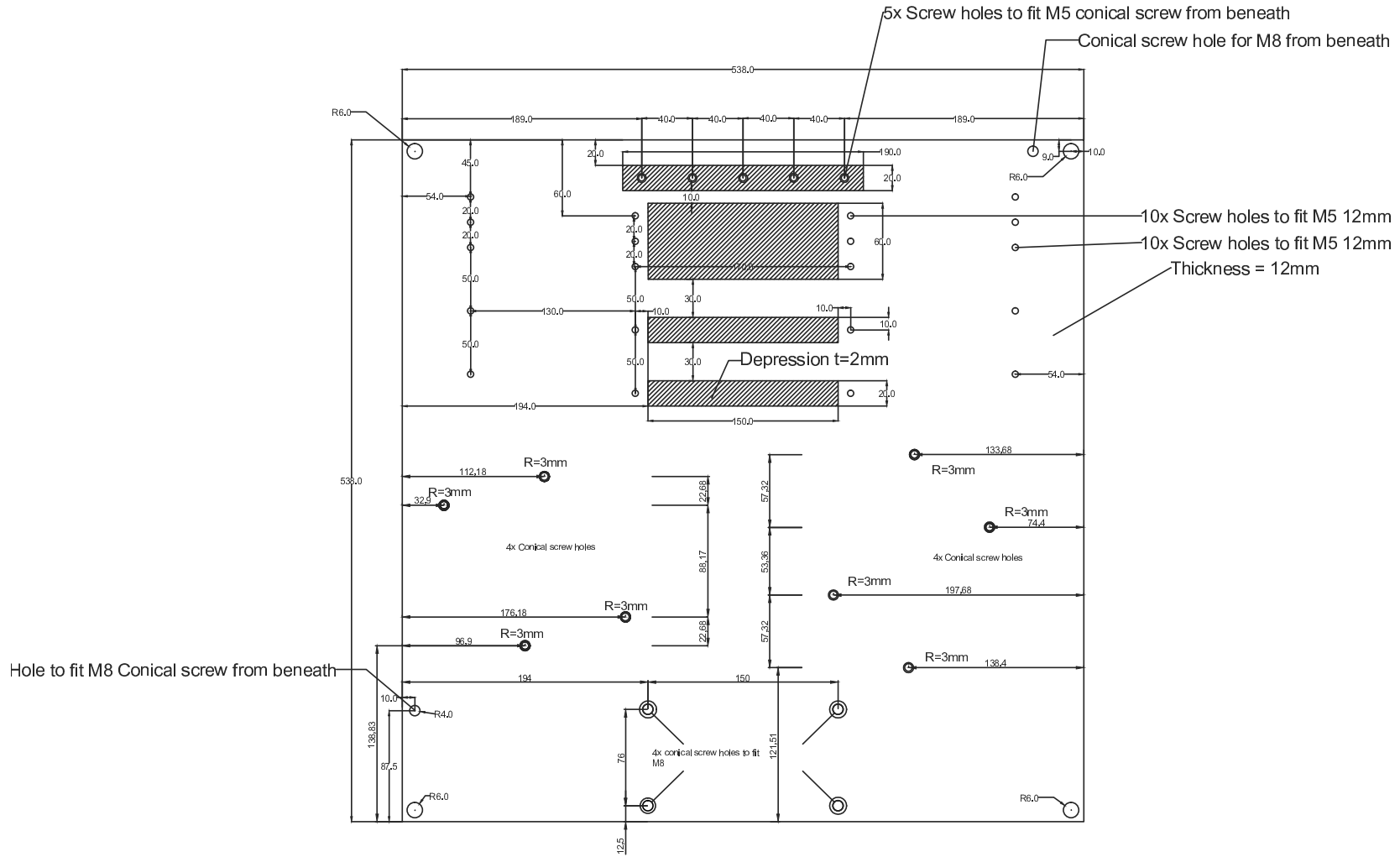
More powerful high-speed cameras would allow more detailed and more accurate quantification and description of flow-fields during discharge, and the small amounts of material required would allow relatively cheap but detailed investigations into the effects of particle size and shape on the flow field. 3D-printing is becoming increasingly affordable and could provide unparalleled control of bulk granular material properties.

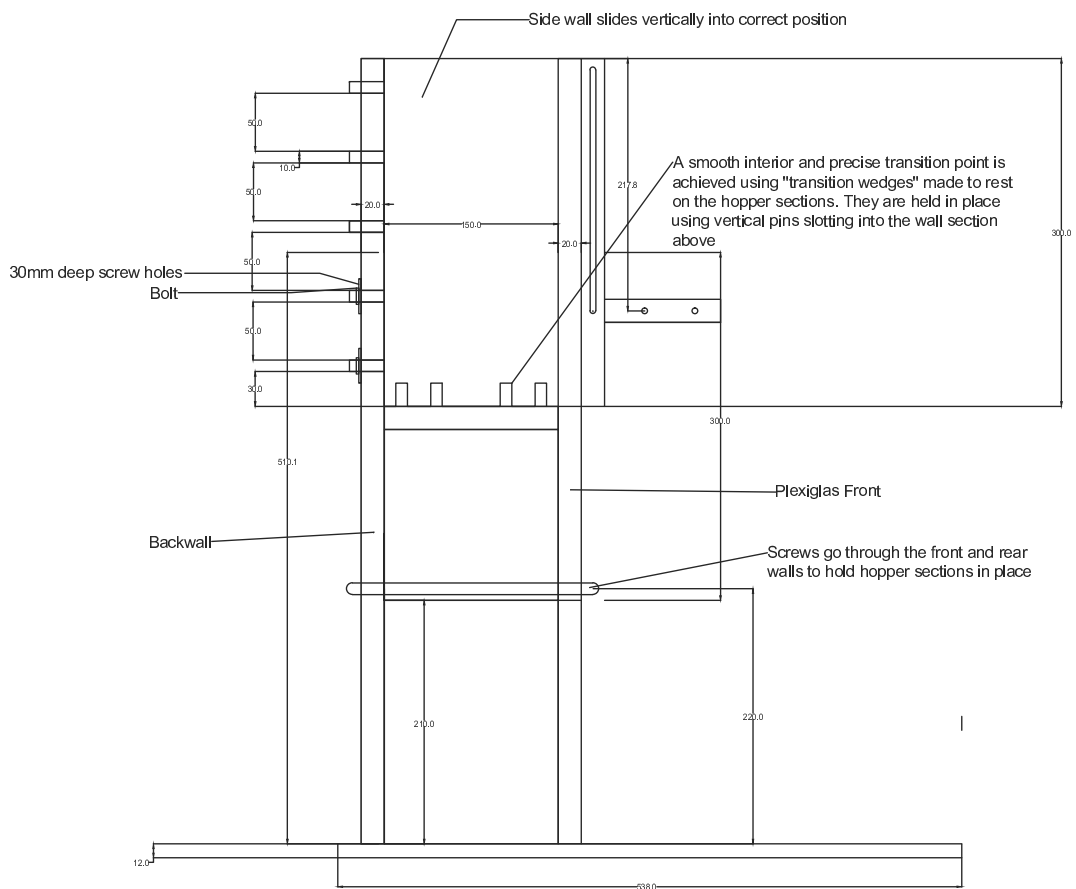
It would be simple to modify the silo centrifuge model used in this research to investigate silo discharge with silo inserts and/or eccentric discharge. A priority for granular materials engineering in variable gravities is confirmation of the effect of gravity on angle of repose. At present, different researchers have reported conflicting results and this thesis was not able to investigate the effect in detail and go beyond a qualitative observation.

## 7. GENERAL CONCLUSIONS AND SUGGESTIONS FOR FURTHER WORK

# **Appendix A: Silo centrifuge model drawings**

# Base plate



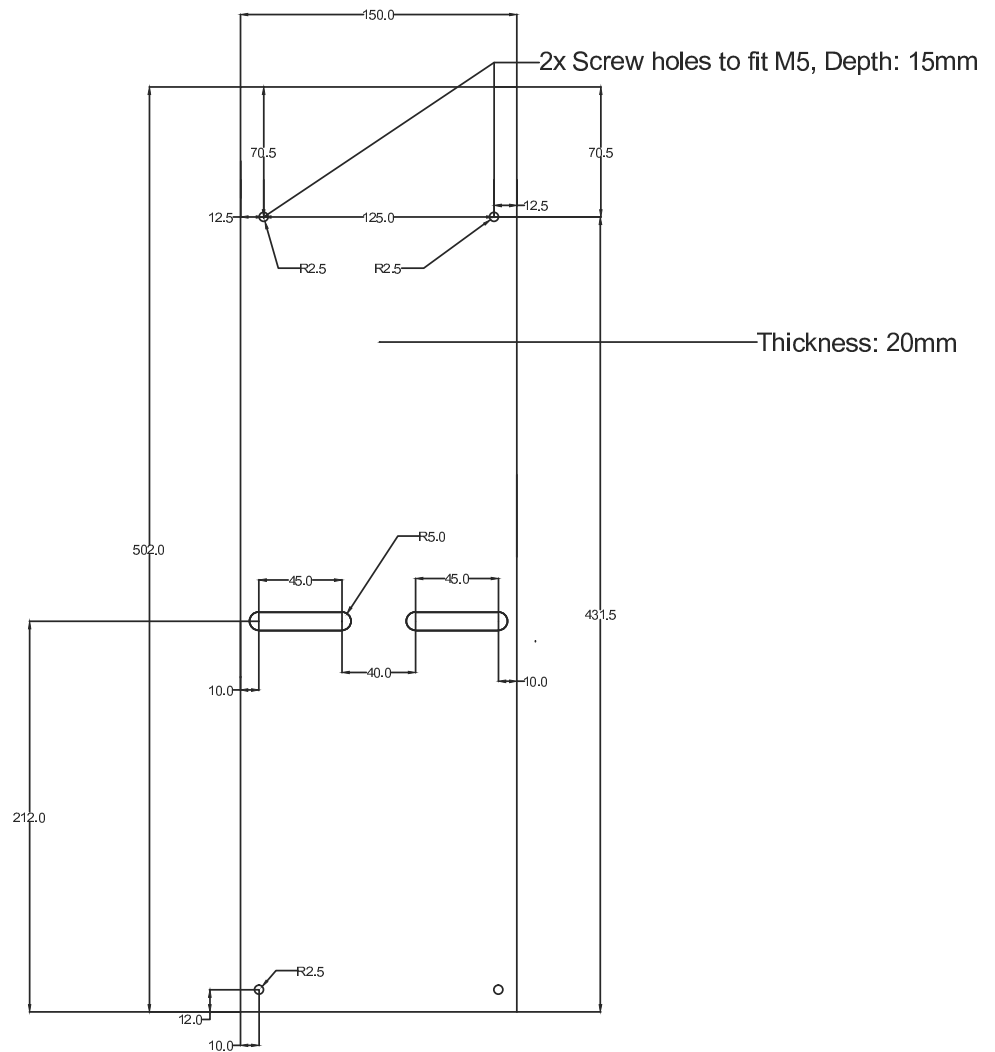


Side profile 30° Hopper half angle

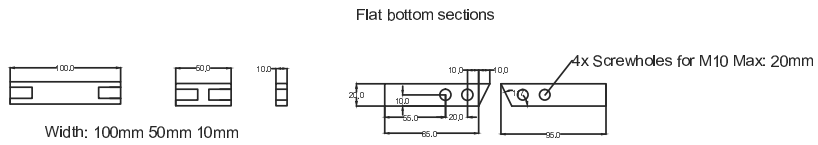
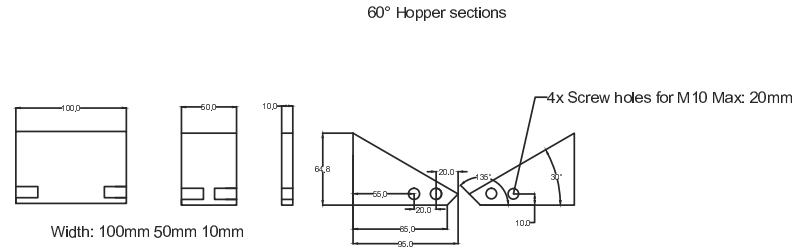
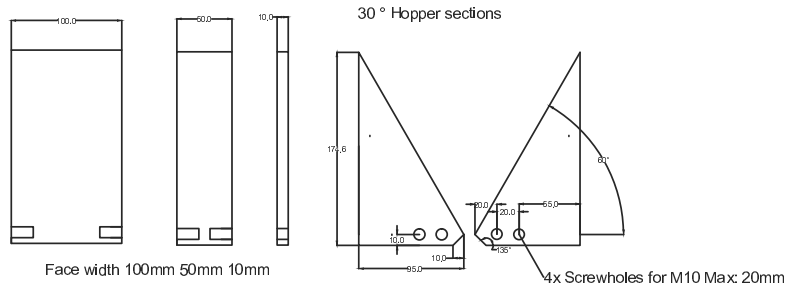
## 7. APPENDIX A: SILO CENTRIFUGE MODEL DRAWINGS

---

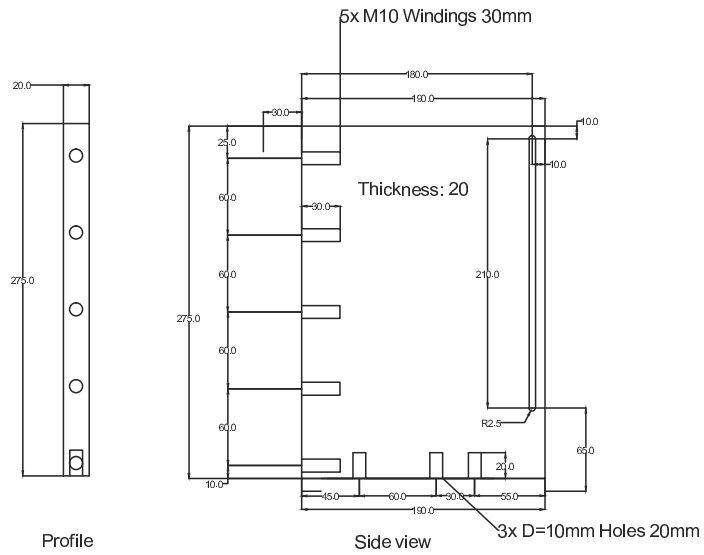
### Acrylic front



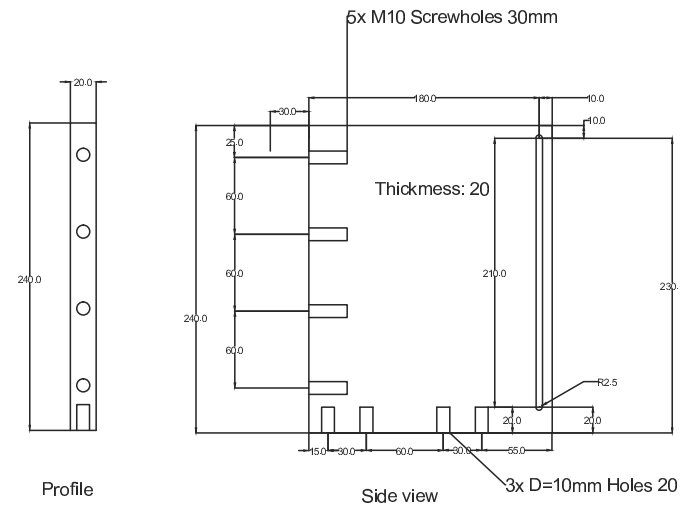
### 3 Pairs of silo hopper sections in 3 thicknesses: 10mm, 50mm, 100mm



### 2 x Side walls Height: 75mm

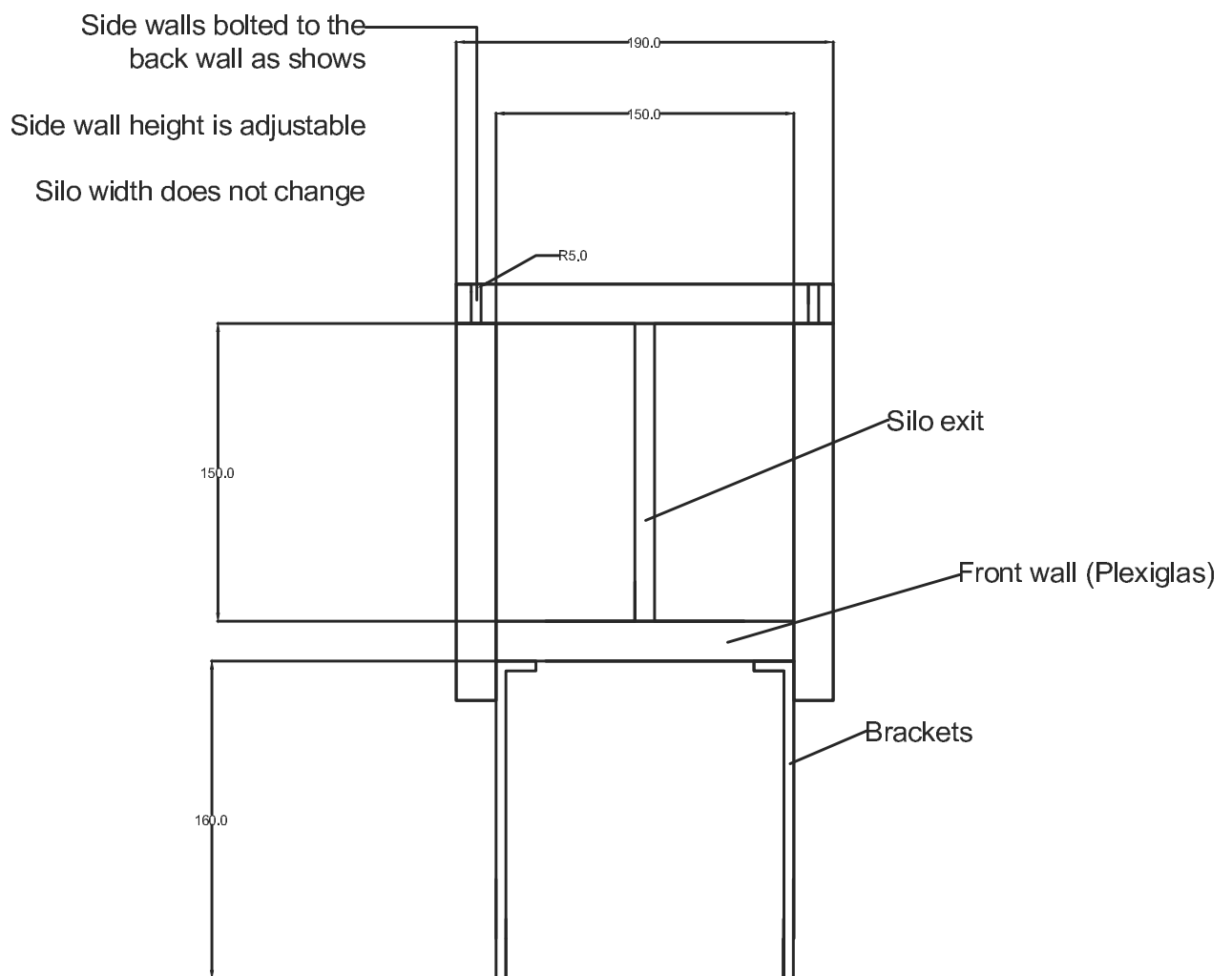


### 2 x Side walls Height: 240mm



---

## Top view: 150mm internal width



## 7. APPENDIX A: SILO CENTRIFUGE MODEL DRAWINGS

---

## **Appendix B: Instrumentation details - Load Cells**

# C9B

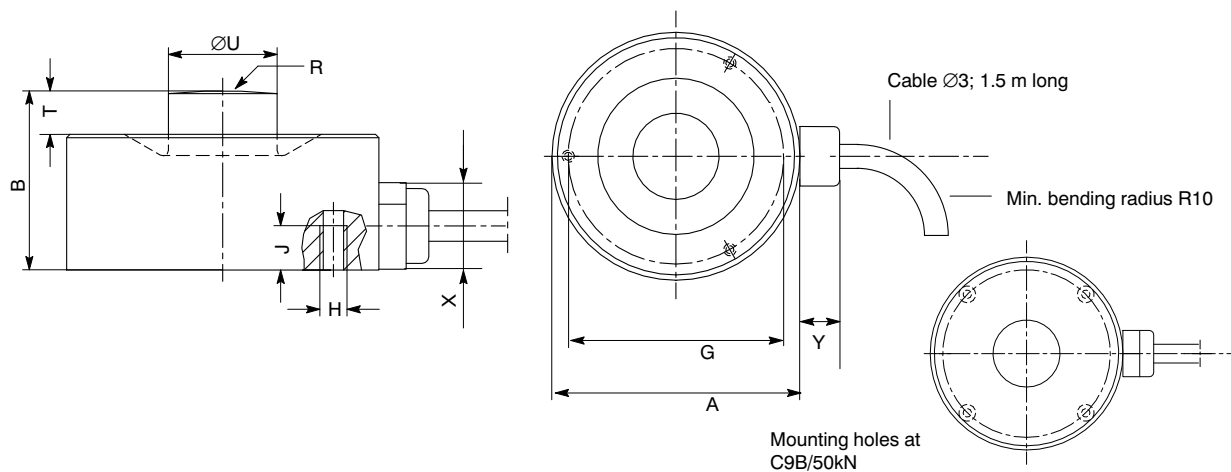
## Force Transducers



### Special features

- Compression force transducers in non-rusting material
- Rated (nominal) forces 50 N ... 50 kN
- Small size
- Accuracy class 0.5

Dimensions (in mm; 1 mm = 0.03937 inches)



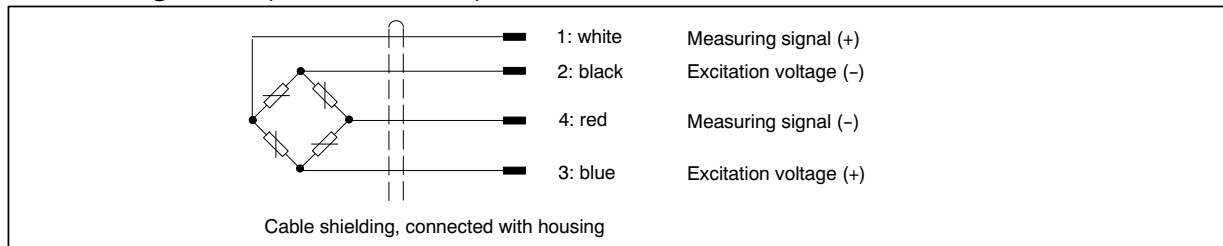
Rated (nominal) force C9B	A <sub>-0.1</sub>	B	G <sub>±0.1</sub>	H	J	R	T	U <sub>-0.1</sub>	X	Y
50 N ... 200 N	26	15	20.5	3xM3	6	20	2.5	5.5	approx. 10.5	approx. 5.5
0.5 kN ... 20 kN	26	13	22.75	3xM2	3.5	40	1	8	approx. 10.5	approx. 5.5
50 kN	46	28	40	4xM4	6	80	8	16	approx. 10.5	approx. 5.5

## Specifications (VDI/VDE 2638 standards)

Type	C9B											
Nominal (rated) force	$F_{nom}$	N	50	100	200							
		kN				0.5	1	2	5	10	20	50
Nominal (rated) sensitivity	$C_{nom}$	mV/V	1									
Accuracy class			0.5									
Relative sensitivity error	$d_C$	%	$\leq 1$									
Relative reproducibility error with unchanging mounting position	$b_{rg}$	%	$\leq \pm 0.5$									
Zero signal error	$(d_s, 0)$	mV/V	$\pm 0.075$			$\pm 0.2$						
Relative reversibility error (at 0.5 $F_{nom}$ )	$v_{0.5}$	%	$\leq \pm 0.5$									
Relative linearity error	$d_{lin}$	%	$\leq \pm 0.5$									
Relative creep over 30 min	$d_{crF+E}$	%	$\leq \pm 0.2$									
Effect of temperature on the sensitivity per 10 K in the nominal (rated) temperature range in the operating temperature range	$TK_C$	%	$\leq \pm 0.5$ $\leq \pm 0.8$									
Effect of temperature on the zero signal per 10 K in the nominal (rated) temperature range in the operating temperature range	$TK_0$	%	$\leq \pm 0.5$ $\leq \pm 0.8$									
Output resistance	$R_a$	$\Omega$	300 ... 400			< 350						
Input resistance	$R_e$	$\Omega$	> 345			300 ... 400						
Insulation resistance	$R_{is}$	G $\Omega$	> $10^9$									
Reference excitation voltage	$U_{ref}$	V	5									
Operating range of excitation voltage	$B_{U,G}$	V	0.5 ... 12									
Reference temperature	$T_{ref}$	$^{\circ}C$ [ $^{\circ}F$ ]	+23 [+73]									
Nominal (rated) temperature range	$B_{T,nom}$	$^{\circ}C$ [ $^{\circ}F$ ]	-10 ... +70 [+14 ... +158]									
Operating temperature range	$B_{T,G}$	$^{\circ}C$ [ $^{\circ}F$ ]	-30 ... +85 [-22 ... +185]									
Storage temperature range	$B_{T,S}$	$^{\circ}C$ [ $^{\circ}F$ ]	-30 ... +85 [-22 ... +185]									
Maximum operating force	$(F_G)$		200			120						
Breaking force	$(F_B)$	% of $F_{nom}$	> 400									
Static lateral force limit <sup>1)</sup>	$(F_Q)$		100			40						
Nominal (rated) displacement $\pm 15$ %	$s_{nom}$	mm	< 0.1			0.04	0.06	0.09	0.11	0.13		
Fundamental resonance frequency $\pm 15$ %	$f_G$	kHz	7.3	10	15.7	3.5	5	7	13	15.1	20	12
Permissible oscillatory stress (vibration bandwidth per DIN 50100)	$F_{rb}$	% of $F_{nom}$	70									40
Weight, approx.		g	55			65						260
Degree of protection per DIN EN 60529			IP67									
Cable length		m	1.5									

<sup>1)</sup> referred to a force application point 2 mm above membrane

### Cable assignment (Four wire circuit)



Modifications reserved.  
All details describe our products in general form only. They are not to be understood as express warranty and do not constitute any liability whatsoever.

#### Hottinger Baldwin Messtechnik GmbH

Im Tiefen See 45 · 64293 Darmstadt · Germany  
Tel. +49 6151 803-0 · Fax: +49 6151 803-9100  
Email: [info@hbm.com](mailto:info@hbm.com) · [www.hbm.com](http://www.hbm.com)

measure and predict with confidence



## 7. APPENDIX B: INSTRUMENTATION DETAILS - LOAD CELLS

---

# **Appendix C: Recommendations for silo centrifuge model design and development**

During the implementation of the model many challenges were overcome. Some of the key lessons learned whilst constructing and developing the model are described below in order to assist future work with silo centrifuge models and allow researchers to develop models more quickly and efficiently.

Challenges encountered when designing a silo centrifuge model tend to stem from one of two main sources. Firstly, silos tend to be tall and thin whilst centrifuges encourage short and wide models. This makes geometric constraints an important consideration. Secondly, the space, bandwidth and energy available for instrumentation and equipment are all reduced because of the size of the centrifuge and the configuration of the slip rings. Therefore careful consideration should be given to each component of the experiment.

## **Cameras**

High gravity environments place unusual demands on mechanical components and the reaction of consumer-grade products to these environments varies widely. The focusing elements of a lens are the parts of a camera likely to fail first. This will result in focus being lost above a certain centrifugal acceleration, though once

## 7. APPENDIX C: RECOMMENDATIONS FOR SILO CENTRIFUGE MODEL DESIGN AND DEVELOPMENT

---

the test is complete, no camera has ever remained dysfunctional for long. Larger lenses generally work better than smaller, lighter lenses. If low resolution (HD720 or lower) and frame rate is allowable, then a fixed focus camera becomes a good option because it has no moving parts.

If high resolution photographs are required then it is recommended to avoid using an SLR in favour of a camera without a reflex mechanism. Two cameras that have been found to work well in the centrifuge are the Canon g12 point-and-shoot for photographs, and the Casio Exilim EX-ZR15 for low-resolution high-speed video. (512px x 384px, 232 fps). Both of these cameras offer good quality for their cost.

### **Computers**

A laptop (a 15-inch HP Pavillion g6 1255sg was used in the research) would work well in the centrifuge save for two problems:

1. Rapid over-heating results from reduced air pressure near the centrifuge axis which reduces the efficiency of the cooling fan. This is avoided by providing a larger ventilation hole to the fan.
2. Data cannot be read from or written to a mechanical hard disk at high g-levels. Attempting to read or write data at gravities greater than 10g results in immediate system shut down because the hard disk head cannot move correctly. This problem is removed by installing a solid-state hard drive.

### **Air pressure**

The centrifuge at BOKU-IGE is a caged cantilevered centrifuge. The cage is included as a safety feature and has the effect of limiting the movement of air away from the centrifuge. Consequently when the centrifuge is accelerated the air inside the cage accelerates as well and rotates about the centrifuge axis. This has had two observed consequences.

- 
1. The power required to accelerate the centrifuge to a particular speed is larger than if the centrifuge was not in a cage, because the air in the cage must also be accelerated. Once the centrifuge has reached the required speed it will continue to accelerate a little as the air in the cage is still receiving momentum from the arm. This results in the centrifuge speed being somewhat higher than the speed dialled into the control panel and the operator must adjust the speed manually.
  2. Air pressure in the centrifuge increases with radial distance from the axis. This has a large effect on the efficiency of cooling fans in computers or other equipment. If the equipment is near the centre of the centrifuge then the air pressure will be reduced and the equipment will be vulnerable to over heating. This was observed when using the centrifuge laptop to operate the lateral wall pressure pads and process video data from the security camera. It is the processor that will over-heat first so by considering how much processing power a task will require, the need for additional cooling may be assessed.

## **Slip-rings**

The quality of slip-rings has a large effect on the bandwidth which can be used to transmit data. This was evidenced by the limitations imposed on high bandwidth activities such as video surveillance of the model during flight. A low resolution web camera, streaming video data at 480p at 30fps was only able to output a maximum of about 1 fps to the control room.

Because the video quality is low it is noted that a quicker safety measure is attentively listening to the centrifuge. With experience, the researcher learns how the motor and beam should sound at certain accelerations, and in the event that something goes wrong it would inevitably make a sound that could be responded to much quicker than if the researcher was only looking at the security camera. The scope for wireless data transfer should be assessed.

### **Coriolis forces**

When designing silo centrifuge models, the researcher should foresee the effects of Coriolis forces and how to minimise them.

### **Dust**

If equipment needs to be screwed or unscrewed between tests then the effects of dust should be considered. If there is a low tolerance then build up of fines can either slow down or stop the resetting of the model altogether.

# References

- Abbaspour-Fard, M. Emadi, B. K. M. (2010). Role of model particle shape in discrete element models of bed structure in containers. *Journal of Food Process Engineering*, 33:117–130. [43](#), [52](#)
- Arnold, P.C. McLean, A. R. A. (1980). *Bulk Solids: Storage, Flow and Handling*. University of Newcastle, NSW, Australia. [43](#)
- Beverloo, W. A., Leniger, H. A., and van de Velde, J. (1961). The flow of granular solids through orifices. *Chemical Engineering Sciences*, pages 260 – 269. [12](#), [26](#), [27](#), [32](#)
- Brown, R. and Richards, J. (1960). Profile of flow of granules through apertures. *Transactions of the institute of chemical engineers*, 38. [30](#), [31](#)
- Brown, R. L. and Richards, J. C. (1970). *Principles of Powder Mechanics*. Oxford: Pergamon Press. [31](#)
- Brucks, A., Arndt, T., Ottino, J., and Lueptow, R. M. (2007). Behaviour of flowing granular materials under variable g. *Phys. Rev.*, 75. [35](#)
- Carson, J. (2001). Silo failures: case histories and lessons learned. 10:153 – 166. [44](#), [52](#)
- Carson, J. A. and Jenkyn, R. T. (1993). *Load development and structural considerations in silo design*. [52](#)
- Cheng, Y. M., Chau, K. T., Xiao, L. J., and Li, N. (2010). Flow pattern for a silo with two layers of materials with single or double opening. *Journal of Geotechnical and Geoenvironmental Engineering*, 136:1278 – 1286. [51](#)

## REFERENCES

---

- Cleary, P. (2002). Dem modelling of industrial granular flows: 3d case studies and the effect of particle shape on hopper discharge. *Applied Mathematical modelling*, 26:899 – 111. [44](#), [52](#)
- Craig, W. (1989). Edouard phillips (1821 - 1889) and the idea of centrifuge modelling. *Geotechnique*, 39:697 – 700. [38](#)
- Craig, W. and Wright, A. (1981). Centrifuge modelling in flow prediction - studies for granular materials. *Institution of Chemical engineers symposium*. [39](#), [53](#)
- Cundall, P. A. and Strack, O. D. L. (1979). A discrete numerical model for granular assemblies. *Géotechnique*, 29:47 – 65. [45](#)
- Dorbolo, S., Maquet, L., Brandenbourger, M., Ludewig, F., Lumay, G., Caps, H., Vandewalle, N., Rondia, S., Melard, M., van Loon, J., Dowson, A., and Vincent-Bonnieu, S. (2013). Influence of the gravity on the discharge of a silo. *Granular Matter*. [73](#)
- Egerer, B. (1982). Kritische auslaufdurchmesser bei massenflussbunkern fuer kohäsive schuettgueter. [39](#), [53](#)
- Electronics, I. (1993). Force and position sensing resistors: An emerging technology. Technical report, Electrade GmbH. [140](#)
- Ewalt, D. J. and Buelow, F. H. (1963). The flow of granular solids through orifices. *Quarterly bulletin of the Michigan Agricultural Experiment Station*, 46(1):92–102. [26](#), [27](#)
- Fedler, C. B. (1988). Mathematical models describing the flow of granular materials. *Mathematical computational modelling*, 11:510–513. [26](#), [27](#)
- Ferstl (1998). *Modellversuche zum Erddruck*. PhD thesis, Universitaet fuer Bodenkultur, Vienna. [xvii](#), [70](#)
- Fowler, R. T. and Glastonbury, J. R. (1959). The flow of granular solids through orifices. *Chemical Engineering Science*, 10:150–156. [26](#), [34](#)

- Gregory, J. M. and Fedler, C. B. (1987). Equation describing granular flow through circular orifices. *Transactions of the ASAE*, 30(2):529–532. [26](#), [27](#)
- Grossstueck, M. and Schwedes, J. (2005). Application of model tests on cohesive bulk solids using silo centrifuge technique. *Powder Technology*, 157:149 – 155. [40](#), [53](#)
- Idinger, G. (2010). *Centrifuge model tests and numerical analysis on the face stability of shallow tunnels in dry sand*. PhD thesis, Universitaet fuer Bodenkultur, Institut fuer Geotechnik, Vienna. [69](#), [72](#)
- Jaky, J. (1948). Pressures in silos. In *Proceedings of the 2nd International Conference on Soil Mechanics and Foundation Engineering*, volume 1, pages 103 – 107. Rotterdam. [24](#)
- Janssen, H. (1895). Versuche ueber getreidedruck in silozellen. *Zeitschr. d. Vereines deutscher Ingenieure*, pages 1045 – 1049. [15](#), [16](#), [42](#)
- Jenike, A. W. (1964). *Storage and flow of solids*. University of Utah, Salt Lake City. [8](#), [22](#), [42](#)
- Jenike, A. W., Johanson, J. R., and Carson, J. W. (1973). Bin loads - parts 2, 3 and 4: Concepts, mass flow bins, funnel flow bins. *J. Eng. Ind., Trans. ASME*, 95 (1, Series B):1–5, 6–12, 13–16. [43](#)
- Job, N., Dardenne, A., and Pirard, J. (2009). Silo flow-pattern diagnosis using the tracer method. *Journal of food engineering*, 91:118 – 125. [51](#)
- Ketchum, M. (1907). *Design of Walls, Bins and Grain Elevators*. McGraw-Hill, New York. [26](#)
- Klein, A. (1998). Untersuchung zur lockesten und dichtesten lagerung von boeden. Master's thesis, Institute for Geotechnical Engineering, University of Natural Resources and Life Sciences, Vienna. [90](#)
- Kleinhans, M. G., Markies, H., de Vet, S. J., in't Veld, A. C., and Postema, F. N. (2011). Static and dynamic angles of repose in loose granular materials under reduced gravity. *Journal of Geophysical Research: Planets*, 116:E11004, doi:10.1029/2011JE003865. [73](#)

## REFERENCES

---

- Kleinhaus, M. . G., Markies, H., s. J. de In't Vet, and Pstema, F. N. (2011). Static and dynamic angles of repose in loose granular materials under reduced gravity. *J. Geophys. Rees.*, 116. [35](#)
- Knowlton, T. M., Carson, J. W., Klinzing, G. E., and Yang (1994). The importance of storage, transfer and collection. 90:44 – 54. [1](#)
- Kristiansen, N., Munch-Andersen, J., and Nielsen, J. (1988). *A centrifuge study of load and flow conditions in silos with cohesive media*, pages 593 – 600. [40](#), [53](#)
- Lepert, P., Ranaivoson, D., and Gourdon, J. (1989). Centrifuge modelling of the flow of a granular medium. *Powders and Grains*, pages 477 – 484. [40](#), [53](#)
- Molerus, O. and Schoeneborn, P. (1977). Bunker design based on experiments in a bunker-centrifuge. *Powder Technology*, 16:265 – 272. [39](#), [53](#)
- Muir Wood, D. (1990). *Soil Behaviour and Critical State Soil Mechanics*. Cambridge University Press, Cambridge, England. [24](#)
- Myers, M. E. and Sellers, M. (1977). Final-year project report. Master's thesis, Department of Chemical Engineering, Cambridge. [35](#)
- Nedderman, R. M. (1992). *Statics and Kinematics of Granular Flow*. Cambridge University Press, Cambridge, England. [26](#), [30](#)
- Nedderman, R. M. and Laohakul, C. (1980). The thickness of shear zone of flowing granular materials. *Powder Technology*, 25:91 – 100. [31](#)
- Nielsen, J. (1984). *Centrifuge testing as a tool in silo research - Application of centrifuge modelling to geotechnical design*, pages 475 – 483. Rotterdam. [40](#), [41](#), [42](#), [53](#)
- Nielsen, J. (1998). Pressures from flowing granular solids in silos. *Mathematical, Physical and Engineering Sciences*, 356:2667–2684. [52](#)
- Nielsen, J. and Askegaard, V. (1977). Scale errors in model tests on granular media with special reference to silo models. *Powder Technology*, 16:123 – 130. [39](#), [53](#)
- Ooi, J., Chen, J. F., and Rotter, J. M. (1998). Measurement of solids flow patterns in a gypsum silo. *Powder Technology*, 99. [171](#)

- Ramirez, A., Nielsen, J., and Ayuga, F. (2010). Pressure measurements in steel silos with eccentric hoppers. *Powder Technology*, 201:7 – 20. [52](#)
- Rose, H. F. and Tanaka, T. (1956). *The Engineer (London)*, page 208. [32](#), [33](#), [180](#)
- Rotter, M. (1999). Flow and pressures in silo structural integrity assessments. In *Proceedings of the International Symposium: Reliable Flow of Particulate Solids III*, Porsgrunn, Norway. [43](#)
- Rotter, M. (2005). Silo design loads from stored bulk solids: the provisions of the new eurocode en 1991-4 (2005). In *Proceedings of the IMechE Seminar on Specifying and Designing Safe Storage Silos*, IMechE. [8](#)
- Rotter, M. (2009). Silos and tanks in research and practice: State of the art and current challenges. [41](#), [42](#)
- Schofield, A. N. (1980). Cambridge geotechnical centrifuge operations. *Geotechnique*, 30(3):227–268. [36](#)
- Sielamowicz, I. and Czech, M. (2010). Analysis of the radial flow assumption in a converging model silo. *Biosystems engineering*, 106:412 – 422. [51](#)
- Tejchman, J. (2013). *Confined granular flow in silos*. Springer. [82](#)
- Walker, D. M. (1966). An approximate theory for pressure and arching in hoppers. *Chem. Eng. Sci.*, 21:975 – 997. [19](#), [42](#), [43](#)
- Walters, J. K. (1973). A theoretical analysis of stresses in silos with vertical walls. *Chem. Eng. Sci.*, 28:13–21. [43](#)
- Wu, J., Binbo, J., Chenb, J., and Yang, J. (2009). Multi-scale study of particle flow in silos. *Advanced powder technology*, 20:62 – 73. [51](#)
- Zhang, J. Y. and Rudolph, V. (1991). Effect of shear friction on solid flow through an orifice. *Industrial Engineering Chemistry*, 30:1977 – 1981. [31](#)
- Zhong, Z., Ooi, J., and Rotter, J. M. (2001). The sensitivity of silo flow and wall stresses to filling method. *Engineering Structures*, 23:756–767. [51](#)